CROSS SECTION MEASUREMENT OF LIGHT IONS USING (p,xp) AND (p,xn) REACTIONS

by

Doris Carole Kenfack Jiotsa

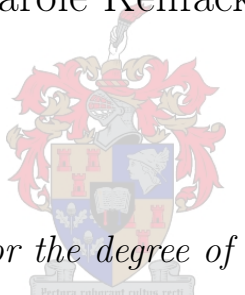

Dissertation presented for the degree of Doctor of Philosophy in Physics in the Faculty of Science at Stellenbosch University

Supervisors:

Prof. Paul Papka

Department of Physics

iThemba Laboratory for Accelerator Based Sciences

Dr Pete Jones

iThemba Laboratory for Accelerator Based Sciences

December 2020

Declaration

By submitting this dissertation electronically, I declare that the entirety of the work contained therein is my own, original work, that I am the sole author thereof (save to the extent explicitly otherwise stated), that reproduction and publication thereof by Stellenbosch University will not infringe any third party rights and that I have not previously in its entirety or in part submitted it for obtaining any qualification.

December 2020

Abstract

Cross section measurement of light ions using (p,xp) and (p,xn) reactions

D. C. Kenfack Jiotsa

Department of Physics

Stellenbosch University

Private Bag X1, Matieland 7602, South Africa

Dissertation: PhD (Physics)

December 2020

The production cross section of light neutron-rich nuclei obtained from a proton induced reaction using light stable nuclei was extracted. The relevancy of such study, away from the valley of stability is oriented toward the understanding of the origin of the elements. Targets of ^{nat}Li, ^{9}Be and ^{nat}B were bombarded by a proton beam in order to produce ^{6,8}He and ^{8,9}Li. The proton beam of energy 50 MeV and 66 MeV was turned on and off during predefined intervals of time using a beam chopper. The beam-on sequence corresponding to the activation time was set long enough to reach secular equilibrium. The beam-off sequence was set to allow at least six decays of the product with the longest half life. The decay rate, hence the production rate of exotic nuclei of interest was evaluated using the Fermi-Kurie plot. The production cross section was deduced and results were compared to theoretical calculations from TALYS.

Measurements were conducted at the Separated Sector Cyclotron facility at iThemba Laboratory of Accelerator Based Sciences (LABS), South Africa. The detection system was composed of two electron spectrometers, mounted following the ΔE-E technique. Each telescope comprised a 5 mm plastic scintillator used to estimate the energy loss and a thin window germanium detector (LEPS) for

residual energy measurement. Such combination of detectors ensured accurate particle identification, while allowing high-resolution measurement.

This project was designed in order to evaluate the feasibility of the production of light neutron rich beams at iThemba LABS using the ISOL (Isotope Separation On-Line) method. Light targets produce lesser species than usual heavier targets, which makes the on-line separation easier. Moreover, nuclei such as boron can be produced in carbide, nitride and oxide forms, known to sustain high temperatures and can be used as a substitute to the uranium carbide in the current design of the ISOL source at iThemba LABS.

Opsomming

Produksie kansvlak metings van ligte kerne deur middel van (p,xp) en (p,xn) reaksies

("*Cross section measurement of light ions using (p,xp) and (p,xn) reactions*")

D. C. Kenfack Jiotsa

Fisika Departement

Universiteit van Stellenbosch

Privaatsak X1, Matieland 7602, Suid-Afrika

Proefskrif: PhD (Fisika)

Desember 2020

Die produksie kansvlak van ligte, neutron ryk, kerne is verkry deur middel van kernreaksies waar protone reageer met stabiele ligte kerne. Hierdie studie op kerne wat te vinde is buitekant die sogenaamde kern vallei van stabilitiet is daarop gemik om vrae rondom die oorsprong van sekere elemente te beantwoord. Teikens bestaande uit ^{nat}Li, ^{9}Be en ^{nat}B is deur protone gebombardeer ten einde ^{6,8}He en ^{8,9}Li te vervaardig. Die kinetiese energie van die proton bundel wat gebruik is in die verskillende metings was 50 MeV en 66 MeV. Tydens die eksperimente is die teikens bestraal met die proton bundel vir voorafbepaalde periodes deur gebruik te maak van 'n bundelkapper. Periodes waartydens die bundel op die teiken toegelaat is word beskou as die aktiverings tydvenster, en is gekies om lank genoeg te wees sodat sekulêre ewewig bereik kon word. Die tydsduur van daaropvolgende periodes sonder bundel was bepaal om ten minste ses keer langer te wees as die langslewende radioaktiewe isotoop se halfleeftyd. Die verval tempo van die kerne wat bestudeer is is bepaal deur middel van die Fermi-Kurie plot. Gevolglik is die produksie kansvlakke bepaal en vergelyk met teoretiese berekeninge wat verkry is deur die kode TALYS.

Experimentele werk is gedoen by die Oop Sekter Siklotron fasiliteit van die iThemba Laboratory of Accelerator Based Sciences (LABS), geleë in Suid Afrika. Twee elektron spektrometers is gebruik tydens die meting. Hierdie detektors, elk bestaande uit 'n 5mm dik plastiese sintillator en 'n dun venster germanium detektor, ook bekend as 'n LEPS detektor, het gebruik gemaak van die ΔE-E tegniek. Hierdie detektor kombinasie het verseker dat verskillende kern deeltjies akkuraat geïdentifiseer word terwyl dit terselfdertyd metings met goeie energie oplosvermoeë moontlik gemaak het.

Die resultate van hierdie projek kan gebruik word om uitspraak te lewer oor die lewensvatbaarheid van die produksie van neutron ryk ligte ioon bundels in die toekoms by iThemba LABS deur middel van die ISOL (Isotope Separation On-Line) metode. Weens die feit dat ISOL teikens bestaande uit ligter kerne 'n kleiner verskydenheid kerne tot gevolg het beteken dit dat die aanlyn skeiding van die radioaktiewe produkte makliker sal wees in vergelyking met swaarder ISOL teikens wat kerne soos uraan bevat. ISOL teikens wat ligter kerne soos boor (B) bevat kan verder makliker vervaardig word met B in karbied, nitried of oksied vorm, wat ook daarvoor bekend is dat dit baie hoë temperature kan weerstaan. Om hierdie redes kan sulke teikens oorweeg word om uraan karbied teikens, wat tans gebruik word, te vervang as ISOL teiken by iThemba LABS fasiliteit.

A mes chéris Zoé et Raphaël

Acknowledgements

I wish to express my deepest gratitude to my supervisors Prof. Paul Papka and Dr Pete Jones for granting me the opportunity to work on this project, and for supporting me throughout its completion. I learned a lot from our discussions and I immensely appreciate your encouragements, patience and guidance.

My extended recognition goes to Dr Frederick D. Smit, Dr Retief Neveling and Dr J.J. van Zyl for always letting their doors open for me. Thank you for taking the time to furnish detailed explanations to my questions and concerns. I would also like to thank Dr Mathis Wiedeking and Dr Deon Steyn for their assistance and support. To the K600 group, the accelerator department and all the colleagues and friends who assisted me during the measurement, from the experimental setting up to taking shifts during the data acquisition process, thank you.

A special thank you to all my friends and colleagues in the students office at iThemba LABS for encouraging me during tough times.

To my dearest and loving husband Thibaut Zafack Takadong. We embarked on this journey together, and you always stood by my side no matter the circumstances. Thank you for the financial and mostly for the emotional support during my moments of doubt; for your understanding; for having to step up and take care of our children whenever I was too busy to play my part. Thank you for your understanding during the late night shifts.

I would like to address an unmeasurable thanks to my parents Joseph and Odile Kenfack. I will not be here without you. To my brothers and sisters, you have put up with me all these years, thank you for been there for me. A special thank you to the Zafack and the Tchimou family for their support and encouragements.

I am very grateful for the financial support allocated for the completion of this project by the South African National Research Foundation (NRF) through the

South African Nuclear Human Asset and Research Programme (SANHARP) Doctoral Scholarships and iThemba Laboratory for Accelerator Based Sciences.

Contents

List of Figures

List of Tables

Chapter 1

Introduction and motivation

The desire of understanding the structure of nuclei away from stability has caused a growing interest in the study of light exotic nuclei in nuclear physics research. A straight-forward definition of an exotic nucleus can be given as a nucleus with an abundance or a deficiency of a specific type of nucleons, as compared to a nucleus of the stable isotope of the same element. This nucleonic specification is more prominent when approaching neutron or proton drip lines. Consequently, nuclei become more and more exotic close to drip lines. Light exotic nuclei are mostly unstable, with short half-lives in the order of milliseconds or even shorter in some cases. When produced, they can be excited depending on the process. They then de-excite to their ground state, and later decay through, most generally a β-decay.

The liquid drop model describes the nucleus as a group of protons and neutrons held together by the combination of the Coulomb and the residual of the strong force. The nuclear force is stronger than the electromagnetic force (Coulomb force) acting as a repulsive force between protons. The nuclear force has a range of interaction of a few femtometers (fm), meaning that nucleons in the nucleus only interact with their close neighbours. For nucleons at the surface of the nucleus, the number of interacting neighbours reduces, causing them to be weakly bound. This means that nuclei with a weak binding energy have a large radius and present a disturbance in their stability. It has been experimentally proven that in an isotopic chain, the probability for a light neutron-rich projectile to interact with a target is greater than that of the stable isotopes. This phenomenon has been observed when bombarding a ^{12}C target with isotopes of lithium at 790

MeV [1]. The interaction cross section of ^{11}Li is higher than for instance that of ^{7}Li and ^{6}Li. This could be explained by the fact that light neutron-rich nuclei have larger radii given that they are weakly bound. The large radius and the non-equilibrium in the neutron and proton densities result in the formation of halos in the nucleus. A neutron-rich nucleus can be described as a stable bound core and some weakly bound valence nucleons. A halo is a state whereby there is a very high probability for these valence nucleons to escape from the nuclear potential of the core. A very good example of a halo nucleus is ^{11}Li with a ^{9}Li core and two valence neutrons. Figure 1.1 shows the position of halo nuclei in the lower section of the nuclear chart [2].

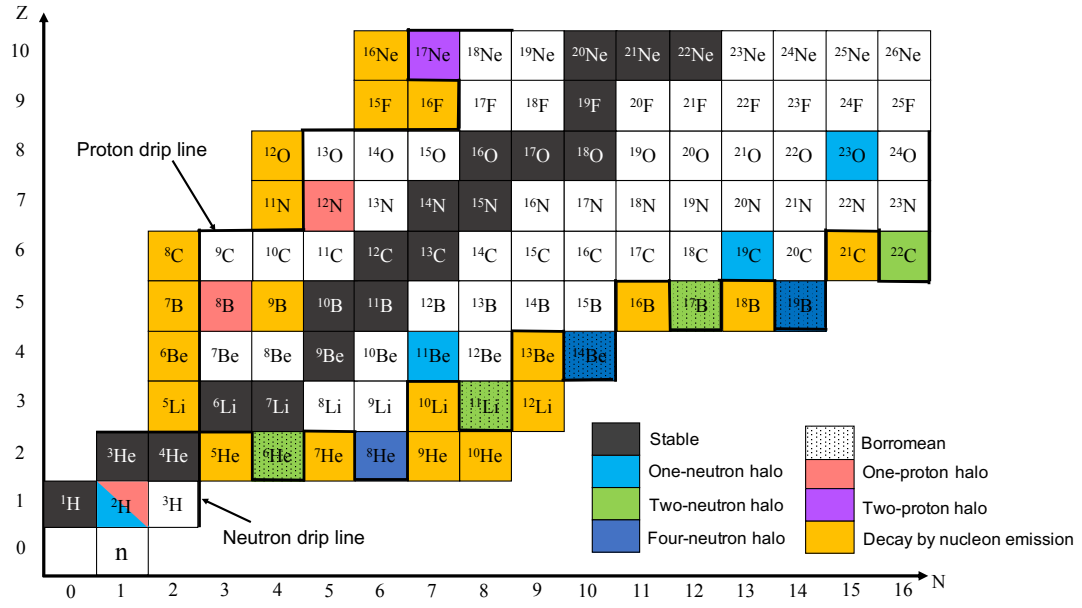

Figure 1.1: Nuclear chart indicating light nuclei with halos.

Halos in light nuclei are sometimes confused with the neutron skin formations. Even though the two phenomena are related to the nuclear radius and the boundedness of neutrons, they are very much different from each other. A neutron-skin is by definition the difference in the root-mean-square (rms) radii between the density distribution of neutrons and protons in the nucleus. A pretty clear distinction between the two could be made by considering their interaction probability [3]. In fact the probability for a halo nucleus to interact with a target is shared between two bodies, the core and the nucleons halo. In a nucleus with a

neutron skin, this same probability is only dependent on one element, that is the whole nucleus.

One cannot address exotic nuclei without including clustering. The formation of clusters made of the lightest nuclei with no excited states such as α-particles (most favourable), deuteron, triton and the helion, can be observed in light neutron rich nuclei. A typical example is ^{8}Be made of two α-particles. The case of ^{7}Li, formed by an α-particle and a triton (t) can also be considered. It needs to be noted that clustering, halo and neutron skin are not the only characteristics observed in light neutron nuclei. They can also display other phenomena such as β-delayed particle emissions and anomalies in level sequences. A β-delayed particle emission corresponds to a β-decay process, followed by the emission of a particle. When an exited state is populated by a β-decay process, if the exited state is above the separation energy of a particle, such particles can be emitted. A β-decay is a weak interaction and as such is slower than other interactions. The fact that the emission of the particle occurs after the decay causes it to be delayed, hence the name β-delayed particle emission.

1.1 Production of light neutron-rich nuclei

To achieve a better understanding of the structure of light exotic ions, they are used as a secondary radioactive beam to bombard stable targets. The analysis of the collision provides a glimpse into the understanding of the properties of exotic nuclei. The secondary radioactive beam is obtained from the product of a primary reaction resulting from the collision between a target and heavy nuclei at high energies, or alternatively a light particle beam.

In recent years, many facilities around the world have developed tools and techniques to produce and study light radioactive beams. The two most common methods of production of light radioactive beams are the fragmentation or In-flight method [4] and the ISOL (Isotope Separation On-Line) method [5]. These two methods rely on the production by a primary reaction of the exotic beam to be directly used in a secondary reaction. The fragmentation method relies on an inverse kinematic reaction. A heavy stable beam is accelerated and impinges on a thin stable target. The beam must have enough momentum for the produced radioactive isotope to acquire the energy needed for the secondary reaction [6].

The fragmentation of heavy nuclei occurs with all participants still in motion. Fragments are collected and separated according to their magnetic rigidity. This method was originally used at BEVALAC accelerator in the 1970's [4] and is now used in facilities like FRIB (Facility for Rare Isotope Beams) at the Michigan State University and RIKEN in Japan.

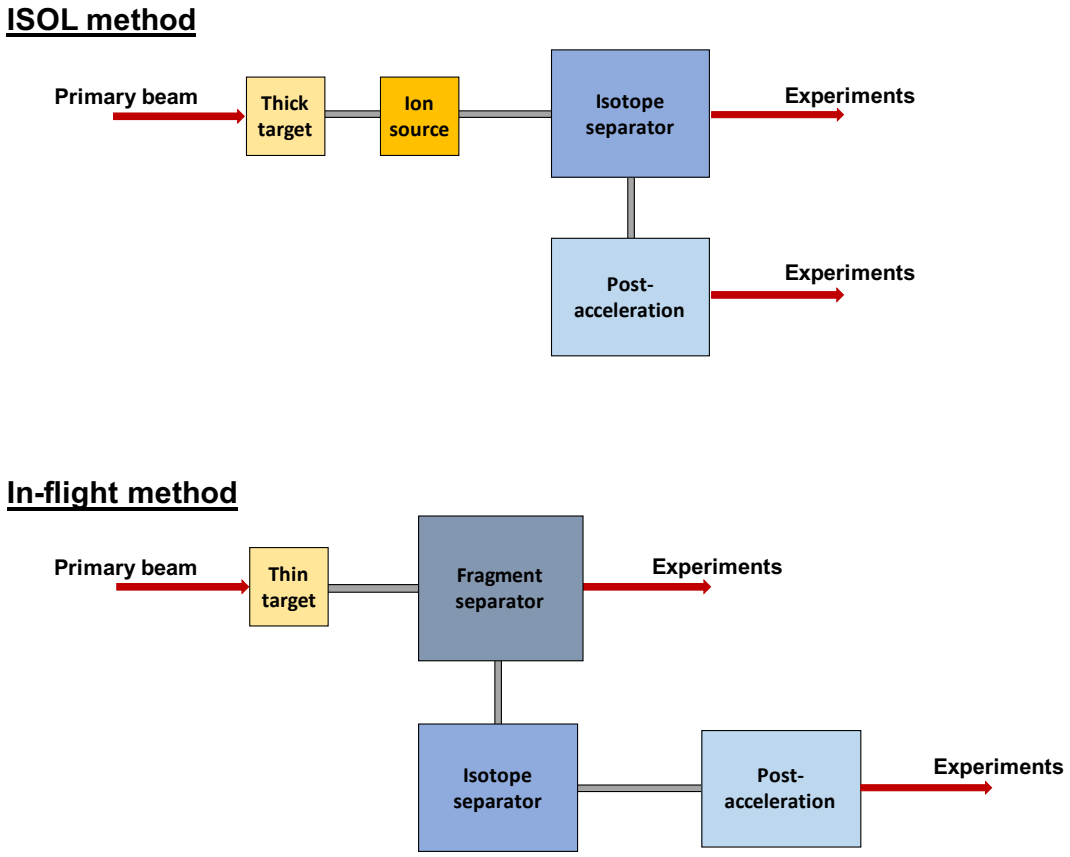

Figure 1.2: Diagram describing the functioning principle of the ISOL and the In-flight isotope production methods.

The ISOL method on the other hand consists of accelerating a high intensity primary beam of protons, deutons or heavy ions, onto a specific target within which reaction products are raised to high temperatures to insure the diffusion of selected species [7]. The target should consist of an element heavier than the radioactive isotope to be produced. Produced ions are sent to an ion source for further selection [5]. Resulting particles are accelerated at an extraction voltage of up to 60 kV, producing a low energy beam, typically at 50-60 keV, which will be

post accelerated to the desired energy. One of the largest facilities using the ISOL method is the ISOLDE Radioactive Beam Facility at CERN [8]. At ISOLDE, a proton beam of about 1 to 1.4 GeV is used in the primary reaction. The available secondary beam consists of more than 600 isotopes from approximately 70 elements [8]. The ISOL method was first developed by Otto Kofoed-Hansen and Karl Ove Nielsen at the Niels Bohr Institute in Copenhagen, in 1951 [9]. For the purpose of this work, the interest is focused on the feasibility study of the production of the radioactive beam using a proton beam on light stable nuclei with the ISOL method.

1.2 Aim of this work

At iThemba Laboratory for Accelerator Based Sciences (LABS), one of the future plans is to put in place an exotic beam production facility under the South African Isotope Facility (SAIF) project [10]. The SAIF facility will consist of two parts: the Accelerator Centre for Exotic Isotopes (ACE Isotopes) and the Accelerator Centre for Exotic Beams (ACE Beams). In ACE Isotopes, the Separated Sector Cyclotron (SSC), with a k-value of 200, currently used for radioisotope production will be replaced by a new commercial high-current 70 MeV cyclotron. The radioisotope production facility based around the 70 MeV cyclotron to be acquired, will insure an increase in the production of radioisotopes and radiopharmaceuticals [11]. The SSC will be entirely dedicated to nuclear physics research. In the ACE Beams project, the SSC will be used as a driver accelerator in the production of radioactive ion beams using the ISOL method. The SSC will produce up to 50 μA of 66 MeV primary proton beam. The first phase of the ACE Beams project has begun with the Low Energy Radioactive Ion Beam (LERIB) facility [10, 12], which will focus mostly on the target handling, the implementation of cooling systems and radiation safety protocols. The second phase of the ACE Beams project will be oriented towards the post acceleration of produced beams.

The current study was conducted in order to investigate the feasibility of the production of light neutron-rich nuclei under the SAIF project. Thereby, cross sections of the production of ^{6,8}He and ^{8,9}Li were measured. These nuclei were produced using light stable nuclei in proton induced reactions. Targets of ^{nat}Li, ^{9}Be and ^{nat}B were bombarded with a proton beam of energies 50 MeV and 66

MeV. To interact with a given material, the proton's energy must be significantly higher than the threshold energy of the reaction of interest. In this case, since the energy is greater than the separation energy of neutrons and protons, from the interaction with nuclei will result multiple reaction channels of type (p,xp) and (p,xn) or even more complex reactions, where x is a factor representing the number of protons or neutrons ejected, for example (p,p), (p,2p) or (p,2n) reactions. The factor x can also stand for another particles produced together with p or n, that is combinations such as (p,αp), (p,np) and so on.

The current design to be implemented at iThemba LABS includes the use of Uranium carbide in the ISOL source. Provided that ^{9}Be and ^{11}B can be used in their oxide, carbide or nitride forms and therefore sustain large temperature amplitudes, they can be used as substitutes to Uranium carbide for the production of light nuclei. Furthermore, using ^{nat}Li which has only one product of interest (^{6}He), ^{9}Be and ^{11}B insures an easier on-line separation process.

Production cross sections were extracted by analyzing the decay of the products. Table 1.1 gives the list of light ions of interest with their β-decay Q-values and half-lives.

Table 1.1: Ions of interest with their half-lives and Q_{β}-values.

Ions	**Half-live [ms]**	**Decay Q-value [MeV]**
^{6}He	806.7	3.5
^{8}He	119	10.6
^{8}Li	840.3	16
^{9}Li	178	13.6

- **Neutron-rich nuclei of interest**

Many elements can be produced from the interaction of ^{nat}Li, ^{9}Be and ^{nat}B with protons. The majority of produced nuclei are weakly bound with short half-lives. Only ^{6}He, ^{8}He, ^{8}Li and ^{9}Li are of interest in this work with ^{8}Li having the longest half-life of 840.3 ms. The lightest among the four is ^{6}He. It is a Borromean nucleus, that is, a nucleus with a halo made of two neutrons. It is one of the most studied halo nuclei, with a half life of 806.89 ms [13], decaying with a β^{-}-disintegration to the ground state of ^{6}Li with a Q-value of 3.508 MeV.

It can also undergo a β-delayed deuteron-emission, which corresponds to a β-decay followed by a break-up into ^{4}He and ^{2}H. The latter reaction channel has a transition probability of $1.42 \times 10^{-6}\,\mathrm{s}^{-1}$ [14], with a decay Q-value of 2.033 MeV. In this work, ^{6}He is obtained from three reactions, ^{7}Li(p,2p), ^{9}Be(p,p^{3}He) and ^{11}B(p,2pα) with a rather high probability and Q-values of -9.96 MeV, -21.17 MeV and -18.64 MeV respectively.

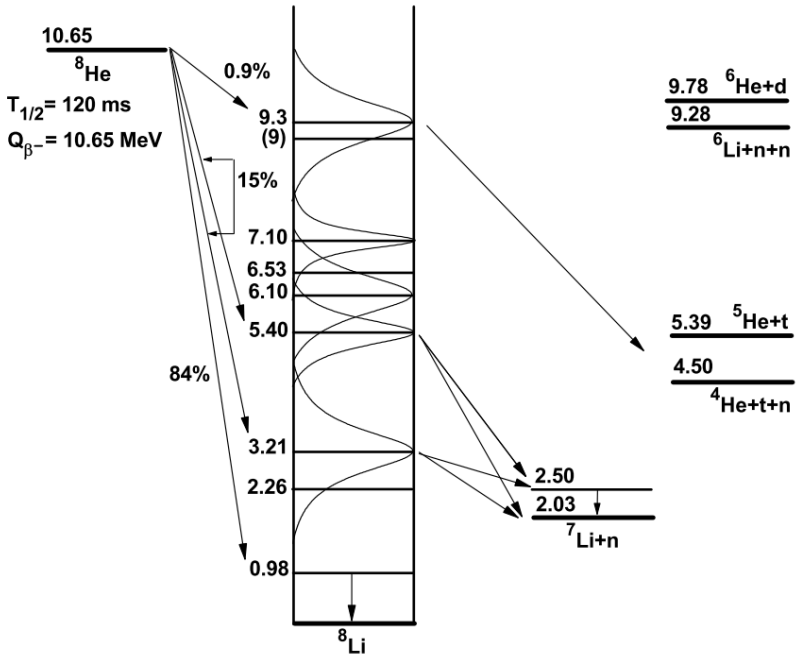

Figure 1.3: Decay scheme of ^{8}He with three branching ratios.

With a very low production rate due to the negatively large reaction Q-value of -45 MeV, ^{8}He is a product of ^{11}B(p,4p). It is a double-Borromean nucleus (four neutrons halo, α+4n) [15] with a very short half live of 119 ms. It β^{-} decays through three channels to the 1^{+} exited states of ^{8}Li as shown in Figure 1.3 [16]. The most probable decay is to the 1^{+} exited state with the excitation energy of 981 keV, with a branching ratio of 84%. This is followed by the de-excitation of ^{8}Li by emission of a 981 keV γ-ray. The remaining 16% corresponds to the decay of ^{8}He to the 3.21, 5.40 and 9.3 MeV 1^{+} states in ^{8}Li.

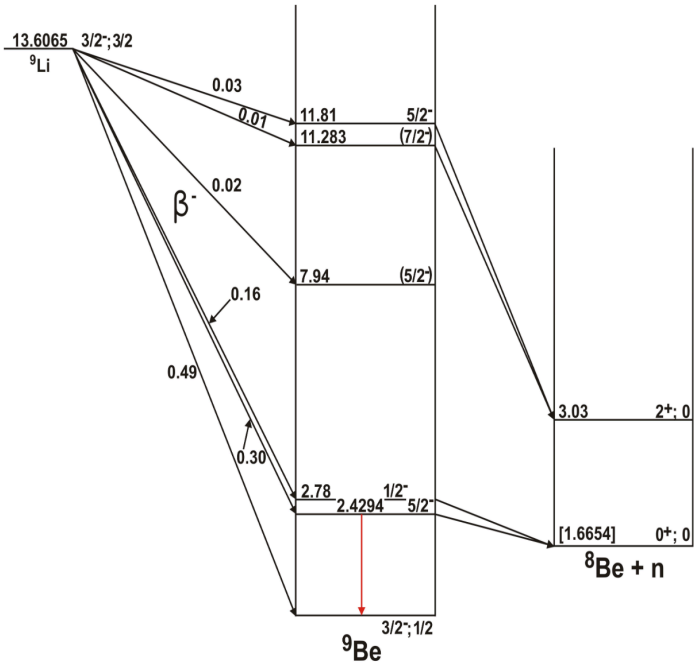

Figure 1.4: ^{9}Li decay scheme [17].

The decay of ^{8}Li is a typical example of β^{-}-delayed α reaction. With a Q-value of 16 MeV, ^{8}Li β^{-} decays to the 2^{+} level of ^{8}Be at $E_x = 3.03$ MeV, which then breaks up into two α particles. Here, ^{8}Li is obtained from ^{9}Be(p,2p) and ^{11}B(p,3pn) with a -17 and -35 MeV Q-value respectively. A nucleus with similar properties to ^{8}Li is ^{8}B, produced here by the ^{9}Be(p,2n) and ^{11}B(p,3np) reactions. It also decays to the 2^{+} level of ^{8}Be following a β^{+}-decay with a decay Q-value of 16.9 MeV.

With a Q-value of 13.6 MeV and a half life of 178 ms, ^{9}Li is produced by the ^{11}B(p,3p). It decays directly to ^{9}Be with branching ration of 49%. The remaining ratio corresponds to a β-delayed neutron emission leading to the ground state of ^{8}B.

1.3 Layout

The work presented in this thesis is the result of an experiment carried out at iThemba LABS in February 2018. Some theoretical background will be introduced in chapter 2, presenting some theories and calculation techniques. The experimental set-up will be previewed in chapter 3, where more details will be

laid out regarding the measuring techniques, the detectors and the facility. The data analysis and processing will be presented in chapter 4, where details on the energy calibration and the energy loss calculations will be advanced, as well as the analysis of data obtained from the bombardment of each target. Chapter 5 will be focused on result presentation and observations. The last chapter will be devoted to the conclusion and the overall summary.

Chapter 2

Theoretical background

2.1 Overview

Some fundamental notions and theories are presented in this chapter. The measurement of the production cross section requires a knowledge of certain parameters such as the number of target nuclei exposed to a number of projectiles, number of events of interest, as well as the type of processes involved in a collision. From the actual reaction to the detection, particles interact with matter at different levels. It is therefore important to understand their behaviour in an absorbing material, both active and passive. Further more, all exotic nuclei in this study undergo a β-disintegration. A brief overview of this process is presented. Fermi's theory of β-decay and the resulting β-particle energy distribution are used to extract events needed in deducing the cross section.

2.2 Interactions of particles with matter

A nuclear reaction occurs when an energetic incident particle interacts with an atomic nucleus. In experimental nuclear physics, the incident particle is called projectile and can be any type of subatomic particle. The atomic nucleus, spatially fixed in most cases, is called the target. A nuclear reaction between a target A and a projectile a is represented by: $A + a \rightarrow B + b$, with a shorthand version $A(a,b)B$, where B and b are the products. If there is a change of the inner structure of A, the reaction is categorised as an inelastic scattering. When

the momentum, and thus direction of the projectile is modified with no change in A, it is an elastic scattering. The Q-value of a nuclear reaction is the difference in energy between the initial and the final state. In other words it is the energy produced by the reaction (if $Q > 0$) or needed for the reaction to take place (if $Q < 0$). When $Q = 0$ the reaction is said to be an elastic scattering.

2.2.1 Cross section

The nuclear cross section is a physical quantity used to determine the probability that under certain conditions, a given nuclear reaction will occur. When a thin sheet of mono-nuclide matter of thickness d, and density ρ, is bombarded by a beam of monoenergetic particles, the probability for a specific reaction to occur is the cross section given by:

$$\sigma = \frac{w}{NI} \tag{2.1}$$

where:

- $N = \rho d N_A/M$ is the area density of nuclei in the sheet, M is the molar mass and $N_A = 6.02{\times}10^{23}$ is Avogadro's number,
- w is the total number of reactions per second also known as the reaction rate and
- I represents the number of incident particles per second. It can be expressed as a function of the beam current I_0, in Ampere (C/s) and the charge of a single particle: $I = I_0/q$ with $q = 1.6 \times 10^{-19}$ C/particles for a proton beam.

The cross section is given in barn (denoted b), 1 b $= 10^{-24}$ cm^2. For a specific type of particle scattered at a solid angle $\Delta\Omega$, the differential cross section is given by

$$\frac{d\sigma}{d\Omega} = \frac{w}{NdI\Delta\Omega} \tag{2.2}$$

Calculations were performed using TALYS [18] in order to predict the cross section of nuclei of interest.

- **TALYS**

TALYS is a computer code used for analysis and simulation of nuclear reactions. It also serves as a database and as such can generate data for all open channels beyond resonance, provided that a range of energy and angle has been predefined by the user. TALYS relies on models such as the optical model, direct reaction, pre-equilibrium model and compound nucleus model, to produce nuclear data [19]. Nuclear reactions are simulated with an energy ranging from few keV to 200 MeV. Projectiles involved are γ rays, protons, neutrons, deuterons, tritons, ^{3}He and α-particles.

In TALYS, optical model calculations are performed by a subroutine called ECIS-06. The Schrödinger equation is numerically solved and observables such as the elastic angular distribution and polarisation, the cross section and s, p-wave strength functions are deduced. This model works mostly for nuclides that are not strongly deformed. In other to include strongly excited scattering and more deformed nuclides, a more general approach is used, that is the coupled-channels method. This formalism falls under direct reactions models which are calculated using the Distorted Wave Born Approximation (DWBA). A direct reaction occurs within approximately 10^{-22} s, corresponding to the time taken by a projectile of energy above $\sim$10 MeV to travel through a target nucleus. For lower energies (below 10 MeV), there is a probability for the target nucleus to capture the projectile and form a compound nucleus. Such a process is slower ($\sim 10^{-18}$ s) and is called compound reaction. The pre-equilibrium reaction is considered as an intermediate reaction type that embodies properties of direct and compound reactions. In TALYS, calculations using models corresponding to direct, compound and pre-equilibrium reactions are performed using both ECIS-06 and DWBA.

To perform calculations using TALYS, an input file is created with information on the beam, the beam energy and the target. An output file is generated with calculated results and information on different reaction channels involved. Additional parameters can be entered in the input file in order to specific a reaction channel for which calculations will be carried out, to specify the model or to organise results in files according to calculated quantities. Many other conditions can be entered depending on the user. Examples of input files are presented in Appendix A.

The cross section of the production of ^{6,8}He and ^{8,9}Li from proton induced reactions on ^{7}Li, ^{9}Be and ^{11}B was calculated using TALYS. Results are reported in Table 2.1 for individual reaction channels leading to the formation of a specific nucleus.

Table 2.1: Cross sections calculated using TALYS for specific reactions producing ^{6,8}He and ^{8,9}Li are listed. The reaction Q-values are also given.

Products	Reactions	Q-values [MeV]	Production cross section [mb]	
			at 50 MeV	at 66 MeV
^{6}He	^{7}Li(p,2p)	-9.96	2.56	1.58
	^{9}Be(p,p^{3}He)	-21.17	1.92	1.04
	^{10}B(p,3pd)	-33.26	4.49×10^{-2}	0.49
	^{10}B(p,2pt)	-24.27	5.30	6.25
	^{11}B(p,2pα)	-18.64	0.64	0.52
	^{11}B(p,pd^{3}He)	-36.99	3.09×10^{-2}	0.31
	^{11}B(p,2p2d)	-42.48	1.58×10^{-5}	0.11
	^{11}B(p,3pt)	-38.45	9.7×10^{-7}	5.22×10^{-3}
^{8}He	^{11}B(p,4p)	-44.81	3.61×10^{-3}	9.73×10^{-2}
^{8}Li	^{9}Be(p,2p)	-16.89	12.73	6.93
	^{10}B(p,3p)	-23.47	4.05	4.61
	^{11}B(p,n3p)	-34.93	0.17	2.41
	^{11}B(p,2pd)	-32.70	0.73	2.34
	^{11}B(p,p^{3}He)	-27.21	0.71	0.47
^{9}Li	^{11}B(p,3p)	-30.86	0.12	0.23

2.2.2 Interaction of photons with matter

When electromagnetic radiation interacts with matter, many types of reactions can occur. Only three of these reactions are often considered in experimental physics, the Photoelectric effect, Compton scattering and Pair-production.

- **Photoelectric effect**

The photoelectric effect is the emission of an electron by matter after the absorption of the energy of electromagnetic radiation (X-rays or γ rays). The emitted

photoelectron has kinetic energy T_{e^-}, given by:

$$T_{e^-} = h\nu - E_b, \tag{2.3}$$

where $h\nu$ is the energy of the incident radiation and E_b is the binding energy of the electron.

- **Compton scattering**

An incident photon of energy $h\nu$ can be deviated by an angle θ from its original trajectory after hitting a loosely bound electron in matter. The photon transfers some of its energy to the electron which is ejected. This process is called Compton scattering. The ejected electron is called a recoil electron and the new acquired energy of the photon, $h\nu'$ is expressed as follows:

$$h\nu' = \frac{h\nu}{1 + \frac{h\nu}{m_0c^2}\,(1 - cos\theta)} \tag{2.4}$$

The rest mass of the electron is given by $m_0c^2 = 0.511$ MeV. The kinetic energy T_{e^-} of the recoil electron can also be obtained,

$$T_{e^-} = h\nu - h\nu' = h\nu\left(1 - \frac{1}{1 + \frac{h\nu}{m_0c^2}\,(1 - cos\theta)}\right) \tag{2.5}$$

- **Pair production**

At high energies, greater than twice the rest mass of the electron ($h\nu \geq 2m_0c^2$), photons are gradually more likely to interact with matter via pair production with increasing incident energy. During this process, the incident γ ray is converted into an electron-positron pair inside the atomic nuclear field. Its energy is equally shared between the electron and the positron in the form of kinetic energy. The total energy of the pair is therefore $T_{e^-} + T_{e^+} = h\nu - 2m_0c^2$. Since the process takes place in the vicinity of the nucleus, the latter is considered as a third body, in addition to the electron-positron pair. The conservation of momentum is therefore satisfied, taking into account the recoil of the nucleus.

The interaction of the positron and an atomic electron will result in the formation of two annihilation photons of 0.511 MeV each. If both annihilation photons

escape from the detector, on the energy spectrum, a peak called double escape peak will be observed at $2m_0c^2$ below the incident gamma energy peak. In some cases, only one annihilation photon will be absorbed. A single escape peak will therefore form at 0.511 MeV below the photopeak.

2.2.3 Interaction of charged particles with matter

The interaction of charged particles with an absorbing material can be categorised as both electronic and nuclear. In the former case, the interaction can be an excitation, where atomic electrons are ejected from their initial orbitals and can find themselves in a higher atomic shell, or it can be an ionization and in that case they are completely removed from the atom. Since atomic nuclei occupy less of the atom's volume (the nuclear volume is about 15 orders of magnitude less than the atomic volume), their interaction with the incident particles have a very small effect and is often neglected.

As the particles traverse the material, charge particles will lose some or all of their energy depending on the density and thickness of the material. The stopping power is the ability for an absorbent to cause a particle passing through it to lose all or part of its incident energy. It is given as a function of quantities such as the density of the absorbing material, the velocity of incident charged particles, as well as the atomic masses of both the absorbing material and incident charged particles. The stopping power is denoted $-dE/dx$, where dE represents the energy loss and dx the thickness per unit areal density of the material.

2.2.3.1 Protons and α-particles

Protons and α-particles lose energy in matter mainly by ionization or excitation of the atoms of the material called collision energy losses. These interactions are caused by the Coulomb forces acting between the incident particles and atomic electrons. When protons and α-particles travel through matter, they continuously interact with electrons along their path. The total stopping power is given by the Bethe-Bloch formula [20] and is mostly due to collision energy losses.

$$-\frac{dE}{dx} = 4\pi n z^2 r_e^2 \frac{m_0 c^2}{\beta^2}\left[ln\left(\frac{2m_0c^2\beta^2}{I\left(1-\beta^2\right)}\right) - \beta^2\right] \tag{2.6}$$

where:

- $\beta = \frac{v}{c}$ is the relative velocity to light of incident particles;
- I is the mean excitation energy;
- m_0c^2 is the rest mass of the electron = 511 keV;
- z is the number of charge of the incident particle in C;
- $n = \frac{N_A Z \rho}{A}$ is the electron density of the absorbing material, with Z, A and ρ being the atomic number, the mass number and density of the absorbing material respectively, and N_A the Avogadro's number;
- $r_e = \frac{e^2}{4\pi\epsilon_0 mc^2}$ is the classical electron radius.

It is observed form Equation 2.6 that the energy loss of a charged particle in matter depends on the velocity and charge of the incident material, and the electron density n of the absorbing material. Protons and α-particles are considered non-relativistic ($v << c$). Since the stopping power is inversely proportional to the velocity of the incident particle, they will lose more energy in the material. Highly charged particles will lose more energy in the material. This leads to the conclusion that in the same absorbing material, α-particles will lose energy at a higher rate than protons. Also, the larger the electron density n in a material, the larger its stopping power. Figure 2.1 shows the stopping power of a germanium crystal for protons and α-particles. It can be observed that α-particles lose more energy going through germanium than protons.

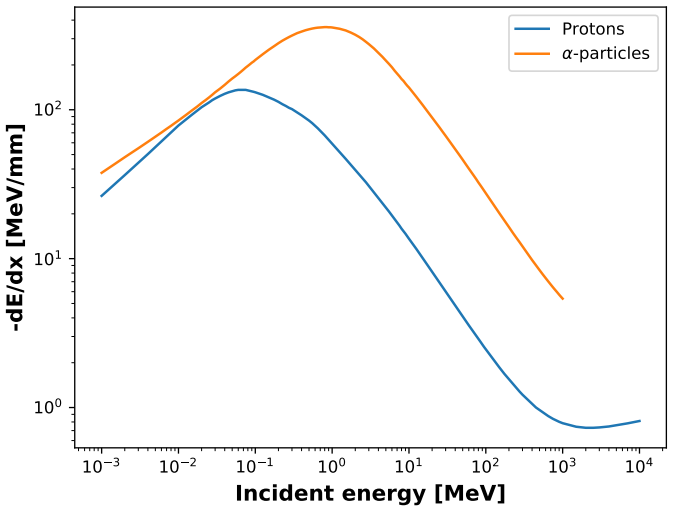

Figure 2.1: Energy loss of protons and α-particles in germanium. Protons lose less energy going through the material than α-particles.

2.2.3.2 Electrons and positrons

During the passage of an electron through matter, three types of processes can take place. It can undergo an elastic collision with change in direction, an inelastic collision accompanied by the excitation of the electron or the ionization of the atom, or an emission of radiation in the vicinity of the nucleus. In the latter case, the electric field of the nucleus causes the incident electron to emit electromagnetic radiation (Bremsstrahlung), causing a deflection from its original path. This type of energy loss is the radiation energy loss.

The collision energy loss is more prominent at low energies (up to approximately 10 MeV) and almost non-existent at high energies (higher than 10s of MeV). On the other hand, the radiation energy loss increases with an increase of the incident energy. Low energy electrons lose their energy in matter like protons and α-particles. β-particles can reach relativistic speeds (energies $> m_0c^2$) so some very high radiation energy loss should be observed. The collision stopping power for fast electrons is obtained by correcting the Bethe-Bloch formula for

particle energies $> m_0c^2$. Both stopping powers are expressed as follow [21, 22],

$$-\left(\frac{dE}{dx}\right)_{collision} = 2\pi n r_e^2 \frac{m_0c^2}{\beta^2}\left(ln\frac{m_0c^2\beta^2E}{2I^2(1-\beta^2)} - \left(2\sqrt{1-\beta^2} - 1 + \beta^2\right)ln2 + 1 - \beta^2 + \frac{1}{8}\left(1-\sqrt{1-\beta^2}\right)^2\right) \tag{2.7a}$$

$$-\left(\frac{dE}{dx}\right)_{radiation} = \frac{nZ}{137}r_e^2E\left(4ln\frac{2E}{m_0c^2} - \frac{4}{3}\right). \tag{2.7b}$$

The ratio of the collision and the radiation stopping power can be approximated to

$$\frac{-\left(\frac{dE}{dx}\right)_{collision}}{-\left(\frac{dE}{dx}\right)_{radiation}} = \frac{EZ}{1600m_0c^2}. \tag{2.8}$$

The critical energy E_c is the energy at which the radiation energy is equal to the collision energy and is given by

$$E_c = \frac{1600m_0c^2}{Z}. \tag{2.9}$$

In a germanium crystal, the critical energy is equal to 25.5 MeV. For a plastic scintillator, it is 6.9 MeV. The total energy loss of electrons and positrons in matter is the sum of the collision and the radiation energy loss.

$$\frac{dE}{dx} = \left(\frac{dE}{dx}\right)_{collision} + \left(\frac{dE}{dx}\right)_{radiation}. \tag{2.10}$$

The stopping power of a germanium crystal to the passage of electrons (or positrons) is shown in Figure 2.2. It represents the comparison between the stopping power obtained using Equation 2.6 (pure Bethe-Bloch formula), with electron parameters, and the stopping power obtained using Equation 2.10 . It can be observed that, the first case corresponds mostly to the collision stopping power. Taking into account the radiative nature of electrons in the neighbourhood of the nucleus, the correct version of the stopping power for electron is obtained.

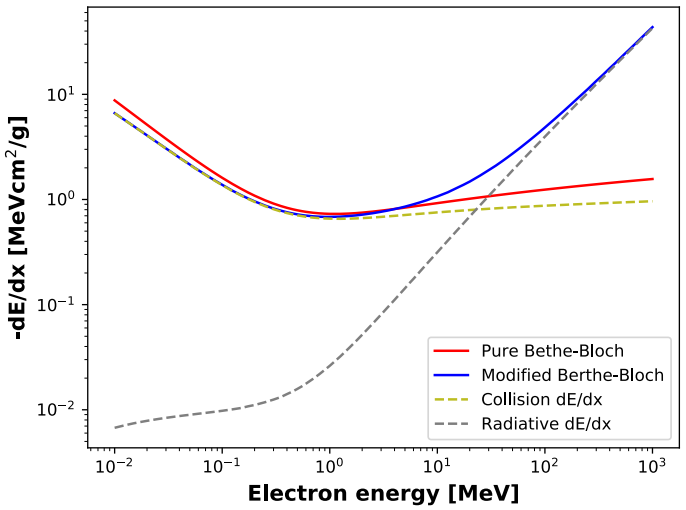

Figure 2.2: Effect of the radiative energy loss to the total energy loss of electrons (or positrons) in a germanium crystal. The Bethe-Bloch formula adapted to electrons (or positrons) corresponds mainly to the collision stopping power.

2.3 Radioactive decay

2.3.1 Radioactivity

Radioactivity is a process whereby unstable nuclei spontaneously transform or decay into other nuclei by emitting secondary particles and energy. Even though it is impossible to predict exactly at what specific time the decay will happen, it is however possible to express the number of particles dN decaying in an interval of time dt,

$$\frac{dN}{dt} = -\lambda N \Rightarrow N(t) = N_0 e^{-\lambda t}. \tag{2.11}$$

The negative sign here indicates that the initial number of particles, N_0 (number of particles at $t = 0$), decreases with increasing time. The decay constant λ is also known as the decay rate. It is the probability that a nucleus will decay after each second. The decay constant is given in unit s^{-1}. It is inversely proportional to the half-life $t_{1/2}$, that is the time within which half of the initial number of particles will decay, thus:

$$\lambda = \frac{ln2}{t_{1/2}}. \tag{2.12}$$

An example of a decay curve is presented in Figure 2.3. It shows the decay curve of ^{6}He obtained from the ^{7}Li(p,2p) reaction. This is observed during a decay time of 5 s. When fitted with an exponential function, the measured decay constant is $\lambda = 0.86 \pm 0.1$ s^{-1} , corresponding to a half-life of 805 ms.

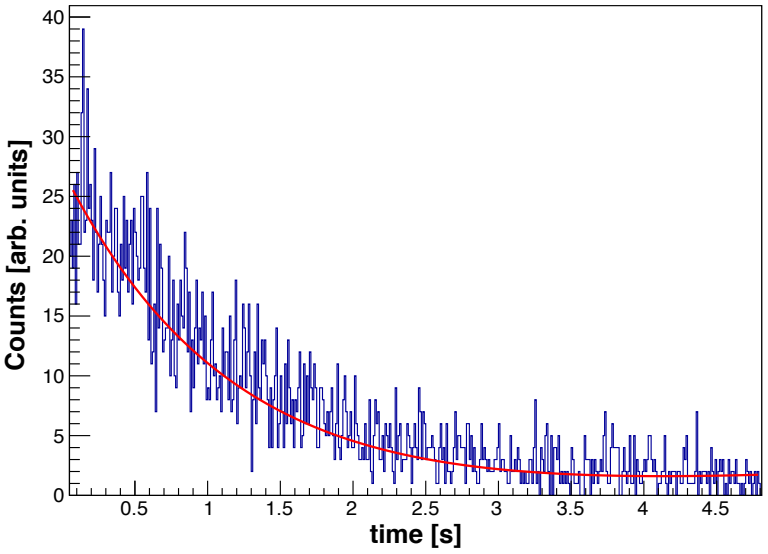

Figure 2.3: Decay curve of ^{6}He.

2.3.2 Radioactive growth

Assuming the product B of a reaction of type $A(a,b)B$ is a radioisotope decaying into a nucleus C, the number N_B of B at time t depends on the number of B produced and the number of B that have decayed into C by that time. Thus, the rate of change of N_B at time t is given as a function of its production rate w and its decay rate.

$$\frac{dN_B}{dt} = w - \lambda_B N_B \Rightarrow N_B(t) = \frac{w}{\lambda_B}\left[1 - e^{-\lambda_B t}\right]. \tag{2.13}$$

w is the same production rate used in the production cross section expression, that is $w = \sigma N I$. If the decay product, C, is stable, its production rate will be equal to the decay rate of B, $\lambda_B N_B$. If on the other hand C decays with a decay constant λ_C, the rate of change of N_C at time t is expressed as follow:

$$\frac{dN_C}{dt} = \lambda_B N_B - \lambda_C N_C, \tag{2.14}$$

where N_B is given by Equation 2.13. Substituting Equation 2.13 in Equation 2.14, a linear differential equation of the first order is obtained. This equation is solved using the method of the variation of a constant, with the condition that at t=0 (at the beginning of the decay of B), N_C=0. The number of C at a given time t is therefore deduced and expressed by Equation 2.15.

$$N_C(t) = \frac{w}{\lambda_C\left(\lambda_C - \lambda_B\right)}\left[\lambda_C\left(1 - e^{-\lambda_B t}\right) - \lambda_B\left(1 - e^{-\lambda_C t}\right)\right]. \tag{2.15}$$

Hence a decay rate

$$R_C(t) = \frac{w}{\lambda_C - \lambda_B}\left[\lambda_C\left(1 - e^{-\lambda_B t}\right) - \lambda_B\left(1 - e^{-\lambda_C t}\right)\right]. \tag{2.16}$$

When comparing the half-life $t_{1/2}(B)$ of the parent nucleus B and the half-life $t_{1/2}(C)$ of the daughter nucleus C, three different scenarios are often observed.

- **No equilibrium**

In this case, $t_{1/2}(B) < t_{1/2}(C)$, that is $\lambda_B > \lambda_C$. Due to the fast decay of B, the activity of C increases rapidly to reach a maximum value after which it decays with its decay constant λ_C.

- **Transient equilibrium**

This corresponds to a situation where $t_{1/2}(B) > t_{1/2}(C)$, that is $\lambda_B < \lambda_C$. In such a case, as time increases, the total activity is governed by the activity B. The decay of C is dictated by its formation, which depends on a slower decay rate of B. This leads to the impression that the daughter nuclei C decays with the decay constant of B.

- **Secular equilibrium**

Here, $t_{1/2}(B) >> t_{1/2}(C)$. This situation is similar to the previous with the difference that when the time t becomes longer than the half-life of C, the formation rate of the latter becomes equal to its decay rate ($dN_C/dt = 0$).

Equations 2.13 and 2.15 describe a situation where the production of B is continuous. In most cases, when studying the decay of the product of a nuclear reaction, the target is irradiated during a defined time after which the beam of

projectiles is turned off and the product is allowed to decay. For the purpose of this work, the beam was switched on during a time t_{on} and off for a time t_{off}, as illustrated in Figure 2.4.

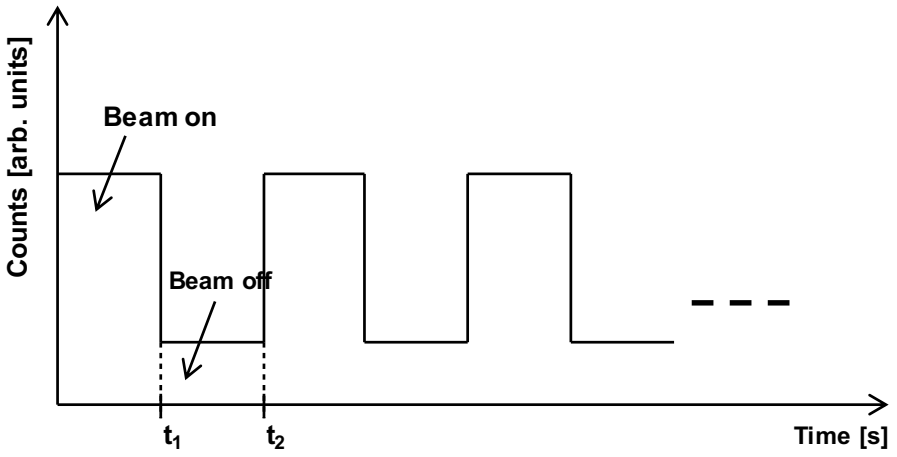

Figure 2.4: A schematic illustration of the beam on-off cycles.

In such case, the beam-on sequence is characterised by the production and the decay of B. This will be accompanied by the production of C if $t_{on} > t_{1/2}(B)$, and the decay of C if it is unstable. During the beam-off sequence, the production of B is stopped and the only activity is due to decay processes. The maximum number of B is obtained at saturation and is given by $N_B(max) = w/\lambda_B$. In practice, saturation is reached after a time t_{on} corresponding to at least three half-lives of the nucleus in question. Above this time, the number of B remains constant until the beam is turned off, where it decreases exponentially.

At the end of the beam-on sequence, if t_{on} is longer than a half-life but not enough for the number of B to reach saturation, the decay rate of B can be written as:

$$R_B(t_{on}) = w\left[1 - e^{-\lambda_B t_{on}}\right]. \tag{2.17}$$

During the beam-off sequence, the production of B is stopped. It however continues to decay with an initial activity equal to $R_B(t_{on})$. The decay rate of B at the end of the beam-off sequence is

$$R_B(t_{off}) = w\left[1 - e^{-\lambda_B t_{on}}\right] e^{-\lambda_B t_{off}}. \tag{2.18}$$

In a similar way, the number of C after t_{off} is given by

$$R_C(t_{on}) = \frac{w}{\lambda_C - \lambda_B}\left[\lambda_C\left(1 - e^{-\lambda_B t_{on}}\right)e^{\lambda_B t_{off}} - \lambda_B\left(1 - e^{-\lambda_C t_{on}}\right)e^{\lambda_C t_{off}}\right]. \tag{2.19}$$

In some cases, a radionucleus can decay into two or more nuclei. For instance, consider B decaying into C and D with decay constants $r\lambda_B$ and $r'\lambda_B$ respectively. The branching ratios r and r' represent the probability of B decaying respectively into C or D $(r + r' = 1)$. Here, the approach used in determining the decay rate of daughter nuclei is similar to the previous case with the difference that for each branch the decay rate is multiplied by the branching ratio. A situation can appear where B and C are products of nuclear reactions with cross sections σ and σ' respectively, with corresponding production rates w and w'. Meaning that the activity of C does not depend entirely on the decay of B. Such a case can be represented by the following diagram.

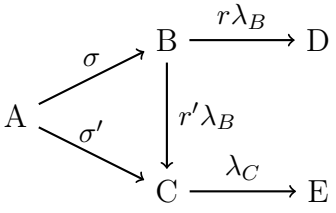

Figure 2.5: Schematic representation of a reaction with two decaying products.

The rate of change of B is expressed as in Equation 2.13 and that of C is determined by

$$\frac{dN_C}{dt} = w' + \lambda_B N_B - \lambda_C N_C. \tag{2.20}$$

Leading to the decay rate

$$R_C(t_{on}) = rw\left[\left(1 - e^{-\lambda_2 t_{on}}\right) - \frac{\lambda_2}{\lambda_2 - \lambda_1}\left(e^{-\lambda_1 t_{on}} - e^{-\lambda_2 t_{on}}\right)\right] + w'\left(1 - e^{\lambda_C t_{on}}\right). \tag{2.21}$$

2.3.3 β-decay

2.3.3.1 Fermi gas model

The definition and origin of the β-decay process are well presented using the Fermi gas model. The assumption behind the Fermi gas model is that nucleons in a nucleus are found at different energy levels. The nucleus can be described as a collection of fermions freely moving in a potential well without interacting with each other. Fermions are particles with spins of 1/2, such as electrons, protons and neutrons, that follow Pauli's Exclusion Principle. According to this principle, no more than two particles can find themselves on the same energy level. Moreover, said particles must have opposite spin. Since protons and neutrons are two distinct type of fermions, they are found in different potential wells. The highest occupied energy level is called the Fermi Energy. For a stable nucleus, the Fermi energy must be the same for protons and neutrons in a given nucleus. The potential well of neutrons is deeper than that of protons since neutrons are not affected by the Coulomb repulsion force. At the ground state, the distribution of nucleons in the nucleus is similar to the configuration presented in Figure 2.6. $E_{F,n}$ and $E_{F,p}$ represent the Fermi energy for neutrons and protons respectively. B/A is the average binding energy per nucleon. The depth of the potential well is given by: $V_0 = E_{F,i} + B/A$, where i stands for neutrons n or protons p.

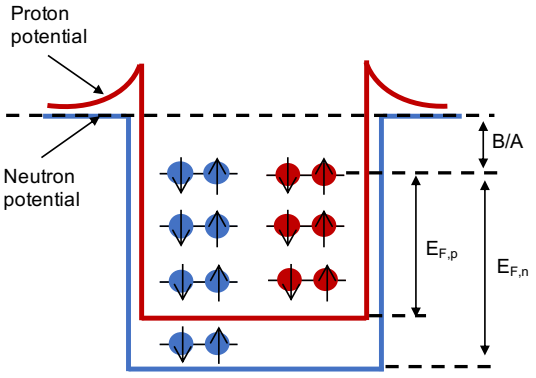

Figure 2.6: Neutrons are represented in blue and protons are in red. The highest occupied level is the same for neutrons and protons. This figure is just for illustrative purposes and does not represent a specific nucleus.

Nuclei in their natural state tend to adopt a more stable configuration. In the case of unstable nuclei, one type of fermions is in excess. The Fermi energy

of the excess nucleon type is higher. The stability of the nucleus is therefore compromised. If the number of protons exceed the number of neutrons, there is a probability for a proton to be converted into a neutron in order to restore the equilibrium. Similarly, if neutrons are in excess, a neutron could be converted into a proton. This process can be illustrated by Figure 2.7 where a neutron in ^{11}Be (unstable) is converted into a proton, such that the system can adopt a more stable configuration, that is ^{11}B. This process is the β-decay process.

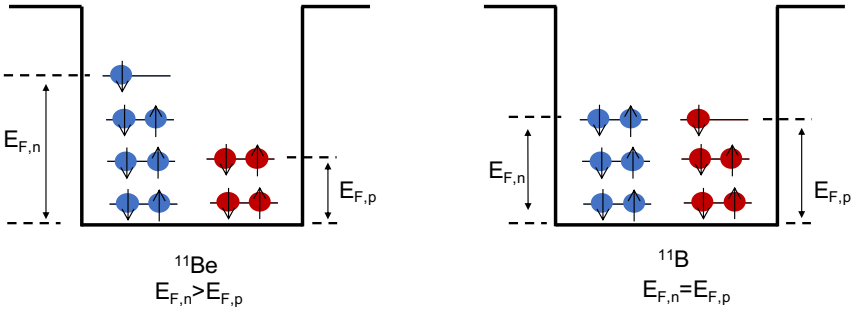

Figure 2.7: The excess neutron causes the neutron potential to have a higher Fermi energy. The neutron at the higher energy level is converted into a proton that occupies a new energy level in the proton well.

In a case whereby the excess neutron is converted into a proton, the process is a β^--disintegration and is accompanied by the emission of an electron and an anti-neutrino $\bar{\nu}$. When a proton is converted into a neutron, it is a β^+-disintegration and a positron and a neutrino ν are emitted. Neutrinos and anti-neutrinos are fermions, which presence in the decay process ensures the conservation of energy, momentum and angular momentum. The β-decay process is represented by the following statements:

$$n \rightarrow p + e^- + \bar{\nu} \tag{2.22}$$

$$p \rightarrow n + e^+ + \nu. \tag{2.23}$$

A third process can be observed whereby, an orbital electron, from any shell (K, L, M, ...), is absorbed by the nucleus and a neutrino is emitted. This case is known as electron capture.

$$^A_Z X + e^- \rightarrow {}^A_{Z-1}Y + \nu. \tag{2.24}$$

As a consequence of the β-decay process, the number of charge Z of the parent nucleus X is changed into Z+1 to form the daughter nucleus Y for a β^--decay and into Z-1 for a β^+-decay and electron capture.

2.3.3.2 Fermi's theory of β-decay

Enrico Fermi developed in 1934 [23] the idea based on the premise that the number of decays per unit time, known as the decay probability (also called transition probability or transition rate or decay rate) λ, can be expressed as a function of the interaction H, that causes the transition between an initial and a final state. This statement is known as Fermi's golden rule,

$$\lambda = \frac{2\pi}{\hbar}|H_{if}|^2\rho(E_f). \tag{2.25}$$

$\rho(E_f) = dn/dE_f$ is the density of the final state with energy E_f and H_{if} is the interaction matrix element given by: $H_{if} = \langle\Psi_f|\hat{H}|\Psi_i\rangle = gM_{if}$. Ψ_i and Ψ_f are the wave functions of the initial and final states respectively. M_{if} is the nuclear matrix element and g is a constant determining the strength of the interaction that gives rise to the emission, $g = 10^{-48}$ to $10^{-49} gcm^5s^{-2}$. This interaction is called the weak interaction and is characteristic of the interaction of subatomic particles causing radioactive decays. A weak interaction, where a neutron is converted into a proton and vice versa, through the emission of an anti-neutrino and an electron or a neutrino and a positron, is analogous to an electromagnetic interaction with the emission of a photon by an electron (the constant g is the equivalent of the fine-structure constant α in an electromagnetic interaction).

During a β-decay, the probability, dn, of having an electron of momentum between p and $p + dp$, and a neutrino of momentum between q and $q + dq$, at a solid angle Ω, is given by

$$dn = \frac{p^2dp}{2\pi^2\hbar^3} \cdot \frac{q^2dq}{2\pi^2\hbar^3} \cdot \Omega^2. \tag{2.26}$$

Following the steps as demonstrated in Fermi's lecture at Chicago University [24], and considering that the relativistic approximation according to which the maximum momentum p_{max} (with $p_{max} = (1/c)\sqrt{Q^2 + 2Qm_0c^2}$) is obtained when the number of neutrinos is zero, the transition probability per unit time is obtained

as

$$d\lambda = N(p)dp = \frac{g^2}{2\pi^3\hbar^7c^3}|M_{if}|^2p^2\left[Q - \sqrt{p^2c^2 + (m_0c^2)^2} + m_0c^2\right]^2 dp, \quad (2.27)$$

where $N(p)$ is the intensity of emission of β-particles. The total decay rate and the lifetime can be deduced,

$$\lambda = \frac{1}{\tau} = \int_0^{p_{max}} N(p)dp.$$

This is obtained by considering only the wave function distribution of the electron. Taking into account the wave function distribution by the Coulomb field of the nucleus, a factor $F(Z,p)$ needs to be introduced in Equation 2.27. $F(Z,p)$ is called the Fermi function and accounts for the Coulomb force, resulting from the attraction of electrons or repulsion of positrons by the nucleus. It is expressed as followed:

$$F(Z,p) = \frac{\eta}{1 - e^{-\eta}}. \quad (2.28)$$

with $\eta = \pm\frac{2\pi Zc}{137v}$ and Z here is the atomic number of the daughter nucleus. The shape of electron or positron energy spectrum and thus the intensity of emission can be given as a function of the momentum p,

$$N(p) = C|M_{if}|^2F(Z,p)\left[Q - \sqrt{p^2c^2 + (m_0c^2)^2} + m_0c^2\right]^2 \quad (2.29)$$

or as a function of the kinetic energy T_e of electrons (or positrons).

$$N(T_e) = C|M_{if}|^2F(Z,T_e)p^2\sqrt{T_e^2 + 2T_em_0c^2}(Q - T_e)^2(T_e + m_0c^2). \quad (2.30)$$

The intersection of the energy spectrum distribution with the horizontal axis at $T_{e_{max}} = Q$ is called the endpoint. Figure 2.8 shows the electron energy spectrum for the decay of ^{6}He into ^{6}Li with the endpoint at 3.5 MeV. This calculation was performed using the Spectroscopic Calculator [25] code in Lise++ [26].

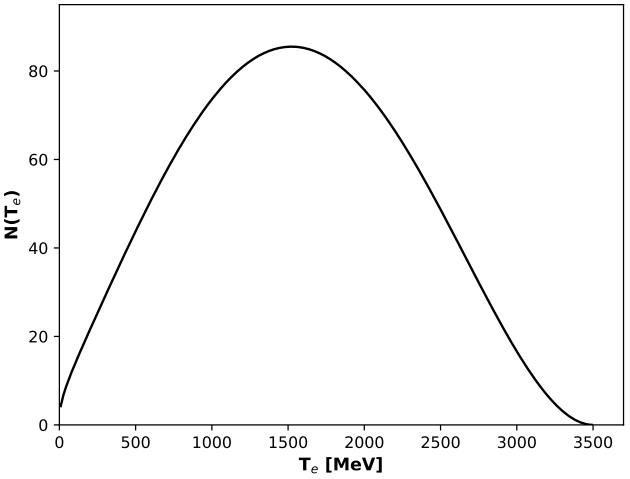

Figure 2.8: Electron spectrum of the decay of ^{6}He obtained using Lise++.

2.3.3.3 Kurie plot

At the endpoint, the energy curve is tangential to the horizontal axis. This makes it experimentally difficult to accurately determine the endpoint value. A more suitable approach could be using the Fermi-Kurie plot, which consists of plotting $\sqrt{\frac{N(p)}{p^2 S(Z,p)}}$ against the energy T_e. This is obtained by rewriting Equation 2.29 as follow:

$$K(T_e) = Q - T_e \quad \propto \quad \sqrt{\frac{N(p)}{p^2 S(Z,p)}}. \tag{2.31}$$

$S(Z,p)$ represents the constants and the nuclear charge dependency in Equation 2.29. The Fermi-Kurie plot of the decay of ^{6}He is shown in Figure 2.9, with the endpoint at 3.5 MeV.

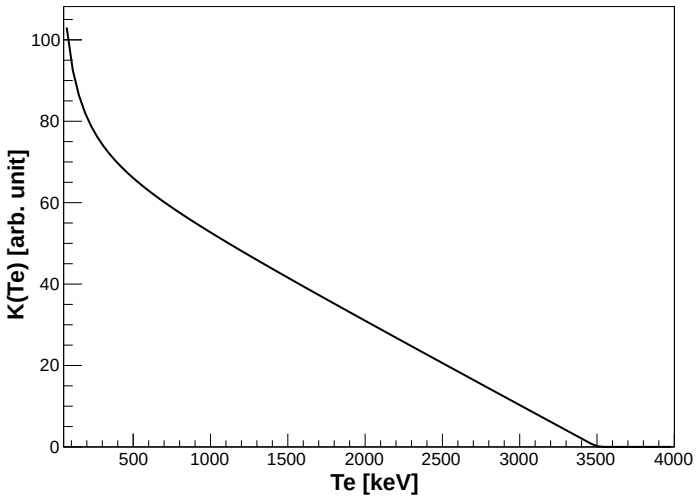

Figure 2.9: Fermi-Kurie plot of the decay of ^{6}He.

2.3.3.4 Selection rules for beta decay

The angular momentum in a β-disintegration is conserved. All fermions present here have a spin -1/2, which makes the relative spin of the electron (or positron) and the anti-neutrino (or neutrino), S_β, to have only two possibilities of values, 0 and 1. Two theories are developed around these possibilities. The first one uses the Fermi approach for which $S_\beta = 0$ and the second approach is the one of Gamow-Teller where $S_\beta = 1$. According to Fermi, the Hamiltonian responsible for the β-decay is not influenced by the heavy particles involved in the process, but rather by the leptons. Gamow and Teller [27] on the other hand support the idea according to which spins of leptons are identical and therefore the interaction depends on the parent and daughter nuclei.

The conservation of angular momentum gives $\Delta\vec{J} = \vec{S_\beta}+\vec{L_\beta}$, with $\vec{L_\beta}$ representing the orbital angular momentum of the leptons. $\Delta\vec{J} = \vec{J_P} + \vec{J_D}$, where $\vec{J_P}$ and $\vec{J_D}$ are the total angular momenta of the parent and the daughter nuclei respectively. The parity is also given by $\pi_P = \pi_D(-1)^{L_\beta}$. These two equations form the selection rule for a β-decay. This gives a classification of the β-decay process in terms of super-allowed, allowed and forbidden decays. Different combinations are itemised in Table 2.2, with $\Delta\pi$ representing the change in parity between the parent and the daughter nucleus.

Table 2.2: Selection rule in β-decay

Type of process	$\vec{L_\beta}$	$\Delta\pi$	$\Delta\vec{J}$ for Fermi	$\Delta\vec{J}$ for Gamow-Teller
Super-allowed	0	+	0	0
Allowed	0	+	0	0, 1
1^{st} forbidden	1	-	0, 1	0, 1, 2
2^{nd} forbidden	2	+	1, 2	1, 2, 3
3^{rd} forbidden	3	-	2, 3	2, 3, 4
4^{th} forbidden	4	+	3, 4	3, 4, 5

To have an estimation of the value of the matrix element $|M_{if}|$, it is important to know the type of transition involved in the decay reaction. For instance, $M_{if} = 0$ for a first forbidden transition and $M_{if} = \sqrt{2}$ for a super-allowed transitions. The illustration in Figure 2.8 was obtained for an allowed transition.

2.4 Radiation detection

2.4.1 Overview on high purity germanium detectors

2.4.1.1 Semiconductors

The two main bands involved in a material conductivity characterisation are the valence and the conduction bands. These bands are made of levels occupied by electrons in the material and are separated by a band gap also called the forbidden band, where electrons are forbidden. The band gap helps determine if the material is an insulator or a semiconductor. The valance band is made of electrons bound in specific lattices in the material; always full in semiconductors. The conduction band on the other hand is made of electrons that are free to navigate through the material.

A pure or intrinsic crystal has a full valence band and an empty conduction band at zero thermal energy. With the presence of thermal excitation, electrons can jump from the valence to the conduction band, leaving empty spaces (holes) behind. A wave of holes is created in the valence band as vacant spaces are filled by nearby electrons. An equilibrium is reached when the number of electrons in the conduction band is equal to the number of holes in the valence band. These holes

and new conduction electrons constitute the charge carriers of the semiconductor and contribute in the electric conduction. A process known as doping consists of adding to the crystal, atoms from materials (impurity) with more or fewer electrons in their valence band than that of the crystal itself. In a case where the impurity has a surplus of valence electrons, the excess electrons jump to the conduction band without leaving holes behind. This type of semiconductor is called n-type. When the number of valence electrons is less in the impurity than in the crystal, conduction electrons will fill the holes created in the valence band by the deficiency in electrons. The semiconductor in this case is a p-type.

The change in density of charge carriers from one end to the other end of the crystal is called a p-n junction. There is a diffusion of electrons and holes to the side where they are less abundant. This results at equilibrium, in the creation of a region where there is a net formation of electrons on the p side and of holes on the n side of the junction. This region is called depletion region and is characterised by an intrinsic electric field. The depletion region is the active area of semiconductor detectors. The thickness of the depletion region is given by Equation 2.32,

$$d = \left(\frac{2\epsilon V}{eN}\right)^{1/2}, \tag{2.32}$$

where ϵ is the dielectric constant, V is the voltage (reverse bias), N is the concentration in impurity in the semiconductor material, e is the electron charge.

The depletion region is quite thin when not connected to an external source of voltage, that is, when the detector is not biased. A reverse bias is obtained by applying a positive high voltage to the n side of the junction. The depletion region expands gradually to the p side as the bias voltage increases. Depending on the application and the type of detector, the bias voltage can be ramped up until the detector is fully depleted. As the volume of the depletion region increases, the detector becomes more efficient. However, such change in the depletion region volume favours the formation of leakage current in the detector, due to thermally generated electron-holes pairs within the depletion region. The leakage current is typically in the order of a microampere. Although detectors such as sillicon detectors can operate without being affected by the leakage current, germanium detector need to be cooled down when biased.

2.4.1.2 Detection principles of germanium detectors

The most commonly used crystal in semiconductor detectors is the Hyper-Pure Germanium (HPGe) crystal. HPGe detectors are built in a p-i-n like structure consisting of a p-type contact, an intrinsic HPGe crystal and an n-type contact. In some cases, the p-type contact consists of the implantation of a boron layer in a lattice of the germanium crystal and the n-type is obtained from a drift of electrons resulting from the diffusion of lithium into the crystal. They are usually built in two main configurations, planar and coaxial. In a planar configuration, the crystal is typically shaped like a disk. The doping atoms are represented as shown in the example in Figure 2.10a, where lithium is implanted on the surface of the crystal. In the coaxial configuration, the core of the crystal is removed. When the core is completely removed, the crystal is said to be a true coaxial crystal. If on the other hand the core is partially removed (only on one end of the crystal), the crystal is referred to as closed-end coaxial crystal. The HPGe detector can be of type p or n depending on the type of impurity.

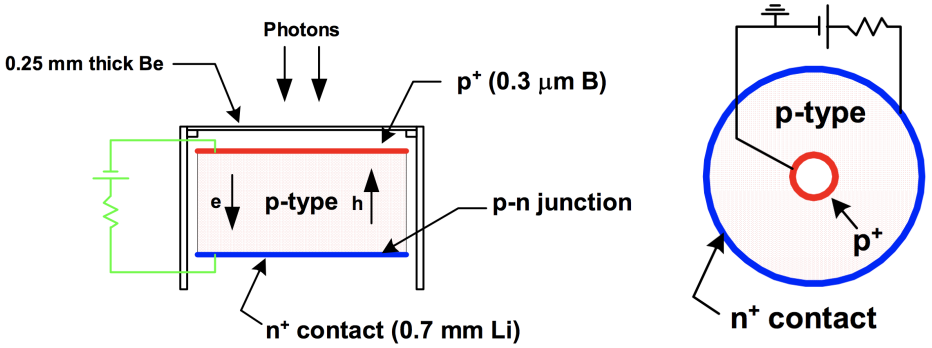

(a) planar configuration

(b) coaxial confugura-tion

Figure 2.10: Schematic representation of two configurations of a p-type High-Pure Germanium detectors [28]

.

The interaction of incident radiations within the detector results in the creation of electrons (or holes) in the depletion region formed in the intrinsic crystal area when the detector is reverse biased. If the incident radiation consists of charged particles like protons and electrons, they will continuously interact with atomic electrons in the detector material, creating electron-hole pairs along their path. When incident radiations are photons or neutrons, their interaction with the detector material results in the creation of secondary charged particles that will in

turn create electron-hole pairs. The presence of an electric field in the depletion region causes created charge carriers to drift apart until they are collected by cathodes at the edges of the depleted volume. The collected signal is then pre-amplified and channelled through adequate electronics for further processing. To avoid leakage current, germanium detectors need to be maintained at a very low temperature when biased. From their construction, they are placed in a cryostat connected to a Dewar filled with liquid nitrogen.

2.4.2 Scintillator detectors

Scintillator detectors are part of the first type of detectors used in radiation detection. Their applications range from charged particles to γ rays and fast neutrons. A scintillator detector is made of a scintillator material, a light guide and a photomultiplier tube.

2.4.2.1 Scintillating materials

Scintillators are materials that fluoresce after an interaction with radiation or charged particles. Fluorescence is the spontaneous emission, by a material, of visible light as a result of an excitation. Scintillators can be organic or inorganic.

Inorganic scintillators can be semiconductor crystals, with sodium iodide being one of the most commonly used in radiation detection. Similarly to germanium crystals, an excitation will cause an electron to jump from the valence band to the conduction band, forming an electron-hole pair. Some impurities are added to the crystal in such a way that some energy levels are created in the forbidden gap. The de-excitation of the electron that previously moved to the conduction band will result in said electron to find itself at one of the newly created energy levels. The photon emitted during this de-excitation carries an energy in the range of visible light. De-excitation sites in the crystal are called luminescence or recombination centres [22].

Organic scintillators can be of different types, pure crystals, liquid organic solutions or plastics. The light output in both organic and inorganic scintillators is

given by Birks' law as follows,

$$\frac{dL}{dr} = \frac{S\frac{dE}{dr}}{1 + k_B\frac{dE}{dr}}. \tag{2.33}$$

The factor S represents the scintillation efficiency, k_B is Birks' constant or quenching parameter. dE/dr is the stopping power and dr the range of the scintillator.
Equation 2.33 only applies for protons, α-particles, ^{3}He, d, t and fast neutrons. For electrons the light output is proportional to the energy deposited:

$$\frac{dL}{dr} = S\frac{dE}{dr}. \tag{2.34}$$

Inorganic scintillators are mostly used for gamma-ray spectroscopy. These have a better light output (50-70%) as compared to organic scintillators. However, organic scintillators have a faster response time with a decay time of 2 to 5 ns as opposed to ∼500 ns for inorganic scintillators [20]. Organic scintillators are used for the detection of charged particles and fast neutrons. They have the advantage of being affordable and easy to shape.

2.4.2.2 Light guide

The light guide serves as a conduit between the scintillator and the photomultiplier tube, in cases where their shapes do not allow a direct connection. Light guides are built from materials such as polyvynil toluene, quartz and perspex (polymethyl methacrylate), and are designed to minimise light losses. Their functioning follows a principle of internal reflection of light propagation. It is often advised to cover the plastic scintillator and the light guide with an aluminium foil to insure an efficient internal light reflection, hence minimising light losses.

2.4.2.3 Photomultiplier tube

The photomultiplier tube (PMT) converts the very weak light output from the scintillator into a corresponding electric signal, and amplifies it to a usable signal. PMTs are divided into two main parts. The first part is a photocathode, where incident photons from the light guide are converted into electrons via the

photoelectric effect. These electrons are then focused and accelerated to strike a dynode. The energy deposited by a single electron on the dynode surface is enough to provoke the re-emission of secondary electrons. Secondary electrons strike a second dynode and more electrons are created, repeating geometrically. This process is repeated several times, depending on the typical gain of the PMT. The final amplified current pulse is sent to an anode and then to appropriate electronics for processing.

An optical grease with the same index of refraction as the scintillator is used to couple the plastic scintillator to the light guide, and the light guide to the PMT. This allows an undistorted flow of light from the scintillator to the PMT.

2.5 Particle acceleration and ion sources

2.5.1 Principle of particle accelerators

Particle acceleration is a process whereby charged particles are accelerated, using an electromagnetic field, to energies higher than 1 MeV typically. The particle beam to be accelerated is provided by a particle source. Two basic types of particle accelerators can be observed: linear accelerators, where particles are propelled along a linear beam line and circular accelerators, where particles are accelerated and directed, using a magnetic field, along a circular beam line. Particle acceleration can occur through non-resonant magnetic induction or through resonant system (or cavities) excited by an oscillating radio frequency (RF) field. Accelerators are built using either one of these mechanisms. Linear induction accelerators and betatrons for instance, operate using magnetic induction. RF fields are used in accelerators such as cyclotrons and synchrotrons. They are circular accelerators. In cyclotrons particles are accelerated by an homogeneous magnetic field generated by an iron magnet [29]. They travel in a circular manner, following repetitively the path with a frequency f_c called cyclotron frequency.

$$f_c = \frac{e}{m}B, \tag{2.35}$$

where B is the magnetic field strength, m is the particle mass and e its charge.

Once ion beams have been accelerated to desirable energy and intensity, they are directed through beam lines to be used for different purposes (experiment and radiation production for example).

2.5.2 Ion sources

Particle sources are one of the most important parts of the accelerator chain. Ion sources are often used for the production of monoenergetic and unidirectional ion beams. Electron sources can also be used, but with a limited variety range [30]. Ion sources consist of two main parts: the ion production region and the ion extraction system. In most cases, the production region is made of plasma. Plasma is gas in which atoms have been ionized. Ionization is achieved by increasing the temperature of a gas (thermal or surface ionization), by applying a strong magnetic field, using a laser or a microwave generator, to a gas (field and laser ionization) or by bombarding a gas with an intense photon beam (photo ionization) [30]. Apart from some unionised neutral atoms, plasma consist of negatively and positively charge particles (positive ions, negative ions and electrons), thus is electrically conductive. Plasma must adhere to certain criteria, with a view to optimize the production of ions of interest while limiting undesirable ions [31]. Such criteria takes into account the density, the temperature and the charge state of the plasma. The basic ion extraction principle consist of applying an electric field between an electrode placed directly in contact with plasma (plasma electrode), and an extraction electrode [32]. Ions converge towards the extraction electrode due to the effect of the electric field. Additional electrodes constituting an electrode system are in charge of the acceleration and focusing of the ion beam. Examples of ion sources are the Penning or Philips Ionizaton Gauge (PIG) ion source, Electron-cyclotron-resonance (ECR) ion source and Metal vapor vacuum arc (MEWA) ion source.

2.6 Summary

Fundamental tools and theories necessary for the measurement of the production cross section of light exotic nuclei using stable nuclei has been presented in this chapter. Details on the interaction of particles with matter were described, as well as the functioning principles of germanium detectors and scintillators. Since

all nuclei of interest undergo β-decay, the description of this process was given, using Enrico Fermi's approach. In Chapter 3, information about the experimental setup and the procedure used for the measurement will be laid out, as well as the overview of the facility.

Chapter 3

Experimental details

3.1 Overview

In view of measuring the production cross section of ^{6,8}He and ^{8,9}Li, measurements were conducted at iThemba LABS, Cape Town, South Africa. Targets of ^{nat}Li, ^{9}Be and ^{nat}B were bombarded with a beam of proton at 50 and 66 MeV. Gamma and electron spectrometers were used for detection. Two 5 mm plastic scintillator detectors were designed and built. They were then combined with two LEPS (Low-Energy Photon Spectrometer) detectors in a ΔE-E manner to form two electron telescopes. The plastic scintillator detector measured the energy loss ΔE while the LEPS was in charge of measuring the residual energy E_r. The total energy of the β particles emitted by the products being the sum of both, $E=E_r+\Delta E$. The ΔE-E technique obtained from this combination of detectors allowed particle identification and high resolution measurement simultaneously. In this chapter, the experimental set-up used for the measurement will be presented, with details on the detectors, electronics and data acquisition system, as well as the experimental procedure. An overview of the facility will also be presented.

3.2 Brief overview of the facility

iThemba Laboratory for Accelerator Based Sciences (iThemba LABS) is the largest accelerator based sciences and technologies research facility in sub-Saharan

Africa. Its area of expertises ranges from radiological research to radionuclide production and research. Research at iThemba LABS is mostly oriented towards nuclear and applied physics, radiation biophysics and materials research. iThemba LABS operates a Separated Sector Cyclotron (SSC) with a K-value of 200, producing beams of various ionic species. The K=200 SSC is capable of accelerating protons to a maximum energy of 200 MeV. It has been operational for more than three decades [33] and is the largest cyclotron in Africa. The SSC is fed by either one of the two Solid-Pole injector Cyclotrons, SPC1 and SPC2 as shown in Figure 3.1. The K8 Solid-Pole injector Cyclotron (SPC1), also known as the light-ion Solid-Pole injector Cyclotron, is equipped with an internal Penning Ionisation Gauge (PIG) ion source. It was designed to pre-accelerate proton beams to a maximum energy of 8 MeV. Pre-accelerated protons are used for both research and radioisotope production. In the latter case, protons are pre-accelerated to an energy of 3.14 MeV and then accelerated by the SSC to 66 MeV.

The Solid Pole Cyclotron with a K-value of 10 (SPC2) is meant for the pre-acceleration of light and heavy ions, as well as polarized protons. It is furnished by three external ion sources: two Electron Cyclotron Resonance (ECR) ion sources and one Polarised proton ion source. The availability of the two ECR sources makes it convenient for beam development and beam delivery. The choice of the injector cyclotron depends on the type of particle to be produced. Once the beam has been pre-accelerated, it is injected to the SSC to be accelerated to the desired energy and further delivered to different facilities through beam lines.

The main experimental facilities used in subatomic physics research at iThemba LABS are the electron spectrometer, the A-line for various subatomic physics experiments, the HPGe detectors array AFRODITE, the full $LaBr_3$:Ce array ALBA, GAMKA made of a combination of HPGe and $LaBr_3$ detectors, and the K600 magnetic spectrometer (along the S-line).

Measurements in regards to this study were performed in the S-line vault. This facility was targeted because of its availability at the moment of the experiment. It is convenient and flexible in the sense that the scattering chamber can be disconnected from the magnetic spectrometer and connected directly to the beam

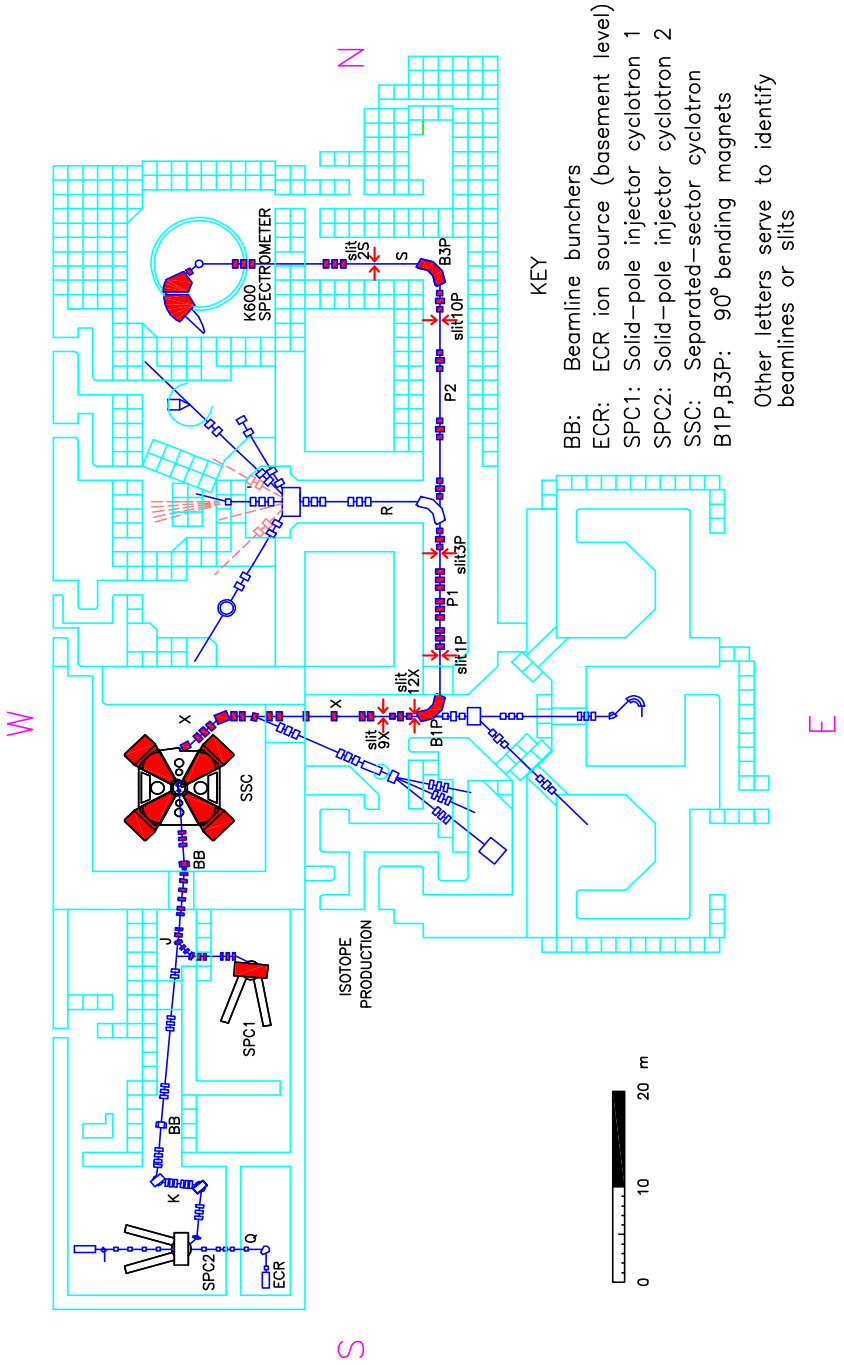

Figure 3.1: Layout of the accelerator facility at iThemba LABS [34].

pipe leading to the beam dump. Moreover, this facility was built with a support structure allowing the location of detectors at custom positions with safe attachment; therefore making it easy to mount two detector telescopes.

3.3 The proton beam

The proton beam used in this experiment was pre-accelerated by SPC1 before being sent through the J line to the SSC, where it was accelerated to 50 and 66 MeV. It was then steered through to the S-line for use. The beam was turned on and off using a beam chopper, during cycles of two and five seconds, depending on the target. The beam-on sequence was set long enough to reach secular equilibrium of the products, and the beam-off time was set to allow nuclei with the longest half-life to decay. The interest in using a proton beam lies in the fact that protons have a relatively high penetrating power as compared to heavy ions and are available with high intensities.

3.4 Target chamber

Also known as the scattering chamber, the target chamber is a vessel in which the reaction takes place. It is located between the end of the S beamline and the pipe leading to the beam stop. It is mostly evacuated and allows beam transport. Targets are placed on a target ladder in the target chamber. The target ladder accommodates six frames occupied from top to bottom by the natural boron target, the beryllium target, the lithium target, a kapton film, the viewer and an empty frame, as shown in figure 3.2.

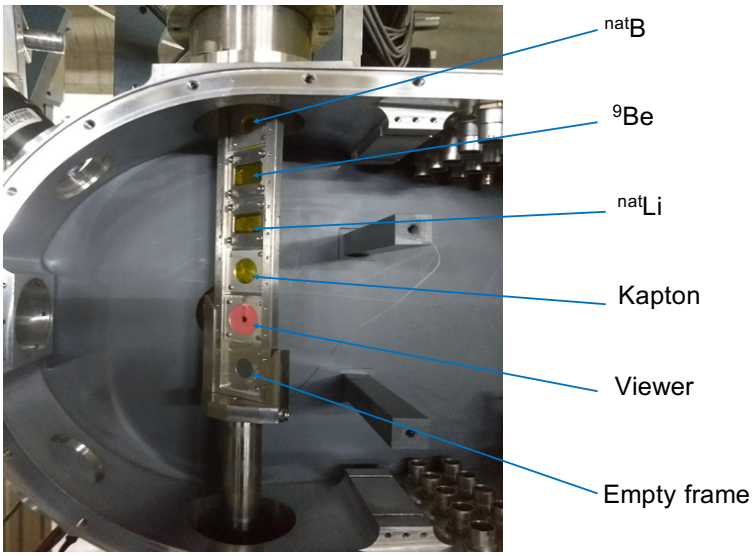

Figure 3.2: The target ladder is occupied from top to bottom by the ^{nat}B, ^{9}Be, ^{nat}Li, a kapton film, the viewer and the empty frame.

The viewer is used to check the beam alignment and the empty frame is for the in-beam background measurement. Detectors are placed facing the sides of the chamber as shown on the experimental set-up in Figure 3.3. The sides are made of polyvinyl chloride (PVC) plates with a window covered by a kapton film. They are tilted to form a 7° angle with the beam axis.

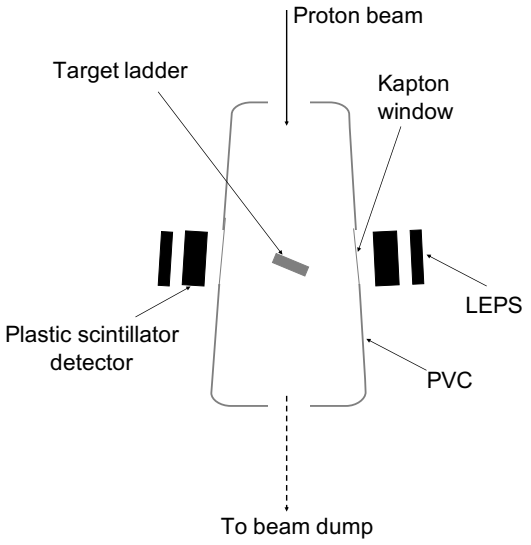

Figure 3.3: Sketch of the experimental set-up with the detectors positioned on each sides of the scattering chamber.

3.5 Targets

As mentioned above, the targets are placed on a target ladder, in the target chamber. The target ladder is mounted in such a way that it can be moved up or down to position the desired target frame in the beam axis without breaking vacuum. The target ladder can also be rotated around its vertical axis, perpendicular to the beam axis. Targets were positioned at an angle of 45° during the experiment. Dimensions of the targets are given in Table 3.1

Table 3.1: Targets characteristics

Targets	Thickness [cm]	Areal density [g/cm^2]	Isotopic composition
^{nat}Li	0.290	0.154	7.6% ^{6}Li, 92.4% ^{7}Li
^{9}Be	0.0154	0.028	100% ^{9}Be
^{nat}B	0.149	0.035	19.8% ^{10}B, 80.2% ^{11}B

In order to obtain the ^{nat}Li target, ^{nat}Li was pressed in a target frame and sealed with kapton films; and therefore taking the shape of the frame. The ^{9}Be target consisted of six layers of 25.7 μm beryllium foils. The ^{nat}B target was fabricated by pressing amorphous boron powder in order to obtain a disc of 9 mm diameter.

3.6 Detectors set-up

Two detection telescopes, each consisting of a LEPS and a plastic scintillator detector, were mounted as shown in Figure 3.4. They were then positioned parallel to the sides of the target chamber, tilted to a 7° angle relative to the beam direction.

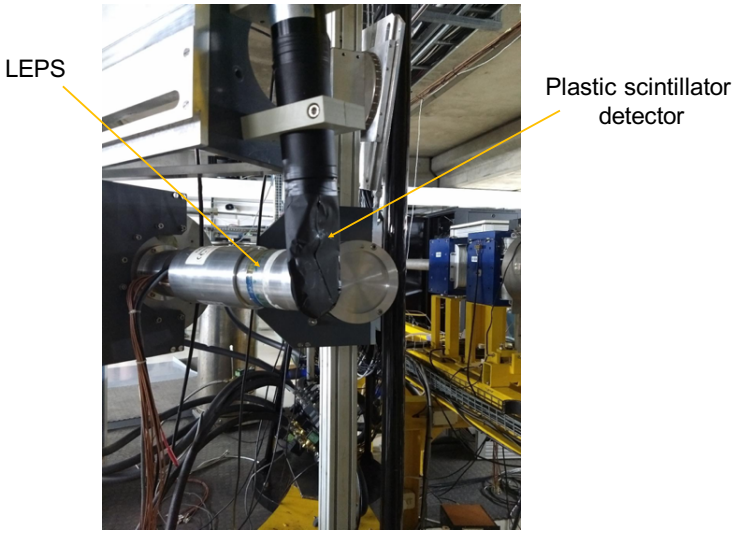

Figure 3.4: Detectors mounted at the S-line.

3.6.1 LEPS

The Low-Energy Photon Spectrometer (LEPS) is a small-area segmented planar HPGe detector. The two LEPS' used for this experiment were manufactured by EURISYS, France. LEPS detectors are made of a p-type HPGe crystal, electrically segmented into four quadrants. They have an active area of 2800 mm^2, an external diameter of 66 mm and 11 mm thickness. The entrance window of a LEPS is made of a 300 μm beryllium sheet [35], protected by an end cap of 80 mm diameter. They have a good energy resolution. For instance the energy resolution at 1300 keV is about 1.7 keV. LEPS detectors are equipped with one internal preamplifier per segment. The first stage of the preamplifier consists of a Field-Effect Transistor (FET) accompanied by an RC feedback, with a decay time of 1 ms. The second stage, more sophisticated, has a decay time of $\sim$50 μs.

3.6.2 Plastic scintillator detectors

3.6.2.1 Plastic scintillator detector assembling

The two plastic scintillator detectors used for this work were mounted and tested. Since these detectors were used in a ΔE-E measuring technique for energy loss measurement, they were cut and shaped to cover the entire surface area of the

LEPS (to be precise, dimensions were taken referring to the end cap diameter). In this respect, the plastic scintillator was cut as shown in Figure 3.5. NE102 was used as scintillating material. The light guide was shaped as in Figure 3.5, with a back side of 50 mm diameter to fit the entrance window of the photomultipier tube (PMT). PMTs used were manufactured by HAMAMATSU, Japan. The three parts were coupled together using a silicon grease. The choice of silicon grease for this task resided in the fact that silicon is thermally resistant, with the same refractive index as the light guide, and as such opposes no resistance to the light flow. The mounted plastic scintillator detectors will be referred to as "paddles" from this point forward. The scintillator and the light guide were then covered with a layer of aluminium foil paper to redirect the light in the light guide, and a layer of black cardboard paper to block the incidence of external photons on the PMT.

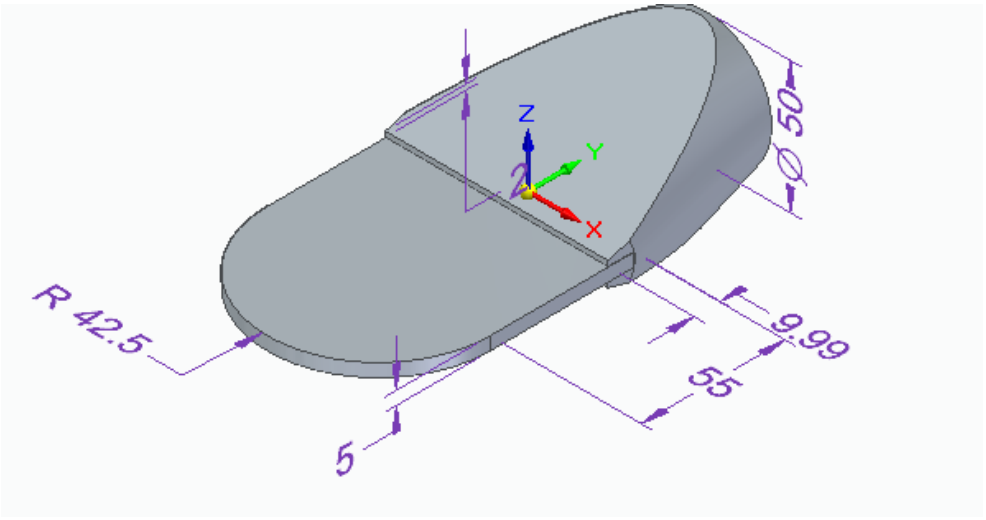

Figure 3.5: Design of the plastic scintillator and the light guide. See labels below.

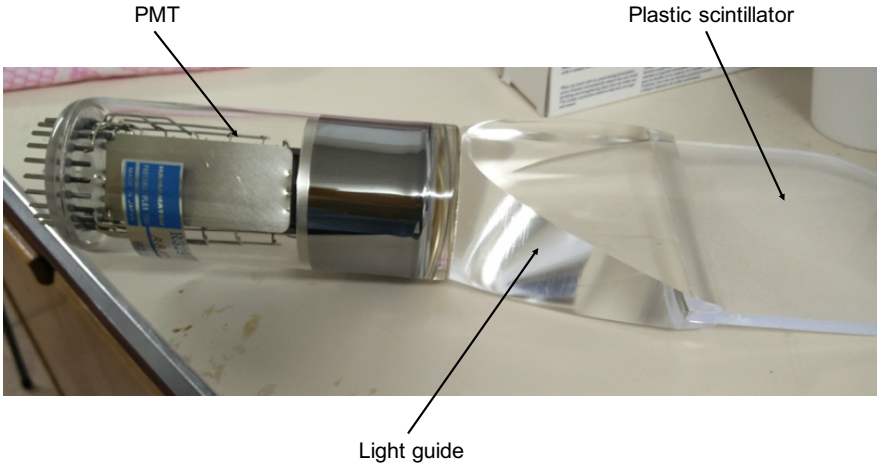

Figure 3.6: Plastic scintillator and light guide were polished and mounted to the PMT.

3.6.2.2 Testing the Paddle

Tests were conducted to evaluate the charged particle detection capability of a paddle. This was achieved by using them to measure muons. Muons are the most penetrating cosmic rays. They are one of the secondary comic rays, together with other muonic, hadronic and electromagnetic particles, that result from a reaction between primary comic rays and atmospheric components. Primary cosmic rays consist mostly of protons. Muons are the product of the decay of pions and kaons:

$$\pi^+ \rightarrow \mu^+ + \nu_\mu,\ \pi^- \rightarrow \mu^- + \bar{\nu}_\mu \text{ and}$$
$$K^+ \rightarrow \mu^+ + \nu_\mu,\ K^- \rightarrow \mu^- + \bar{\nu}_\mu.$$

They primarily decay into electrons and positrons:

$$\mu^+ \rightarrow e^+ + \nu_e + \bar{\nu}_\mu \text{ and } \mu^- \rightarrow e^- + \bar{\nu}_e + \nu_\mu.$$

Muons are highly energetic; they are minimum ionizing particles and their energy loss is approximated to 2 MeV/g/cm^2. The maximum energy detected for muons at sea level is 4 GeV. At low energies, they lose energy mostly by ionization and the energy loss can be calculated using the Bethe-Bloch formula. For high energy muons, on the other hand, the energy loss is mostly by bremsstrahlung,

pair production and photo-nuclear interactions (these processes constitute the radiative loss). The mean stopping power for muons at high energy in a given material is expressed in Equation 3.1,

$$\frac{dE}{dx} = a(E) + b(E)E \tag{3.1}$$

where $a(E)$ represents the ionization or electronic loss, $b(E)$ the radiative loss and E the total energy.

The energy loss of muons in a plastic scintillator material was calculated using known stopping powers [36], for incident energies up to 10 GeV, as represented by Figure 3.7. It is observed that at 4 GeV, muons lose approximately 1.2 MeV when going through the paddle. The energy loss of muons of multi GeV incident energy is comparable to the energy loss of electrons with a couple of MeV. Testing the detectors using cosmic muons helps to anticipate what happens with the electrons of interest in this measurement.

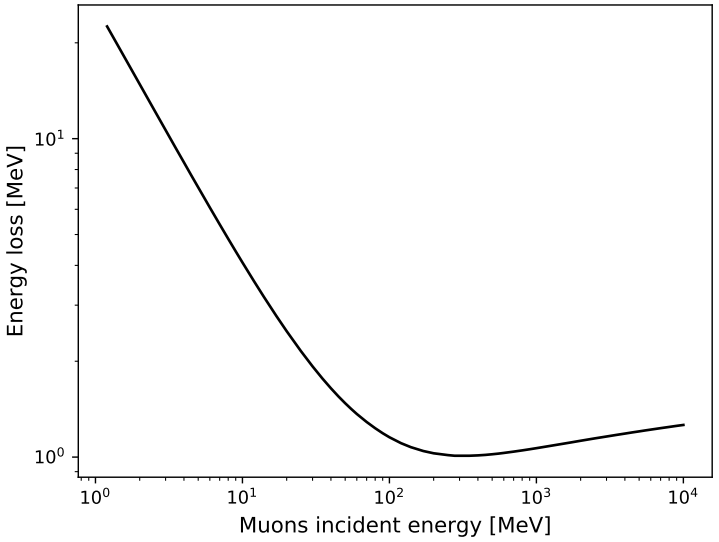

Figure 3.7: Energy loss of muons in plastic scintaillator.

To test the two paddles, they were put together with six large plastic scintillator detectors of 10 cm thickness each, present in the lab, in order to observe coincidences. The six large detectors consist of three $600\times100\times100$ mm^3 plastic scintillator of type NE102, each with two PMTs, one on either side. All PMTs were supplied with a 1500 V negative high voltage. Detectors were stacked vertically as shown in Figure 3.8.

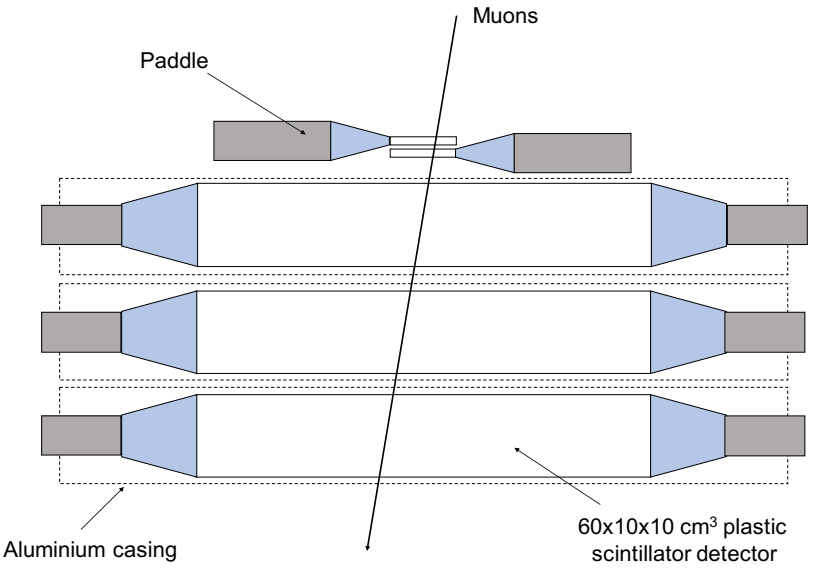

Figure 3.8: Plastic scintillator assembly for detection of muons. Three large plastic scintillators are each connected to two PMTs, making a total of six 600×100×100 mm^3 plastic scintillator detectors.

Coincidence measurements were conducted between paddles and other detectors. Figure 3.9 shows the output of one of the paddles in coincidence with two of the 600×100×100 mm^3 detectors. The selection of events was based on energy deposited within the 600×100×100 mm^3 detector, consistent with muon energy deposition. Since muons were the only high energy charged particles present in the lab in the absence of any radiative source, it was concluded that the peak on the histogram represents the energy deposited by muons. This experiment confirmed that paddles could be used to detect charged particles.

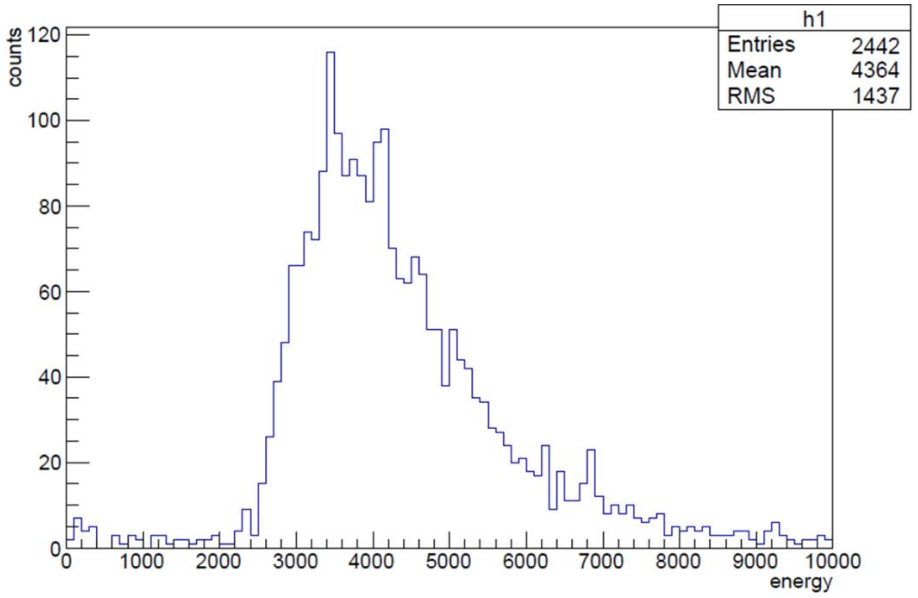

Figure 3.9: Output of a paddle in coincidence with two 10 cm plastic scintillator detectors. The abscissa represents the energy in channel numbers and the ordinate represents the number of counts per energy division.

3.7 Electronics and data acquisition system (DAQ)

A high voltage supply is used to bias the LEPS (+1500 V) and supply the paddles PMTs (-1000 V). The signal produced by the detectors is required to go through several levels of processing before being collected and analysed.

3.7.1 Amplifiers

Signals produced by detectors are in most cases of low amplitude. Preamplifiers and amplifiers are therefore required for signal conditioning. Some detectors like LEPS are equipped with internal preamplifiers, and can have their outputs connected directly to the digital data acquisition system without being submitted to an amplification. Plastic scintillator detectors however need to be connected to either an external preamplifier or an amplifier, or both for the signal to have suitable characteristics. The signal from the paddle was connected to a Timing

Filter Amplifier (TFA) from ORTEC, model 474. The role of the TFA in this case is to perform a linear amplification on the small amplitude range produced by the paddle. It is also used for signal shaping controlled by selected differentiation and integration time constants set to regulate the rise and decay time. Another function of the TFA is to invert the signal polarity (paddles generate a pulse of negative polarity).

3.7.2 Pulse generator

The pulse generator or pulser generates pulses characterised by a fast rise time and an exponentially slow decay time. When collecting data during a beam-off sequence, a gradual decrease in count rate can be observed. After a number of decays, the signal becomes weak and can no longer be coded by the DAQ. As a result, a pulser was used to keep a constant minimum count rate in the system at all time. The pulser can also be used for synchronisation when more than one DAQ modules are used simultaneously.

3.7.3 Current integrator

The Faraday cup is an electrically isolated cup introduced along the path of the beam, which primary function is to measure the beam current. It is located after the scattering chamber and completely evacuated. Projectiles constituting the beam transfer their charge to the cup, generating a flow of electrons collected by a high precision current meter (current integrator). The obtained beam current is used to determine the number of particles hitting the cup per unit time. The functioning principle of the Faraday cup detection system is described in Figure 3.10. The current (flow of electrons generated by the Faraday cup) is amplified and converted via the current-voltage converter, producing the voltage U to be measured. The following expression can be written

$$U = R_L \cdot I_{beam}, \tag{3.2}$$

where I_{beam} is the beam current and R_L a reference resistor.

The measured beam current is monitored by the current integrator, where it is digitised and pulses are generated. A range is set depending on the charge to be

measured, in order to produce a pulse rate of 1000 Hz. The number N_p of beam particles hitting the cup for a time t is deduced from the beam current as follow:

$$N_p = \frac{I_{beam} \cdot t}{ze}, \tag{3.3}$$

where ze is the charge of beam particles.

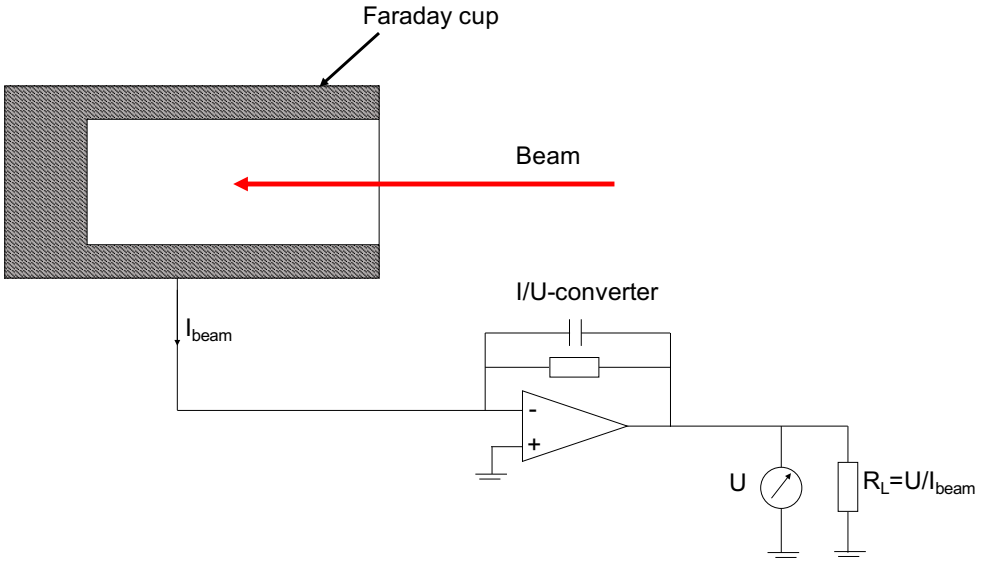

Figure 3.10: Faraday cup functioning principle.

3.7.4 Data acquisition system

The iThemba LABS Digital Data Acquisition System [37] was used in acquiring data necessary for the cross section measurement. The DAQ system is equipped with Pixie-16 acquisition modules, from XIA, USA [38]. It constantly samples the input signal (100 / 250 MHz) and subsequently converts the analogue signal from the detector into a digital signal and coding it in order to obtain digital information including amplitude, time information, channel number, pulse shape and more. The Pixie-16 is a module with 16 input channels, each equipped with a Flash Analogue to Digital Converter (ADC) unit. It is hosted in a Compact PCI/PXI crate which can accommodate 7 or 11 modules depending on its power capacity. Pixie-16 are high performance and flexible DAQs, with broad computing power. The DAQ encodes energy values from raw signals and records the values within events that are considered of interest (triggered) or time stamped to be further considered interesting, or not, depending on the time gates. Once in

the ADC unit of each Pixie-16 channel, the signal is filtered, adjusted for offsets and digitized. The digital signal is then sent to the field programmable gate array (FPGA) for processing. The signal flow for input channels to the PCI (Peripheral Component Interconnect) and API (Application Programming Interface) interfaces, as well as event building, is insured by the Digital Signal Processor (DSP). It also insures the overall control unit of the Pixie-16. The Multi Instance Data Acquisition System (MIDAS) software developed in Daresbury Laboratory, UK [39] was used to run Pixie-16.

The current integrator was connected to a separated acquisition system called Pixie-4 [40]. Pixie-4 is a four channel digital pulse processor mounted on a CompactPCI/PXI Express processor, with data reading out to a computer, where it is ran by the software IGOR Pro [41].

The data acquisition process is schematically represented in Figure 3.11.

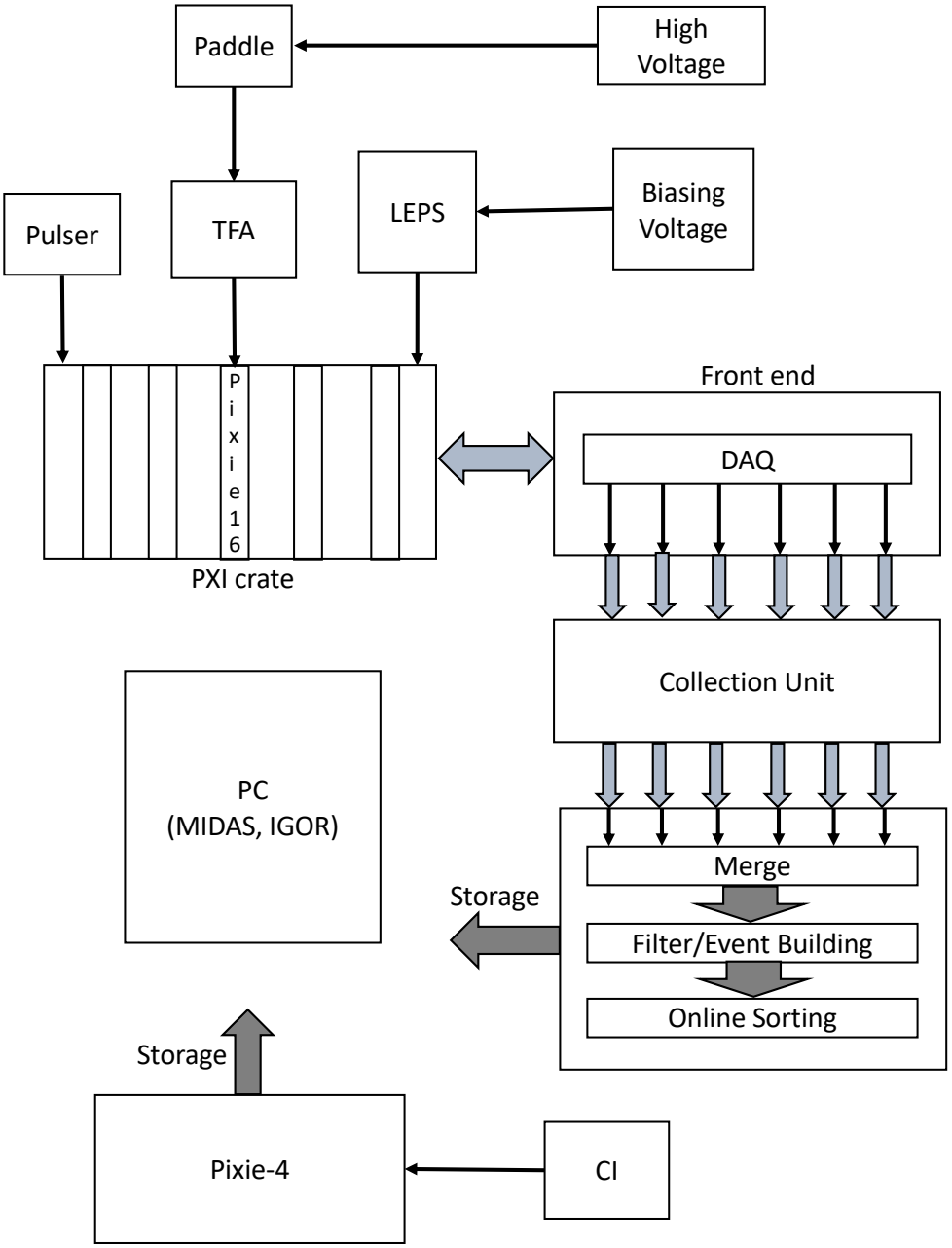

Figure 3.11: Schematic representation of the data acquisition process. The front panel consists of 16 input channels equipped each with an ADC unit. The Pixie-4 operating mode is rather similar to that of the Pixie-16 with difference that the latter has four input channels.

3.8 Experimental procedure

The first series of data were collected for a proton beam of 50 MeV, and a second set at 66 MeV. The data acquisition procedure was the same in both cases. With detectors mounted as shown in Figure 3.3, targets were placed on the target ladder and in the target chamber. The target chamber was then evacuated to a pressure of 2.37×10^{-5}Pa. A viewer was used to position the beam in such a way that it hits the target directly at the center. For measurements with a specific target, the target ladder was moved to the corresponding position. In order to have a larger interaction area, targets were positioned to form an angle of 45° with the beam axis. The target positioning and the beam chopper were monitored from the data room. Beam on-off sequences were set depending on the target in place. Data files were collected during 30 min for ^{nat}Li and ^{9}Be targets, and up to 2 hours for the ^{nat}B target.

3.9 Summary

The main objective in this chapter was to give an insight on the experimental set-up used to conduct the measurements. Details have been presented on the functioning principle of various electronics involved in the data acquisition, as well as the data acquisition system used at iThemba LABS. The detection system has also been laid out. Some informations were also presented regarding the facility where the measurements were performed. The next chapter will focus on the data analysis.

Chapter 4

Data analysis

4.1 Overview

The iThemba LABS Digital Data Acquisition System [37] was used to collect and store data. The list-mode data was then subsequently analysed through SimSort [42]. Histograms generated by the software informed on the number of events detected with respect to ADC channel numbers. In order to identify isotopes produced in the reaction, a conversion of these channel numbers into energies was required. A linear relationship was hence established between the two. The energy loss was also evaluated and it was observed that the total energy of β-particles followed a linear distribution with respect to the energy of β-particles detected by the LEPS. Observing events that occurred during the beam-off sequence, provided information on the decay of products. The product identification was performed by generating the Fermi-Kurie plot, used to observe the endpoint (β decay Q-value) of the reaction. The Fermi-Kurie plot was also used to determine the number of β-particles emitted in the decay, corresponding to the decay rate of products, necessary for the cross section extraction. It was obtained by taking into account the energy loss of electrons in every layer before being absorbed by the active part of the LEPS detector.

Details about the energy calibration and the energy loss calculation will be presented in this chapter. For each target, γ-ray energy spectra and electron spectra of the products will be presented and interpreted.

4.2 Data sorting procedure

4.2.1 Sorting code

The data analysis was conducted using a sorting code called SimSort. SimSort stands for Simulation and Sorting code. It is a software package written in C++, under the ROOT framework developed at CERN [43] and is used to generate energy loss tables. SimSort can be used to conduct simulation and analysis in charge particles, gamma and neutron spectroscopy. It is used to generate ROOT files containing parameters needed for the calculation of physical quantities, provided that adequate information have been entered in input files by the user. This information is relative to the type of reactions and reaction products, as well as detector characteristics and calibration parameters. When used for simulation purposes, SimSort reads through input files, generates events and writes them into binary files. In the case of a data analysis, SimSort reads raw data written in binary files event by event and selects those that correspond to the conditions listed in input files. Undesirable events are discarded and good ones are saved in ROOT files for further analysis. In the course of this work, SimSort was used as a sorting code.

Some of the input files in SimSort are *lookup.cal*, *gain.cal*, *offset.cal*, *position.cal* and *thickness.cal* (see Appendix B). These files inform on the position and geometry of the detectors. Lookup tables are defined in *lookup.cal* files, in which detector outputs are assigned to ADC channel numbers. The gain and offset are defined in the *gain.cal* and *offset.cal* files respectively, and the position and thickness of the detectors are entered in *position.cal* and *thickness.cal* files. Events corresponding to primary information such as the time, the energy, the energy loss needed in the calculation of physical variables such as the cross section are extracted and saved in defined trees using the *SimSort.cxx* file. Some additional files with the .sims extension are created where tasks to be conducted are defined, namely simulation, reaction, analysis, energy loss and such. The number of blocks to be compiled, the type of reaction and the time stamp are set depending on particles of interest (charge particle, photons and neutrons).

4.2.2 Procedure

Once information on the detector geometry, the ADC channel number assignment and the calibration parameters have been entered, the next step is to select the adequate data set depending on the beam characteristics. Events collected during the beam-on sequence inform on the products of the reaction between each target and the proton beam. Those obtained during the beam-off sequence give details on the decay of some of these products. Beam on-off cycles were set from 2 s to 10 s depending on the target. Figure 4.1a shows a fraction of the time spectrum obtained in the p+^{9}Be reaction. This shows a fraction of the time spectra directly from raw files. In this case, the beam is turned on for 4.8 s and off for 5.2 s.

By adding together events corresponding to each beam on-off sequence, Figure 4.1b is obtained. The beam-on is characterised by a high number of events corresponding to prompt γ rays, neutrons, charged particles from induced nuclear reactions including scattered protons, as well as electrons from β-decays. During beam-off, only electrons and γ rays from β-decays are observed, resulting into a lower number of counts.

Photon energy spectra are generated by observing the output of the LEPS in anti-coincidence with the paddles. For electron energy spectra, events considered are those observed with detectors in coincidence. Meaning that, only particles that deposited some energy in the paddle and were detected by the LEPS are considered. A logigram of the data analysis procedure is presented in Figure 4.2.

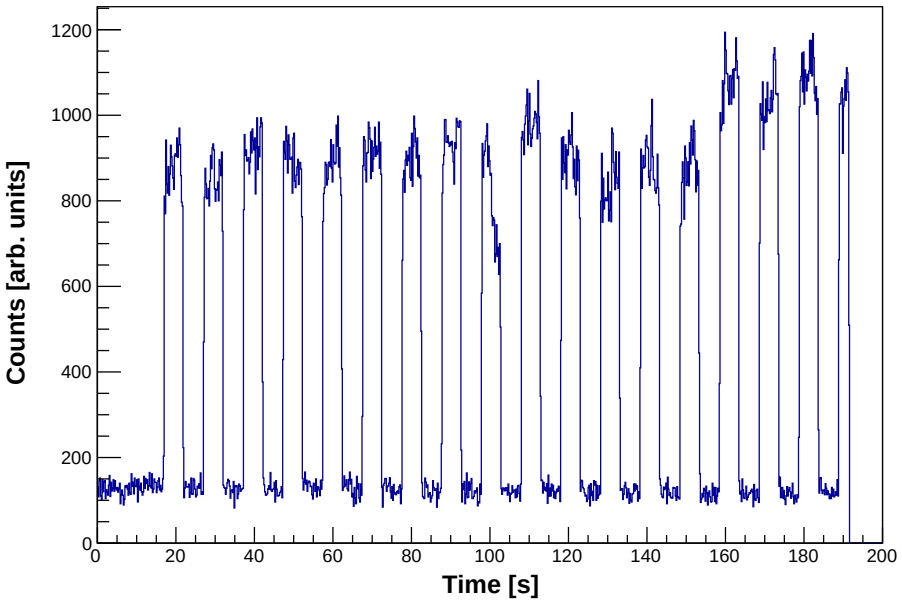

(a)

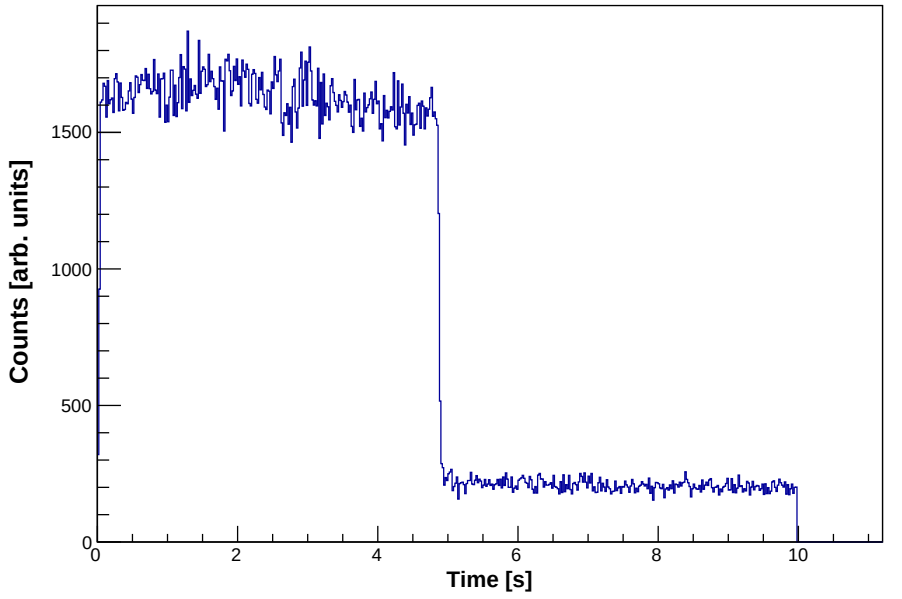

(b)

Figure 4.1: Example of the beam on-off cycles corresponding to a ^{9}Be target with a beam-on sequence of 4.8 s and a beam-off sequence of 5.2 s. **(a)** represents the time spectra obtained from raw data and **(b)** the time spectra with the summing of events produced during the same beam sequences. The beam-on sequence is characterised by a larger number of events, given that only a few particles produced in the primary reaction undergo a decay process when the beam is turned off.

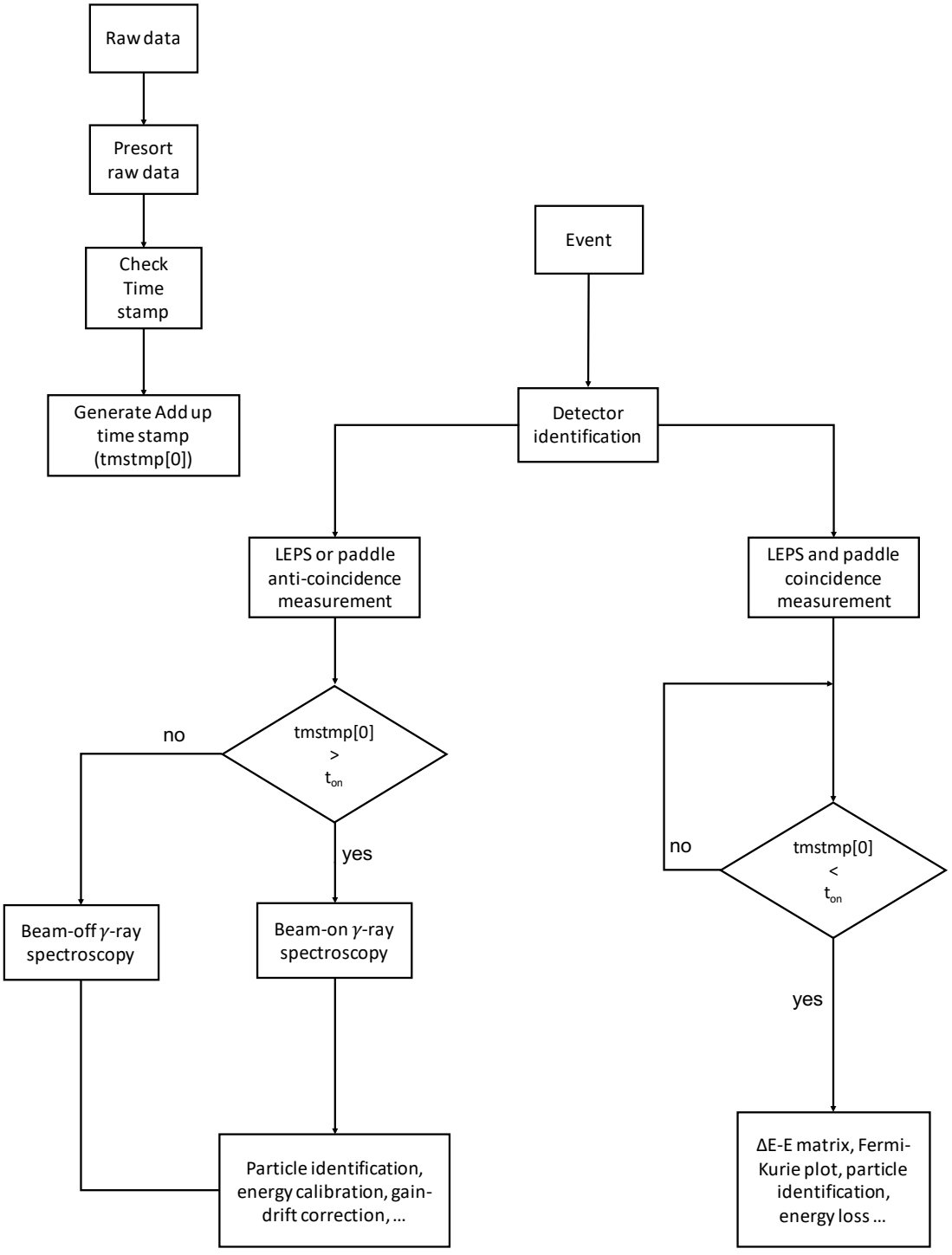

Figure 4.2: Diagram describing the analysis logic. The presorting step consists of running the raw data using SimSort with the gain at unity and a null offset (no modification is done to the data). The selection of events depends on the event time stamp, determining the time at which the event took place and hence the adequate beam on-off sequence.

4.3 Energy calibration

As previously mentioned, the energy calibration consists of assigning energy values to ADC channel numbers. Photon energy spectra are characterised by distinct peaks, facilitating the energy assignment. In this study, electron energy spectra follow a Bethe-Bloch distribution when measuring the energy loss, or the Fermi-Kurie distribution when studying the decay. The effect of the energy calibration of a specific detector, performed using γ rays will be to ensure the positioning of the endpoint of the Fermi-Kurie plot at the expected energy.

4.3.1 Energy calibration of LEPS

The chi-squared (χ^2) minimisation method is used to obtain the line of best fit in the form of a first degree polynomial equation. The best fit corresponds to a minimum possible χ^2 value. Ideally, $(\chi^2/ndf)\approx 1$, with ndf denoting the number of degree of freedom. Coefficients of the polynomial equation generated by the fit represent the calibration parameters and are used to correct the gain and offset of the amplifier. An equation of the form $E = a\times Ch + b$ is established, where a and b represent the gain and offset respectively, Ch the ADC channel number and E the corresponding energy.

Since LEPS' are mostly used in low energy γ-ray spectroscopy, the energy calibration was performed using a ^{152}Eu source. This source emits photons with energies up to 1408 keV. An example of a linear calibration curve obtained by observing the pulse height in channel numbers for one detector's output channel is shown in Figure 4.3, where the gain and offset are deduced. This is achieved by matching each energy peak to its corresponding energy. A set of calibration parameters for each LEPS is listed in Table 4.1, where C_1, C_2, C_3 and C_4 represent the four output channels of each detector.

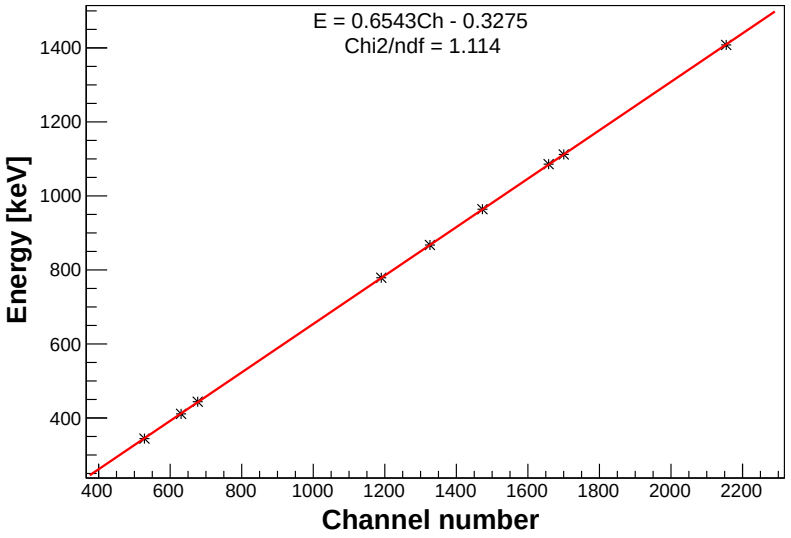

Figure 4.3: Calibration curve for one channel of an individual LEPS detector using ^{152}Eu.

Table 4.1: Set of parameters from the LEPS detector calibration using a ^{152}Eu source. One of the output channels of LEPS number 2 presented some defects and is not included in the analysis.

LEPS	Detector segment output	a [keV/channel]	b[keV]
1	C_1	0.8006	-1.0810
	C_2	0.6977	-1.3105
	C_3	0.6640	-0.2926
	C_4	0.6892	-0.5088
2	C_1	0.8136	-1.0219
	C_2	0.6546	-1.9302
	C_3	0.8305	0.4081

In this study, LEPS detectors were used to measure β-particle energies reaching 16 MeV. In addition to that, the γ-ray energy spectra of all nuclei populated in the nuclear reactions revealed some transitions at high energy, for channel numbers between 5000 and 6000. When correcting for the gain and offset using parameters obtained from the calibration of LEPS with the ^{152}Eu source, it was observed that, by overlaying γ-ray energy spectra from all the detector's segment outputs, the centroid of the peaks at high energy were not aligned. This resulted from the fact that the ^{152}Eu source only guaranteed a good calibration at low energies

and could not be extrapolated to high energies. It was therefore necessary to perform a calibration at high energy.

Considering that LEPS are suitable for low energy γ-ray spectroscopy, the detection of high energy photons has a low probability. In fact, due to their thickness, they are unlikely to detect high energy photons; if the latter Compton scatters, the probability of escape of the secondary photon is very high. Hence it was important to investigate the maximum energy detectable by LEPS detectors. Furthermore, an additional issue was raised regarding the linearity of the calibration curve at high energy. In an attempt to address these issues, one of the detectors was used to measure high energy photons emitted by an americium-beryllium-iron (AmBeFe) source.

4.3.1.1 High energy calibration

An AmBeFe source emits photons with energies higher than 9 MeV. It is made of an α emitter (^{241}Am, with a half life of 432.2 years), coupled with a low atomic number material, ^{9}Be in this case. The resulting americium-beryllium source is fundamentally one of the most commonly used neutron sources in radiation detection. The interaction of α-particles from ^{241}Am and ^{9}Be produces neutrons and ^{12}C with a 4438 keV γ ray (^{9}Be(α, n)^{12}C).
When an americium-beryllium source is placed in close contact with iron, the interaction of neutrons with iron ensures it to be an excellent high energy γ-ray source. Some relevant reactions that happen in the AmBeFe source and their corresponding γ-ray energies are enumerated in Table 4.2.

Table 4.2: AmBeFe source γ-ray energies [44].

Reaction	γ-ray energy [keV]	Reaction	γ-ray energy [keV]
^{56}Fe(n,n)^{56}Fe	846.8	^{54}Fe(n,n)^{54}Fe	6129.3
^{1}H(n,γ)^{2}H	2223.2	^{56}Fe(n,γ)^{57}Fe	7278.8
^{12}C(n,n)^{12}C	4438.9	^{56}Fe(n,γ)^{57}Fe	7631.2
^{56}Fe(n,γ)^{57}Fe	5920.3	^{56}Fe(n,γ)^{57}Fe	7645.6
^{56}Fe(n,γ)^{57}Fe	6018.4	^{54}Fe(n,n)^{54}Fe	9297.8

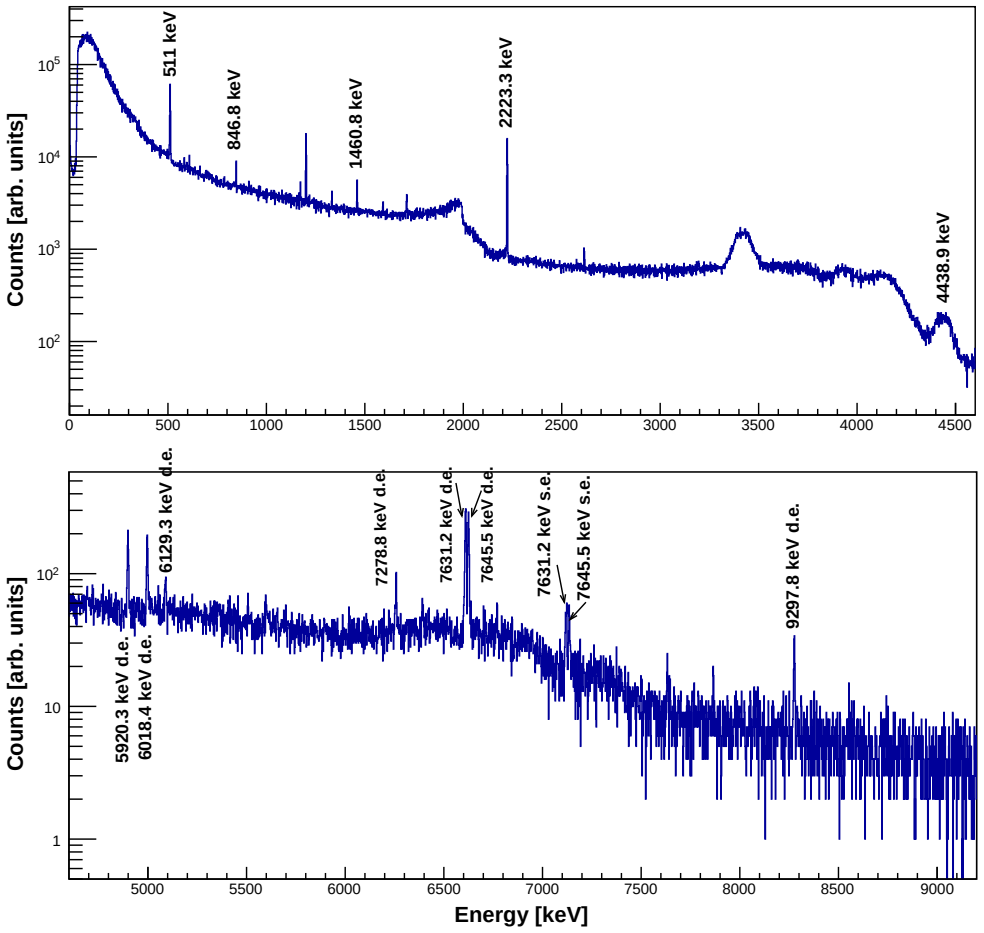

Figure 4.4: AmBeFe source energy spectrum with LEPS detector. The notations s.e. and d.e. stand for single and double escape peak respectively.

In HPGe detectors, as the incident photon energy increases, double and single escape peaks can have a measured intensity higher than that of the full energy photopeak. This can be explained by the fact that the likelywood for photons to interact with the crystal without being fully absorbed is more prominent with increasing energy. Electron-positron pairs that are generated along their path could result in the escape of annihilation photons and the absorption of lower energy γ-rays represented by escape peaks (see Section 2.2.2). With increasing primary photon energy, the number of electron-positron pairs increases and hence the higher the detected intensity of the escape peaks. Consequently, at high energy, a photopeak will probably have its double escape peak with a higher detected intensity than the single escape peak, which in turn will be higher than the photopeak itself. As the energy increases, photopeaks are completely absent

or lost in the background. Following this logic, the response signal of the LEPS to the AmBeFe source was calibrated and energy peaks were identified as shown in Figure 4.4.

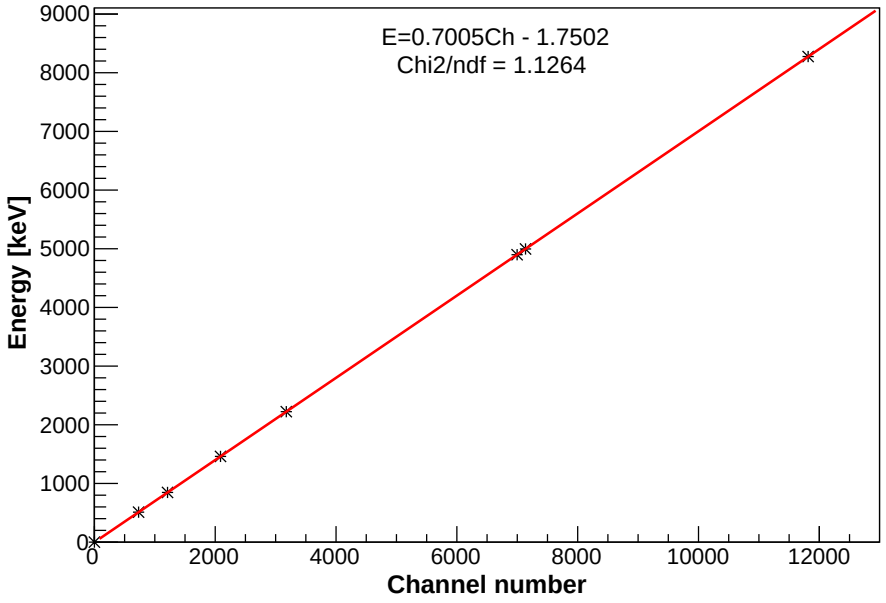

Figure 4.5: AmBeFe calibration curve with one channel of an individual LEPS detector.

It can be observed that LEPS are capable of detecting photons with energies of about 8 MeV, corresponding to the escape peak of a full energy peak lost in background around 9 MeV. The linearity at high energy was also confirmed as shown by the calibration curve in Figure 4.5. This implied that the calibration curve obtained using the ^{152}Eu source could be extrapolated to high energies. As previously mentioned, this procedure results in a non alignment of peak centroids at high energies when overlaying all detector channels of a specific LEPS. The average value of the peak centroids at high energies is compared to known γ-ray energies belonging to any known products of all the reactions at play and catalogued in the ENSDF database. The new identified energy values were then used to correct the calibration and hence the gain and offset. The new calibration parameters are listed in Table 4.3.

Table 4.3: Set of calibration parameters for LEPS detectors corrected for high energy.

LEPS	Output channel	a [keV/bin]	b[keV]
1	C_1	0.7965	2.1979
	C_2	0.6957	0.9011
	C_3	0.6611	2.5033
	C_4	0.6889	-0.1345
2	C_1	0.8122	0.3335
	C_2	0.6554	-2.3664
	C_3	0.8289	1.7306

4.3.1.2 Gain drift correction

When overlaying calibrated signals obtained from different runs, cases are observed where the centroids of some peaks are not aligned. If one of the data files created at the beginning of the measurement is considered as reference, the difference between centroid positions of the peak at high energies are shifted. Such situation is illustrated by Figure 4.6, representing the non-alignment of the peak at 5106 keV, from the p+^{nat}B reaction γ-ray energy spectra. In this case, for a proton beam energy of 50 MeV, one of the LEPS detector output channel is observed in three different runs collected at the beginning, in the middle and one towards the end of the measurement. Such a phenomenon is called gain drift and often comes as a result of temperature fluctuations during the experiment, affecting the electronics; or fluctuations in the beam intensity.

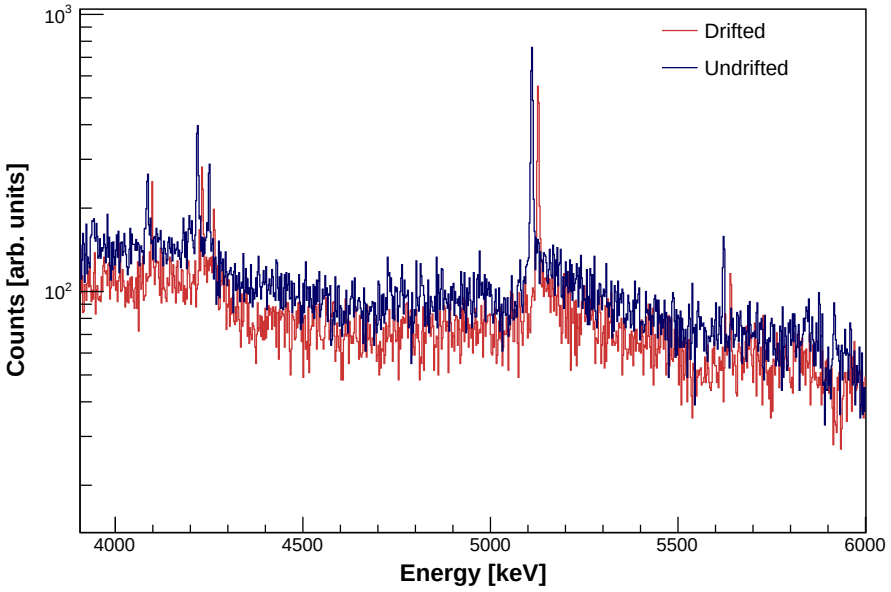

Figure 4.6: Sectioned energy spectra obtained when observing the same detector output channel in two different runs, one at the beginning of the measurement and the other one towards the end. These spectra are generated when using the gain and offset obtained from the calibration of the ^{nat}B γ-ray energy spectrum. Peaks are shifted at high energy.

To correct for the gain drift, two peaks are chosen in the reference run, one at low and one at high energies. These two energy peaks are characterised respectively by the following linear equations:

$$E_1 = a{\cdot}Ch_1 + b \tag{4.1}$$

$$E_2 = a{\cdot}Ch_2 + b, \tag{4.2}$$

where a and b are the gain and offset obtained from the calibration of a specific detector output channel. Ch_1, Ch_2 are the ADC channel numbers allocated to the centroids of the two peaks and E_1 and E_2 their corresponding energies. These same peaks in a different run are characterised respectively by:

$$E_1 = a'{\cdot}Ch'_1 + b' \tag{4.3}$$

$$E_2 = a'{\cdot}Ch'_2 + b'. \tag{4.4}$$

Here, a' and b' are the new gain and offset values, that need to be applied to this run in order to have an alignment of centroids. Ch'_1 and Ch'_2 are the channel numbers. Energies stay unchanged. Channel numbers in both runs, as

well as a and b are known. Therefore by substituting E_1 in Equation 4.3 and E_2 in Equation 4.4 by their respective expressions given by Equation 4.1 and Equation 4.2, a system of two equations with two unknown a' and b' is formed. These new equations are solved to determine values for a' and b' as follow,

$$a' = a \cdot \frac{Ch_2 - Ch_1}{Ch_2' - Ch_1'} \tag{4.5}$$

$$b' = a \cdot \frac{Ch_1 \cdot Ch_2' - Ch_2 \cdot Ch_1'}{Ch_2' - Ch_1'} + b. \tag{4.6}$$

These new parameters are generated for each run and used to correct for gain drifts.

Figure 4.7 further illustrates the centroid shift by representing the difference between a peak centroid in the reference run and the same peak position in other runs. The red line is the reference line corresponding to the run with the best possible calibration. Ideally, all the points should fit on the line. Meaning that all the centroids are supposed to be at the same position regardless of the run.

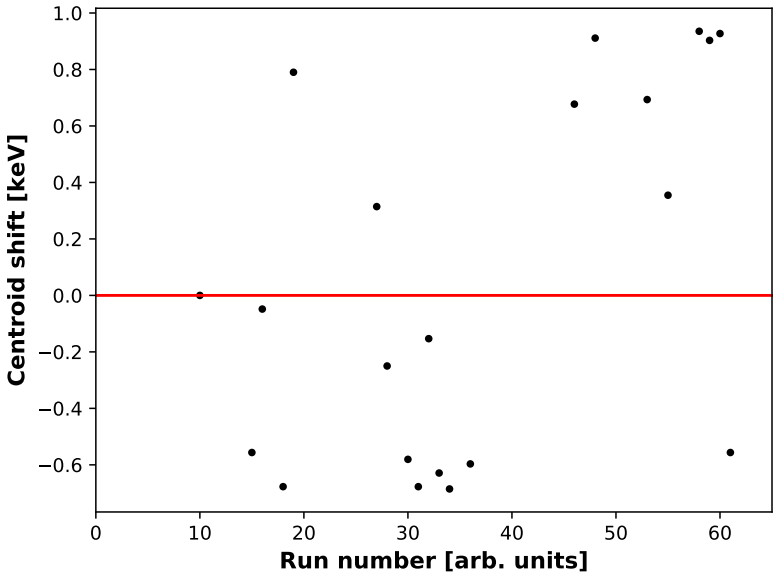

Figure 4.7: Centroid positions of a peak with respect to the reference file. Points are scattered on either sides of the reference line. All the points should be on the reference line after drift correction.

4.3.2 Energy calibration of paddles

Plastic scintillator detectors are mostly used for charged particle detection. They are less efficient and have a poor energy resolution for photons. A photon interacting with a plastic scintillator will most likely Compton scatter and escape the scintillator. The outcome is a spectrum with one or two bumps as illustrated in Figure 4.8. The energy calibration of such spectra is fastidious, especially when photons of different energies are involved.

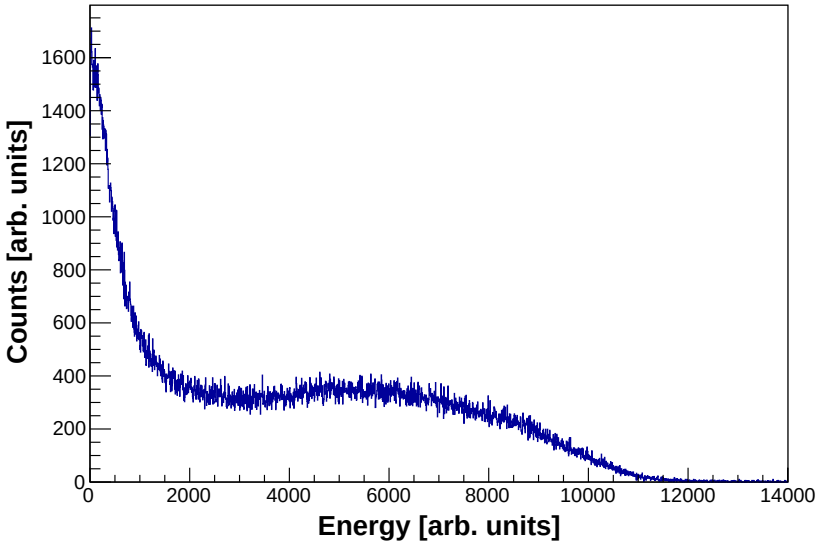

Figure 4.8: Histogram of particles resulting from the p+^{nat}B reaction observed with a paddle in anti-coincidence with the LEPS detector.

The paddle's PMT output is used to plot ΔE-E two dimensional matrices, some of which will be presented in Section 4.7 (see Figure 4.18 for instance). In order to obtain the electron spectrum, one needs to make a cut on the area corresponding to events that happened in both the paddle and the LEPS. A projection of this area on the axis representing the LEPS output, is used to generate the Fermi-Kurie plot. This can be obtained regardless of the paddle being calibrated or not. More details about the ΔE-E matrix will be presented in Section 4.7.

4.4 Residual background analysis

Several phenomena can take place during the experiment resulting in sources of background in the data. Background noise can originate from the electronics used during the experiment, contaminants in the target, contaminants from materials surrounding the target, reaction products that are not of interest in the study and in some cases contaminants from the beam. Regardless of their origins, background noises need to be controlled in order to have accurate results. Meaning that the background needs to be minimized as much as possible during the measurement and later on during the data analysis by developing residual background subtraction techniques.

In this work, in addition to the electronic noise, the major background source is the kapton film surrounding each target. Kapton films are composed of carbon, nitrogen and oxygen. Products of the interaction of these components with the proton beam can emit particles that are observed in both the γ-rays and electron energy spectra. To have an estimation of such background noise, a kapton film was placed in one of the target frames (see Section 3.4) and bombarded by the proton beam. Resulting histograms are presented in the next sections, and compared to energy spectra of reactions taking place in each target.

Histograms are also obtained for electron spectra, when observing LEPS' and paddles in coincidence. Figure 4.9 shows the electron energy spectrum obtained after bombarding the kapton film with the proton beam for 18 min. This spectrum will be parametrised and used to estimate the background when analysing Fermi-Kurie plots. However, since the histogram follows a linear distribution at high energies, the background subtraction on Fermi-Kurie plots can be performed by fitting the background at high energy using a linear equation and extrapolating it to lower energies.

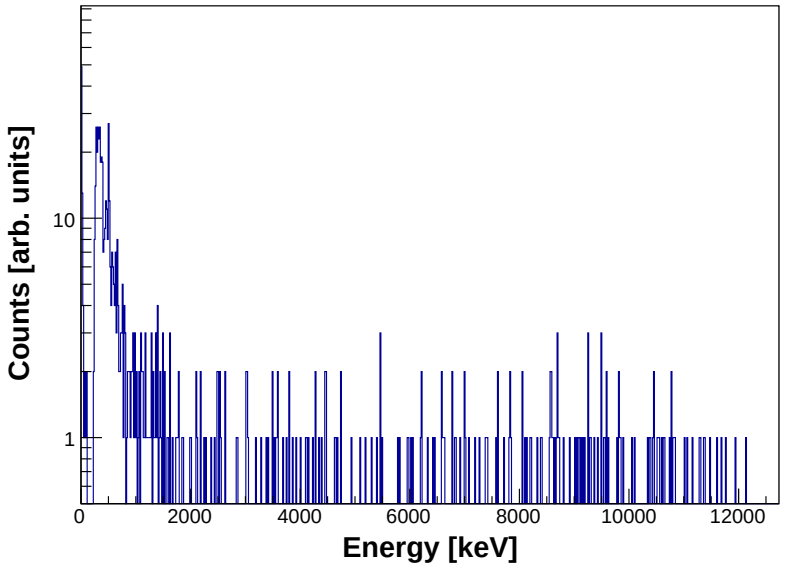

Figure 4.9: Electron energy spectrum resulting from the interaction of the proton beam and the kapton film. It will be considered as background in Fermi-Kurie plots.

In addition to the kapton film, contaminants in targets can also be taken into consideration. For instance lithium targets are prone to some sodium contaminants and can rapidly undergo an oxidation if not well stored. This can however be controlled if the target undergoes very few manipulations and is placed under vacuum as soon as possible. Background from the target frame also have to be taken into account, in which case reactions between the beam and aluminium, which is the major constituent, are considered; as well as reactions between beam-target reaction products and aluminium. This situation is less likely to happen given that alignments between the beam trajectory and the target was checked during measurements.

4.5 Gamma-ray energy spectra

The γ-ray energy spectrum is generated as the respond of the LEPS. It informs on different reactions that took place in the target. Different behaviours are observed depending on the beam characteristics, namely its energy and its state (on or off). In this regard, γ-rays observed during the beam-on sequence are emitted by stable nuclei or unstable nuclei with a half life long enough for the said

nuclei to still be in its decay process at the beginning of the beam-off sequence. During the beam-off sequence, only reaction products, emitting a γ-ray during their decay are observed. Moreover, some reaction channels can only be opened at specific beam energies.

Background spectra are also presented. In each case, background spectra are normalised using a time parameter. The time parameter here is a coefficient obtained by considering the duration of the data collection when the beam is bombarding the kapton film, as compared to the data collection with the beam on the target.

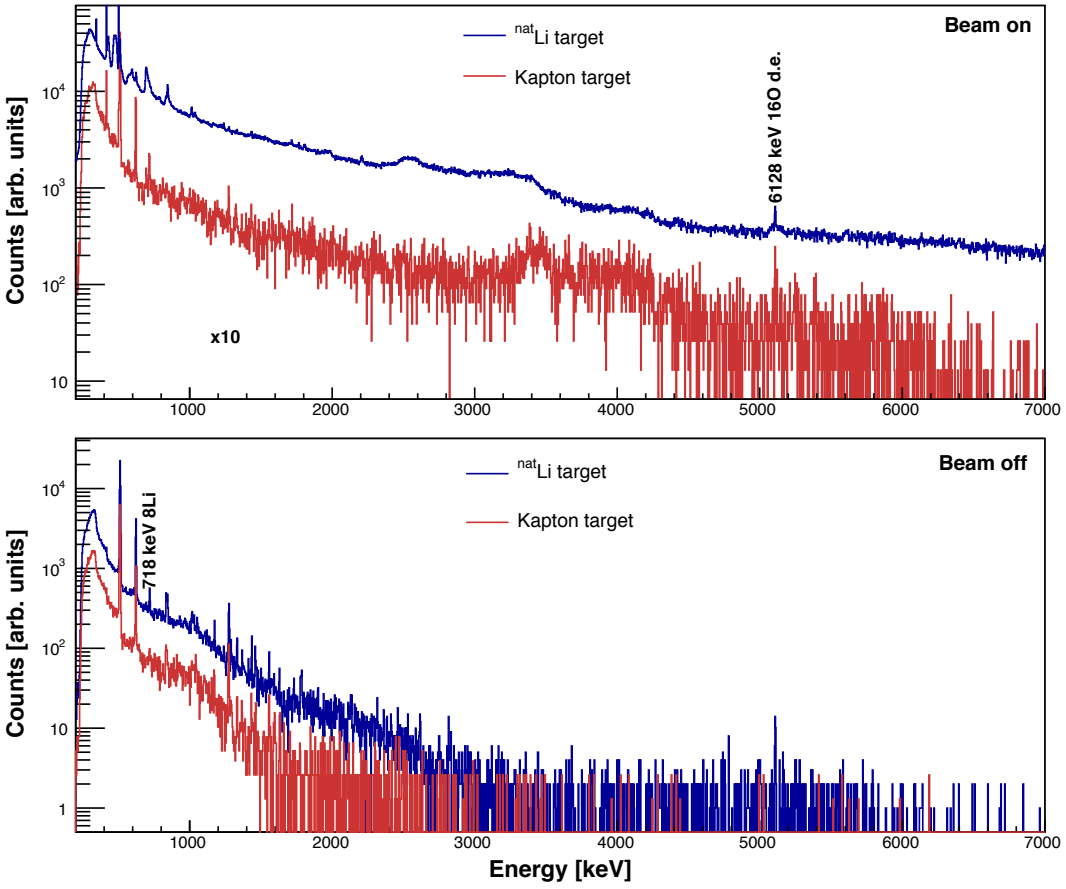

Figure 4.10: Gamma-ray energy spectra of ^{nat}Li and kapton targets for the proton beam at E_{lab}= 50 MeV, in the case when beam is on (top) and off (bottom).

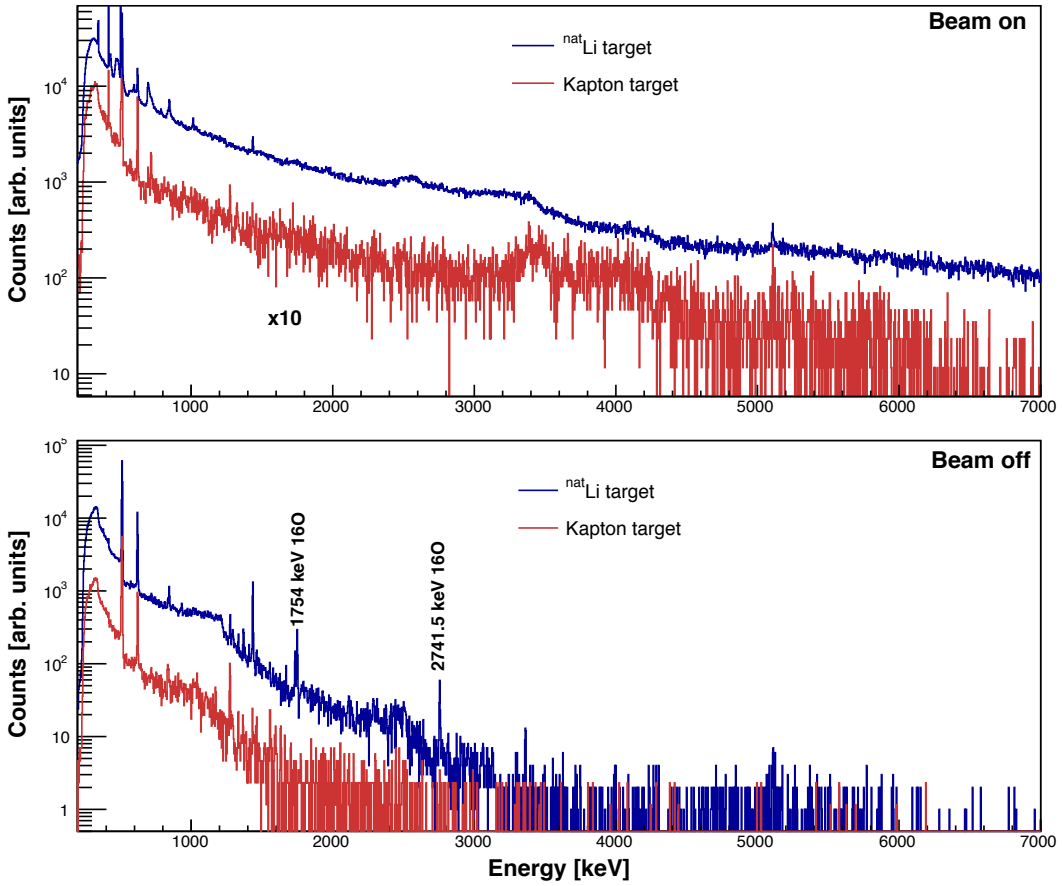

Figure 4.11: Gamma-ray energy spectra of ^{nat}Li and kapton targets for the proton beam at E_{lab}= 66 MeV, in the case when beam is on (top) and off (bottom).

Figure 4.10 and Figure 4.11 show γ-ray energy spectra resulting from the p+^{nat}Li reaction for beam energies of 50 MeV and 66 MeV respectively. At low energies, the 429 keV transition excited by the ^{7}Li(p,p) reaction when the beam is on, as well as the 718 keV γ-ray resulting respectively from the decay of ^{8}Li during the beam-off sequence are observed. The peak at 5106 keV most probably is the double escape peak of the 6128 keV γ-ray from ^{16}O, originating from the kapton film, since the same peak is observed on the background spectrum. This peak is also observed in both the p+^{9}Be and the p+^{nat}B reactions. Additional ^{16}O peaks are observed during the beam off at 1754.9 keV and 2741.5 keV, from the decay of ^{16}N. These peaks are more visible for a beam energy of 66 MeV and could come as the result of the oxidation of ^{7}Li. The ^{16}O peaks could also be considered as the product of the decay of ^{20}Na, produced from the interaction between the sodium contaminant and protons.

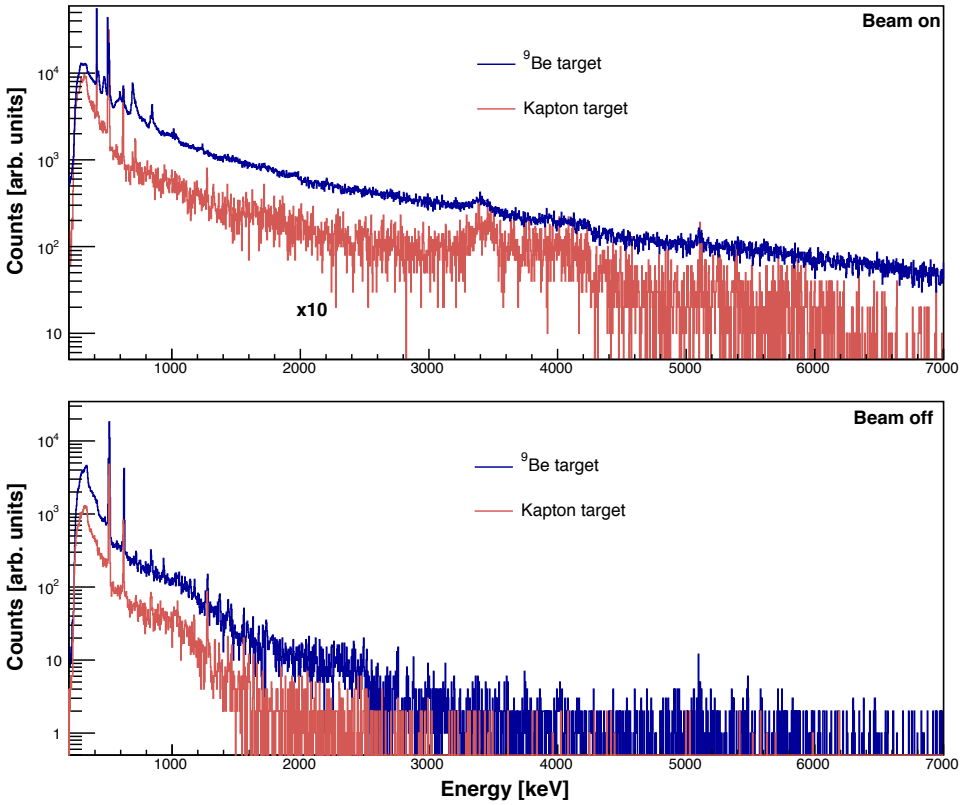

Figure 4.12: Gamma-ray energy spectra of ^{9}Be and kapton targets for the proton beam at E_{lab}= 50 MeV, in the case when beam is on (top) and off (bottom).

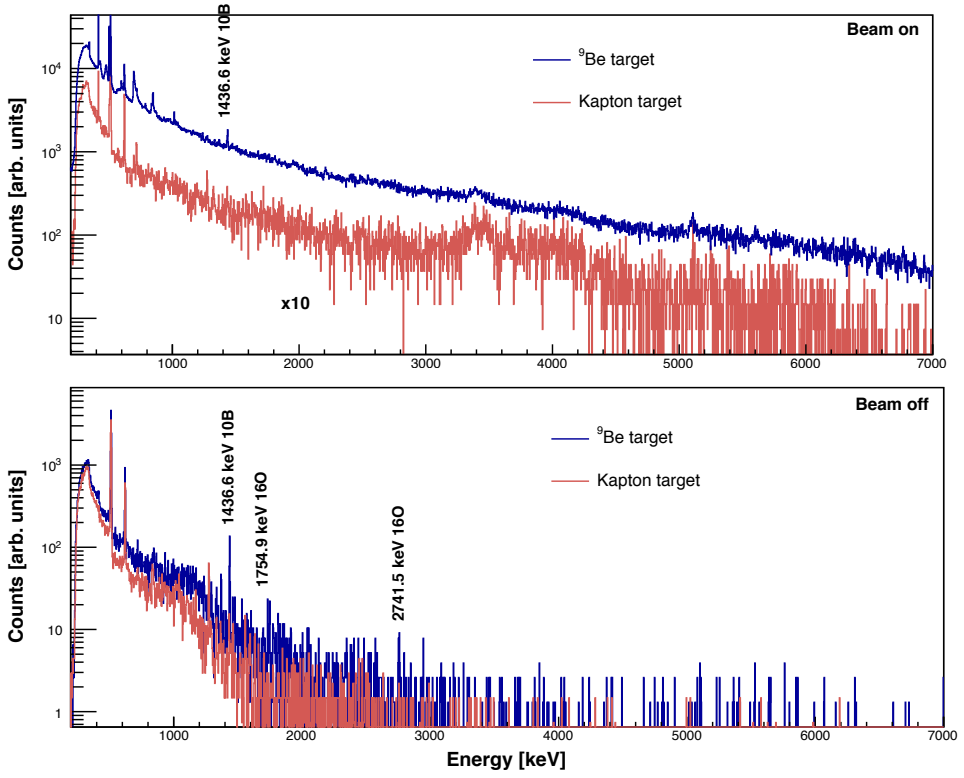

Figure 4.13: Gamma-ray energy spectra of ^{9}Be and kapton targets for the proton beam at E_{lab}= 66 MeV, in the case when beam is on (top) and off (bottom).

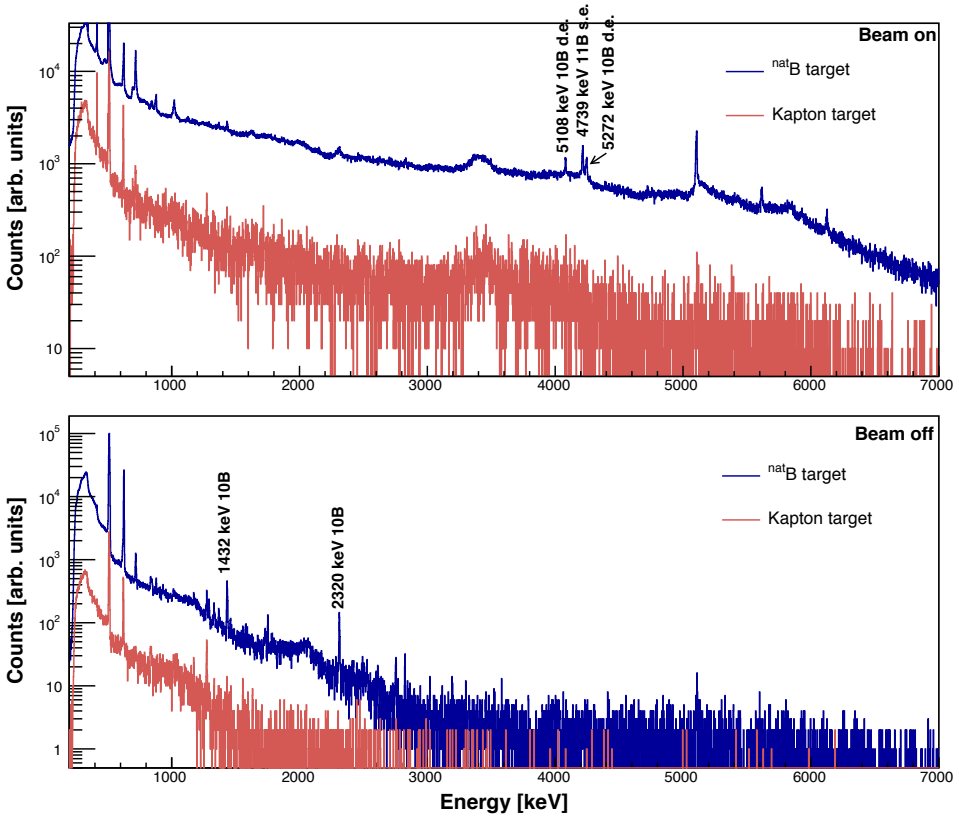

Figure 4.14: Gamma-ray energy spectra of ^{nat}B and kapton targets for the proton beam at E_{lab}= 50 MeV, in the case when beam is on (top) and off (bottom).

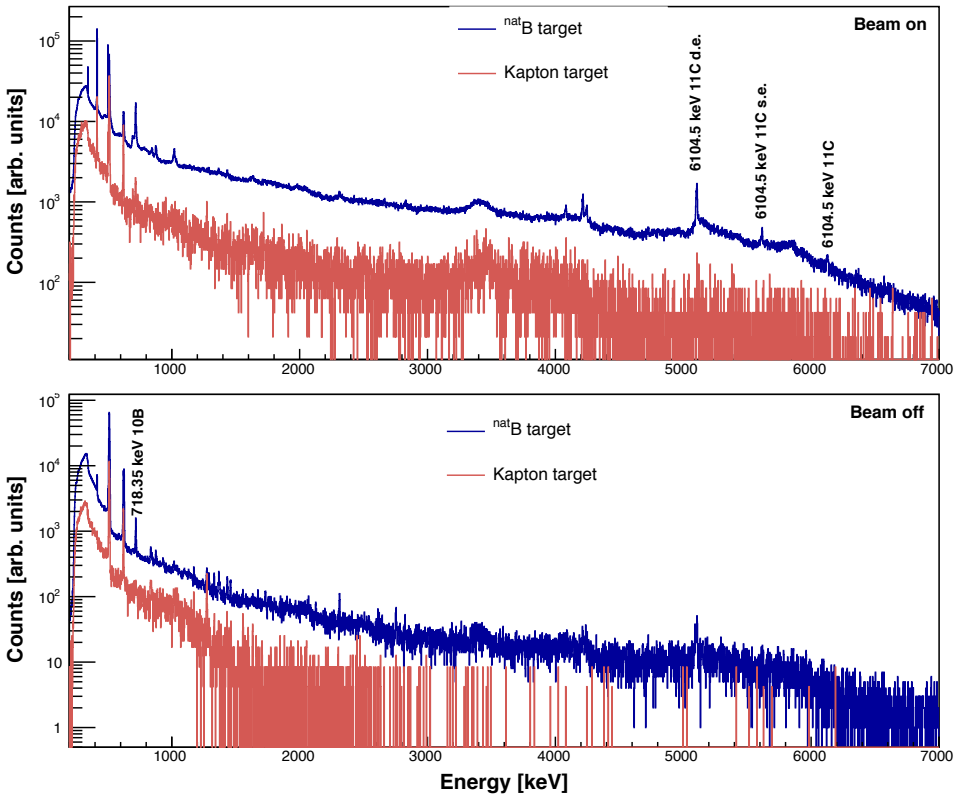

Figure 4.15: Gamma-ray energy spectra of ^{nat}B and kapton targets for the proton beam at E_{lab}= 66 MeV, in the case when beam is on (top) and off (bottom).

The energy spectra of p+^{9}Be reactions presented in Figure 4.12 and Figure 4.13 for beam energies of 50 MeV and 66 MeV respectively, display some ^{10}B photopeaks at 1435.6 keV.

Natural boron consists of about 80% of ^{11}B and 20% of ^{10}B. Their interaction with protons result mostly in the production of ^{10}B, ^{11}B, ^{10}C and ^{11}C as shown in Figure 4.14 and Figure 4.15. All these nuclei are produced during the beam-on sequence from ^{10}B(p,p), ^{10}B(p,n), ^{11}B(p,p) and ^{11}B(p,n). The production of ^{10}B and ^{11}B is sustained during the beam-off sequence by the decay of ^{10}C and ^{11}C respectively. The long half-life of ^{10}C (19 s) and of ^{11}C (20 min) allows the isotopes to still be present by the next beam-on sequence.

4.6 Energy loss calculations

In order to generate the Fermi-Kurie plot, one needs to have an estimation of the total energy of emitted electrons. In a first assumption, ΔE represents the energy deposited by electrons in the active area of the paddle. Since electrons have a high probability of interacting with any absorbing material, ΔE needs to be corrected taking into account the energy deposited by electrons in other materials else than the active area of the paddle.

From the interaction site in the target to the LEPS crystal, emitted β-particles travel through the kapton window, the paddle and the beryllium window at the entrance of the LEPS, before interacting with the germanium crystal. Assuming that the proton induced reaction takes place in the center of the target, emitted β-particles will travel through half of the target thickness to the vaccum. No energy loss is recorded in the vaccum. Electrons then interact with the 12 μm kapton film, followed by an air gap of 20.5 mm between the kapton film and the paddle. As previously described, paddles are made of three materials, a 5 mm plastic scintillator covered by a 17 μm aluminium foil and a 0.2 mm cardboard paper. Meaning that, electrons will go through two layers of paper and two layers of aluminium foil, with one layer on each side of the scintillator. The LEPS beryllium window has a thickness of 300 μm. Figure 4.16 shows the position of each layer with their thicknesses and densities, forming what will be referred to as the compound material.

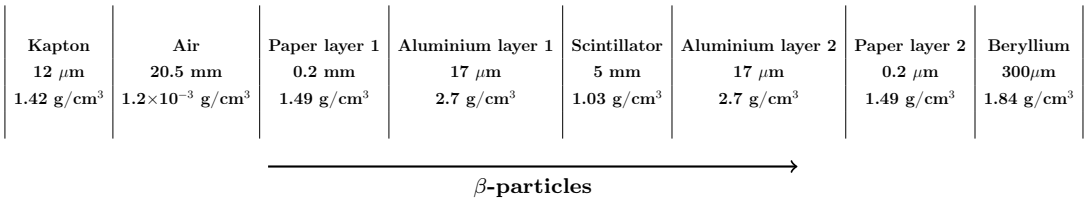

Figure 4.16: β-particles travel through all the layers following the arrow. The paddle is made of one layer of plastic scintillator, two layers of aluminium and two layers of paper.

The Bethe-Bloch formula in Equation 2.10, giving the stopping power for β-particles, is used in this case. The stopping power was calculated using ESTAR [45], the online stopping power calculator from NIST (National Institute of Standards and Technology). Knowing the density and thickness of each material, the energy loss was deduced. Since electrons follow the same path regardless of the target used, the only factor that differs in each case is the target density and thickness. Consequently, the energy loss is evaluated for individual targets. Figure 4.17 shows the energy loss of electrons from the center of the target to the beryllium window. It gives the total energy loss dE as a function of the energy E of emitted β-particles. The energy loss is calculated for individual layers by considering the outgoing energy of a previous layer to be the incident energy of the current one. For instance the energy of β-particles exiting the kapton film is considered as the incident energy of the first paper layer, whose output is the incident energy of the first aluminium layer. The process is repeated until all layers have been considered. The total energy loss is obtained by either summing energy losses in individual layers, or by subtracting the final outgoing energy E_{out} from the initial incident energy. Cellulose nitrate and vinyltoluene were respectively used for the paper and the plastic scintillator material in the stopping power calculation.

There is a value below which the energy loss is equal to the incident energy, that is, electrons with an energy below that value lose all of their energy in the target or in the compound material. This value is estimated at 1 MeV, 1.5 MeV and 1.2 MeV for Li, Be and B targets respectively.

The goal behind the energy loss calculation is to establish a relationship between the total energy E of electrons emitted during the decay and the residual energy E_r from the LEPS. In this regard, a linear relation can be established between

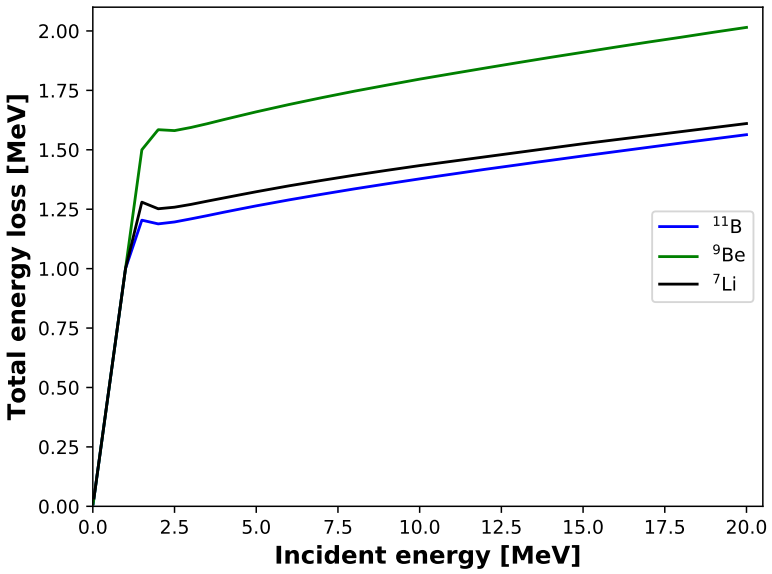

Figure 4.17: Layers composing the compound material. The total energy loss is plotted as a function of the energy of emitted β-particles. The linear distribution observed below ~1.5 MeV indicates that electrons with energy in that area lose all their energy within the compound material.

the total energy of emitted electrons E and the total energy E_{out} of electrons exiting the compound material. This is obtained by plotting E against E_{out}, which follows a linear distribution. A linear equation is extracted for each target as follows:

$$E = 1.02E_{out} + 1148 \text{ [keV] for } ^{7}\text{Li}, \tag{4.7a}$$

$$E = 1.02E_{out} + 1558 \text{ [keV] for } ^{9}\text{Be}, \tag{4.7b}$$

$$E = 1.02E_{out} + 1224 \text{ [keV] for } ^{11}\text{B}. \tag{4.7c}$$

E_{out} is the energy of electrons entering the LEPS and should be equal to the energy detected by the latter. The question at this point is to find out if all electrons impinging on the germanium crystal are absorbed. The energy loss of electrons in the LEPS detector can be estimated by considering that LEPS' are made of a 0.7 mm lithium drifted region and a 0.3 μm boron diffused contact, making a total thickness of 10 mm. The larger amount of energy is lost in the germanium crystal. Electrons lose approximately 50 to 90 keV in the 0.7 mm thick lithium layer and less than 0.1 keV in the 0.3 μm thick boron layer. These losses are negligible compared to the 10 MeV deposited in a 10 mm germanium crystal by a 10.2 MeV electron for instance. The energy loss in the LEPS is not

influenced by the type of target. Electrons entering the LEPS with an energy below 10.2 MeV are fully stopped. Above this value, they deposit some energy and exit the detector with an energy E'_{out}. This energy corresponds to the energy lost in the detector's dead layers and will not contribute to the signal. The product of p+^{7}Li undergoing a β^{-}-decay is ^{6}He with a Q-value of 3.5 MeV, thus emitted electrons have an energy between 0 and 3.5 MeV. An electron with 3.5 MeV will lose on average 1.28 MeV before reaching the LEPS. The remaining energy, 2.2 MeV, is less than 10.2 MeV, meaning that electrons resulting from the decay of ^{6}He are fully absorbed. As a consequence, E_{out} is equal to the energy detected by the LEPS, that is E_r. Thus, the total energy is extracted as follow:

$$E = 1.02E_r + 1148 \text{ [keV]}. \tag{4.8}$$

The highest Q-value in this study is 16 MeV resulting from the decay of ^{8}Li, produced by both boron and beryllium targets. When considering the ^{9}Be target, electrons emitted with an energy of 16 MeV lose approximately 1.9 MeV in the target and the compound material before reaching the crystal. For the ^{11}B target, electrons with that same energy will lose about 1.5 MeV before the germanium crystal. In both cases, the remaining energy is greater than 10.2 MeV, meaning that some electrons are able to reach the detector's dead layer. In such situations, the energy of the electrons entering the LEPS is given by $E_{out} = E_r + E'_{out}$. By expressing E'_{out} as a function of E_r, Equation 4.7c and Equation 4.7b can be corrected. The expression of the total energy of emitted electrons as a function of the residual energy is given by Equation 4.9 and Equation 4.10 for both beryllium and boron targets respectively.

$$E = 1.6E_r + 1558 \text{ [keV] for } {}^{9}Be \tag{4.9}$$

$$E = 1.6E_r + 1224 \text{ [keV] for } {}^{11}B. \tag{4.10}$$

4.7 Fermi-Kurie plot

The Fermi-Kurie plot shows the total energy distribution of electrons emitted during the decay of products, in which the square root of the number of β-particles emitted with an energy lying within a certain narrow range, divided by the Fermi function, is plotted against β-particle energy. It is generated by

applying Equations 4.8, 4.9 and 4.10 on the LEPS output, therefore taking into account the total energy loss. LEPS' and paddles outputs are observed in coincidence in this case. The notation "coincidence" simply means observing electrons that traversed both detectors. Electron spectra are generated using the section of the data collected during beam-off sequences.

4.7.1 Lithium target

The decay of ^{6}He into ^{6}Li is accompanied by the emission of electrons with energies up to 3507.8 keV. To verify that ^{6}He were indeed produced by the p+^{7}Li reaction, the electron spectrum needs to be plotted with the endpoint at 3507.8 keV. The first step is to generate the ΔE-E plot, which consists in plotting the output of the paddle against the output of the LEPS. It represents events describing electrons that deposited some energy in the paddle and were stopped or were able to traverse the LEPS. The ΔE-E matrix obtained from the p+^{nat}Li reaction at 50 MeV is shown in Figure 4.18. This corresponds to electrons emitted by all the products of the p+^{nat}Li reaction undergoing a β-decay; including those produced by the interaction of the proton beam with the kapton film. The ordinate is given in channel numbers since the paddles were not calibrated. For this task, the only usable area is the one delimited on the ordinate by 400 and 2000 [Ch. number] approximately. The notation "Ch. number" stands for channel number. Events below 400 [Ch. number] are attributed to electronic noise and some background noise from the kapton film.

This plot only includes the output of each detector and thus does not take into consideration the energy lost in other media. Recalling the correction performed on the energy loss in Section 4.6 by accounting for the energy loss in the kapton film of the target chamber, the air gap, the paper, the aluminium foil, as well as the beryllium window, the total energy of emitted electrons can be extracted using Equations 4.8 to 4.10. Given that electrons emitted from the decay of ^{6}He have an energy of 3507.8 keV, the linear distribution described by Equation 4.8 is used to plot the electron energy spectrum. The energy of electrons detected by the LEPS (E_r) is obtained by making a projection of the usable area in Figure 4.18 on the abscissa. Equation 4.8 is applied to the resulting output to generate the histogram in Figure 4.19.

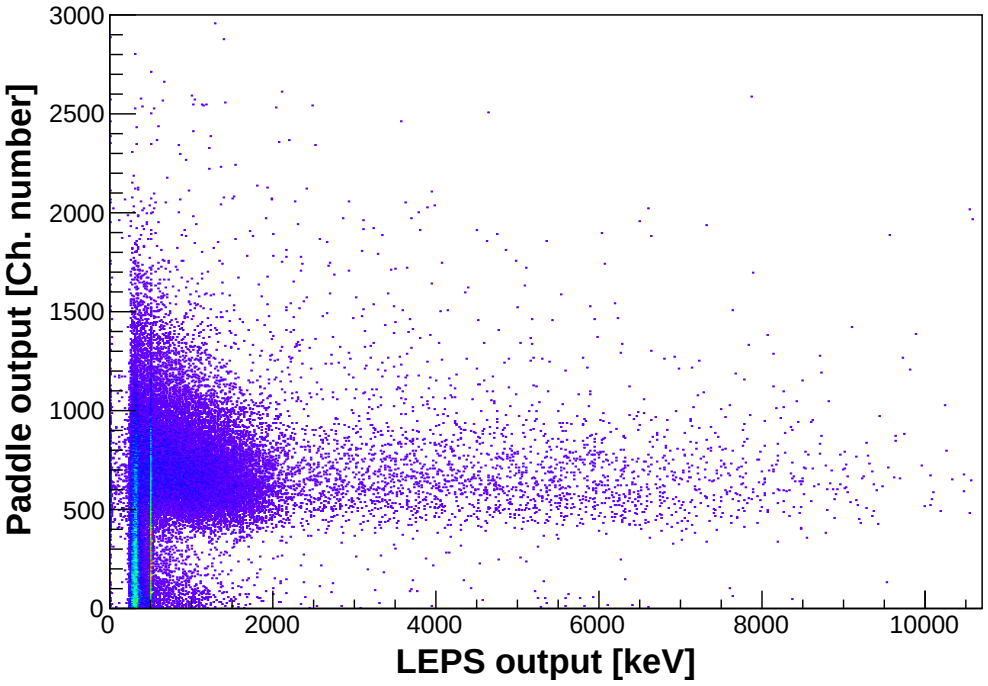

Figure 4.18: ΔE-E matrix for the p+^{nat}Li reaction. This corresponds to the output of detectors without accounting for the energy loss of electrons before the LEPS.

The empty space observed below 1200 keV in Figure 4.19 corresponds to the energy lost by electrons before reaching the LEPS. From 1900 keV to about 4000 keV, the electron energy distribution adopts a shape similar to that of a Fermi-Kurie plot. The distribution then drops around 3.5 MeV, corresponding to the Q-value of the decay of ^{6}He into ^{6}Li. This shape sits on top of a background considered to be an extension of the segment of the spectrum found between 4000 keV upward. The decay of ^{6}He observed in this case is confirmed by observing the decay curve in Figure 4.20, obtained by plotting the beam-off time spectrum for events corresponding to an energy between 1.2 MeV and 3.5 MeV. Such energy interval is considered due to the fact that the energy lost by electrons emitted with an energy between 0 and 3.5 MeV, before reaching the LEPS crystal, varies approximately from 0 to 1.2 MeV.

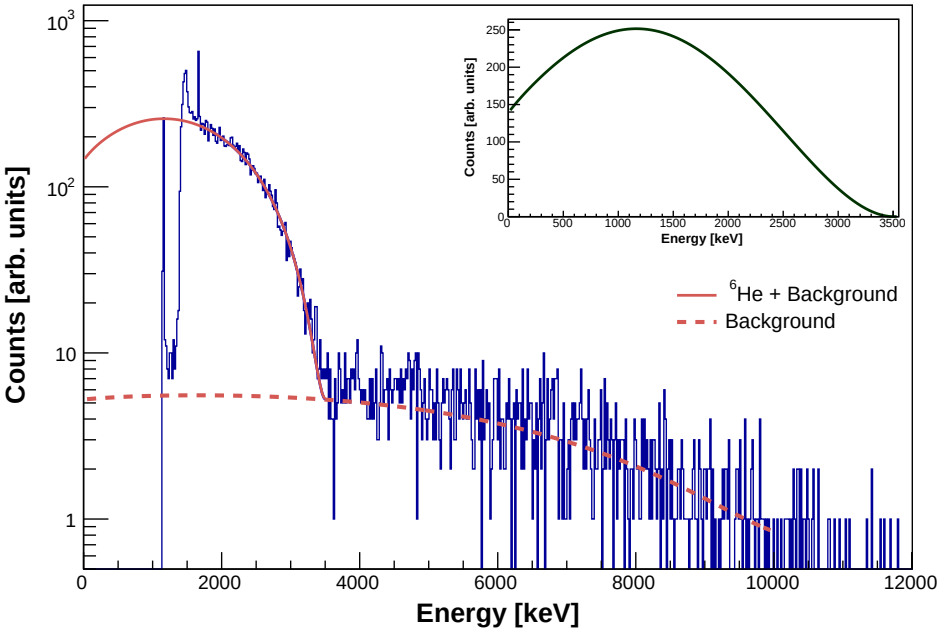

Figure 4.19: Electron energy spectrum of the decay of ^{6}He. The function giving $N(T_e)$ is used to fit the spectrum from 1900 keV to 3507.8 keV. The resulting function with fitting parameters is extrapolated to low energies following the red line. The background is also fitted in the same manner. The Fermi-Kurie plot with subtracted background is represented by the dark curve on the upper right of the figure.

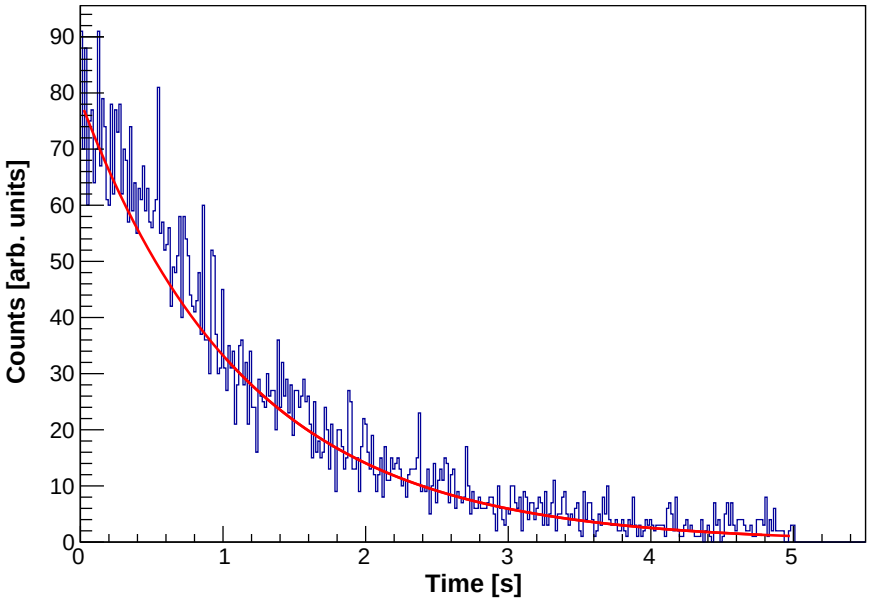

Figure 4.20: Decay curve of ^{6}He, with a decay constant of 0.861± 0.023 s^{-1}. This is obtained for E_{lab}=50 MeV.

During measurements using the ^{nat}Li target, the beam was turned on for 4.8 s and off for 5.2 s, making a cycle of 10 s. Only events observed during the beam-off sequence are considered in analysing the decay of products. Events bellow 0.2 s are discarded in order to limit as much as possible, background due to the decay of nuclei with very short half lives. The decay curve in Figure 4.20 is fitted with an exponential function. The experimental decay constant obtained from the fit is 0.861± 0.023 s^{-1}, range within which can be found the theoretical value of the decay constant of ^{6}He, 0.859 s^{-1}.

The background in Figure 4.19, displays a shape similar to that of a Fermi-Kurie plot, with an endpoint around 10 MeV. In order to determine which nuclei are responsible for such distribution, the time spectrum is plotted in Figure 4.21 with the energy set between 4000 keV and 12000 keV. By fitting the time spectrum using an exponential function and considering a linear background, an experimental decay constant of 1.506±0.137 s^{-1} is deduced, corresponding to a half life of 0.460± s. Given that none of the products resulting from the p+^{nat}Li reaction decays with such decay constant, the most plausible candidate is considered among contaminants. Recalling from previous statements, the interaction between the kapton film (consisting of carbon, nitrogen and oxygen) could result in the production of contaminants, in addition to which contaminants from the target (from oxidation and from sodium contamination) could be considered. In this regards, ^{20}Na was observed as the best candidate, since it produces ^{16}O by undergoing a β-delayed α emission with a Q-value of 9162.7 keV and a half-life of 0.448 s, that is a decay constant of 1.547 s^{-1}. It can therefore be concluded that the background following the Fermi-Kurie distribution in Figure 4.19 originates from the decay of ^{20}Na.

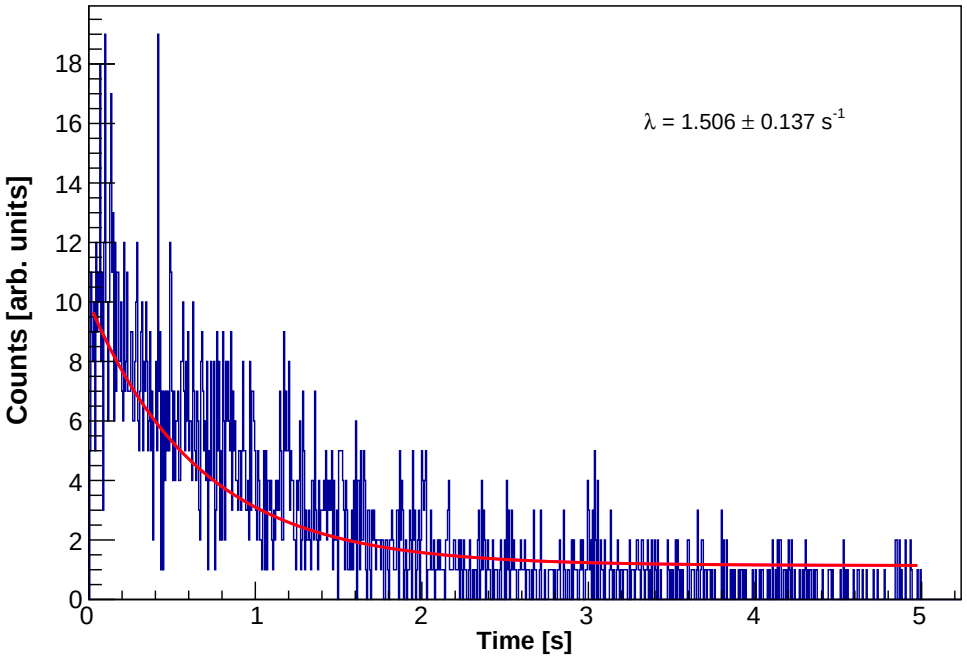

Figure 4.21: Time energy spectrum corresponding to background due to contaminants, obtained when setting an energy gate between 4 MeV and 11 MeV.

The total number of ^{6}He can be extracted by fitting the energy spectrum in Figure 4.19 using Fermi's equation, which expresses the total number of electrons or positrons emitted during the decay as a function of their kinetic energy, that is

$$N(T_e) = C|M_{if}|^2 F(Z, T_e) p^2 [\sqrt{T_e^2 + 2T_e m_0 c^2}(Q - T_e)^2 (T_e + m_0 c^2). \qquad (4.11)$$

In this equation, m_0c^2 and Q are known constants and can be set as fixed parameters, that is 511 keV and 3507.8 keV respectively. $C|M_{if}|^2$ on the other hand informs on the forbiddeness of the interaction and is specific to each reaction. It can as such be set as a fitting parameter. In the expression of the Fermi function, $F(Z,p) = \eta/(1 - e^{-\eta})$, where $\eta = \pm\frac{2\pi Z_D c}{137v} = \kappa/v$, the factor κ has the characteristics of the daughter nucleus. It is thus set as the second fitting parameter. The fitting process consists of setting a fitting interval with the upper limit equal to the endpoint of the plot, corresponding to the β-decay Q-value of the nucleus of interest (3507.8 keV for instance). The lower limit of the interval is set at different positions. For each position, the spectrum is fitted until the best fit is obtained. The best fit corresponds to a situation whereby the χ^2 minimization

is observed, that is $(\chi^2/ndf)\simeq 1$, and where the value of κ is positive since $\eta>0$ for electrons.

The first step of the fitting process consists on fitting the section from 4000 keV upward using Equation 4.11 associated to a polynomial equation, by setting the lower limit to 9771.7 keV. The polynomial equation accounts for any other background. The function obtained from such a fit is extrapolated to low energies and serves as background for the next fit to be performed between 1900 keV and 3507.8 keV. In the later case, the histogram is fitted using Equation 4.11 and the extrapolated function. Once the best fit has been obtained for the ^{6}He spectrum, values of each fitting parameter are substituted in the expression of $N(T_e)$. This new expression is extrapolated to low energies as represented by the red curve in Figure 4.19. After background subtraction, the curve on the upper right of Figure 4.19 is generated, and follows the actual shape of the Fermi-Kurie plot for the decay of ^{6}He. The total number of electrons is deduced by integrating the function defining this new curve from 0 to 3507.8 keV. Fitting parameters obtained in this case are presented in Table 4.4.

Table 4.4: Parameters obtained after fitting electron spectra.

Beam energy	χ^2/ndf	$C\|M_{if}\|$	κ
50 MeV	1.0644	$(8.2\pm1.1)\times10^{-12}$	$(2.8\pm0.9)\times10^{3}$
66 MeV	1.1781	$(5.4\pm1.6)\times10^{-13}$	$(5.4\pm1.6)\times10^{4}$

4.7.2 Beryllium target

The interaction of ^{9}Be and a proton beam produces ^{8}Li and ^{8}B through ^{9}Be(p,2p) and ^{9}Be(p,2n) reactions respectively. The β^--delayed α emission of ^{8}Li consists of its decay into ^{8}Be with a Q-value of 16005.2 keV, followed by the break up of ^{8}Be into two α-particles. A similar process is observed in the case of ^{8}B, with the break up of ^{8}Be being preceded by a β^+-delayed α emission and a Q-value of 16956.8 keV.

Many nuclei are produced in this reaction, some of which can undergo a β-decay. This is the case of ^{6}He populated by the ^{9}Be(p,p^{3}He) reaction. Nuclei produced from the interaction of protons with the kapton film can also be considered. However, none of these nuclei undergo a β-decay with Q-values are greater than

10 MeV. In order to confirm the production of ^{8}Li and ^{8}B, the time spectrum is plotted, by setting a gate on the energy. It has previously been established that β-particles emitted with an energy close to 17 MeV lose approximately 1.5 MeV of their energy in the paddle and LEPS entrance window before impinging on the LEPS crystal. Taking this into consideration, an energy gate is set between 10 MeV and 16.96 MeV (10 MeV to discard low Q-values). Figure 4.22 shows the decay curve obtained in such manner. It represents the decay of a mixture of the two nuclei of interest. Such decay can be described by the following equation:

$$N(t) = N_1 e^{-\lambda_1 t} + N_2 e^{-\lambda_2 t} \tag{4.12}$$

where N_1 and N_2 are the initial numbers and λ_1 and λ_2 the decay constants of the two nuclei of interest.

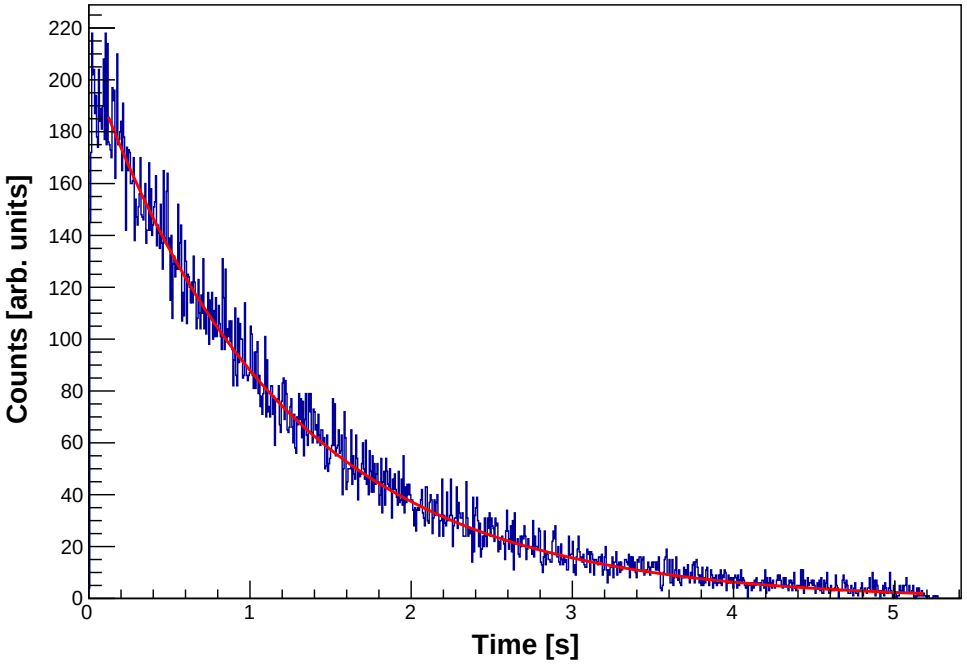

Figure 4.22: Decay curve of ^{8}Li and ^{8}B for a decay time of 5.2 s.

When using the function defined by Equation 4.12 (and a first degree equation for background) to fit the curve in Figure 4.22, values of experimental decay constants are extracted: λ_1=0.89±0.16 s^{-1} and λ_2=0.89±0.031 s^{-1}. The real decay constant of ^{8}B and ^{8}Li, that is 0.899 s^{-1} and 0.825 s^{-1} respectively, lie within the ranges of experimental values. Since only electrons and positrons of energies between 10 MeV and 17 MeV are considered here, N_1 and N_2 correspond

to an underestimated value of the total number of products needed in determining the decay rate. This situation is however corrected using the Fermi-Kurie plot.

Plotting the Fermi-Kurie curve consists of determining if the electron spectrum of the decay of ^{8}Li and ^{8}B drops to zero at 16 MeV and 16.9 MeV respectively. The same procedure as in Section 4.7.1 is observed. The ΔE-E matrix is represented in Figure 4.23. The paddle's output is plotted on the ordinate in channel number and the LEPS output is plotted on the abscissa. The part of the ΔE-E matrix necessary in generating the Fermi-Kurie plot is the area delimited on the ordinate by 400 to 2500 [Ch. numbers]. This area corresponds to the electron distribution, characterised by the decreasing number of electrons towards the endpoint. In order to reduce events due to contaminants, as well as to discard very low half lived nuclei and to limit the number of β-particles emitted by nuclei with very long half lives, ΔE-E matrix is plotted for one half life of ^{8}Li (0.84 s). A time gate is therefore set between 0.1 s and 0.94 s. It can be observed at this point that the projection of the area of interest on the abscissa will result into an electron spectrum with the endpoint around 11 MeV, corresponding to the residual energy (E_r) measured by the LEPS.

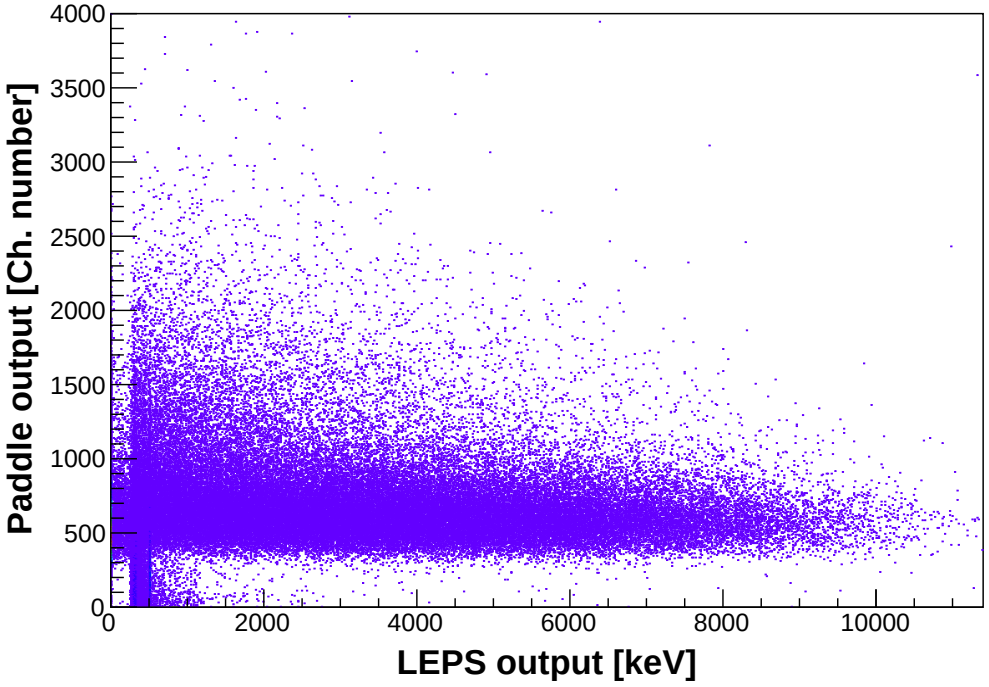

Figure 4.23: ΔE-E matrix for the p+^{9}Be reaction. This corresponds to the output of detectors without accounting for the energy loss of electrons before the LEPS, thus the endpoint around 11 MeV.

A correction can be performed on the energy, similar to that used in the case of ^{nat}Li. Therefore, the expression of the total emitted energy as a function of the residual energy, defined by Equation 4.9, is applied to the projection of the area of interest on the abscissa. The resulting histogram is presented in Figure 4.24. Above 4 MeV, the spectrum takes the shape of the Fermi-Kurie plot and drops around 16 MeV.

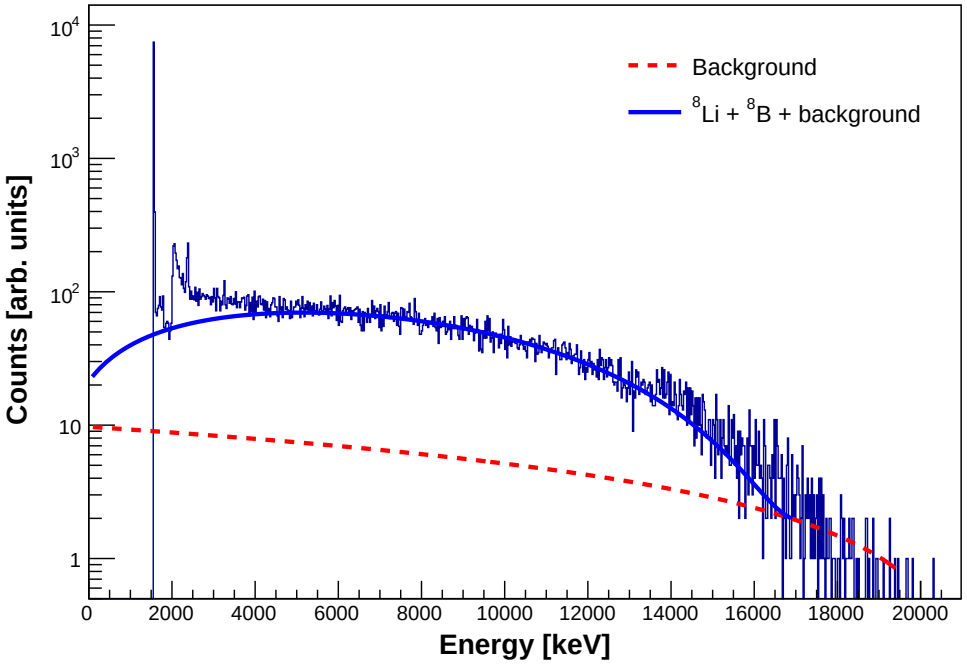

Figure 4.24: Electron energy spectrum of the decay of products of the p+^{9}Be reactions, measured during one half-life of ^{8}Li.

The Q-values of ^{8}Li and ^{8}B are very close (16 MeV and 16.96 MeV), which makes it difficult to distinguish their endpoints. Furthermore, they have very close half lives, that is 0.84 s for ^{8}Li and 0.77 s for ^{8}B. These conditions make it difficult to determine which nuclei are actually decaying just by observing the electron spectrum. The histogram is fitted using the $N(T_e)$ function and a linear background, considering $C|M_{if}|^2$ and κ as fitting parameters. The first fit is performed with the upper limit fixed at 16.96 MeV. Once the best fit has been obtained, for energies bellow 4 MeV, the fitting parameters are substituted in the expression of $N(T_e)$ and the function is extrapolated to low energies. The conditions for a good fit are $C|M_{if}|^2>0$ and $(\chi^2/ndf)\simeq 1$. The function is integrated from 0 to 16956.8 keV in order to determine the total number N_t of ^{8}B and ^{8}Li produced during one half life of ^{8}Li. If $N_{^8Li}$ and $N_{^8B}$ are the total

number of ^{8}Li and ^{8}B to have decayed after 0.84 s respectively, N_t is expressed as

$$N_t = N_{^8Li} + N_{^8B}. \tag{4.13}$$

The decay curve in Figure 4.22 is fitted using Equation 4.12 while fixing λ_1 and λ_2 to the decay constants of ^{8}Li and ^{8}B respectively. Using values of N_1 and N_2 deduced from the fit, the total number of ^{8}Li and ^{8}B to have decayed after 0.84 s, namely $N'_{^8Li}$ and $N'_{^8B}$ respectively, are determined. These new values are obtained during the beam-off sequence for energies between 10 MeV and 16.96 MeV. N_t is determined for energies between 0 and 16.96 MeV. It therefore exists a proportionality coefficient defined in such a way that,

$$\frac{N_{^8Li}}{N'_{^8Li}} = \frac{N_{^8B}}{N'_{^8B}}. \tag{4.14}$$

Since N_t, $N'_{^8Li}$ and $N'_{^8B}$ have known values (obtained from fits), Equation 4.13 and Equation 4.14 are considered as a system of equations with two unknowns $N_{^8Li}$ and $N_{^8B}$. The solution to these equations leads to the expression of the total numbers of ^{8}Li and ^{8}B as follows:

$$N_{^8Li} = \frac{N'_{^8Li}}{N'_{^8Li} + N'_{^8B}} N_t \quad \text{and} \quad N_{^8B} = \frac{N'_{^8B}}{N'_{^8Li} + N'_{^8B}} N_t. \tag{4.15}$$

Fitting parameters obtained when performing fits on Fermi-Kurie plots are presented in Table 4.5.

Table 4.5: Parameters obtained after fitting Fermi-Kurie plots for ^{8}Li and ^{8}B.

Beam energy	χ^2/ndf	$C\|M_{if}\|$	κ
50 MeV	1.2732	$(1.45\pm0.19)\times10^{-17}$	$(5.01\pm0.67)\times10^{6}$
66 MeV	1.3796	$(1.6\pm0.1)\times10^{-17}$	$(6.9\pm0.4)\times10^{6}$

4.7.3 Boron target

The ^{nat}B target is used to produce all four of the nuclei of interest in this work, that is ^{6}He (0.807 s), ^{8}He (0.119 s), ^{8}Li (0.84 s) and ^{9}Li (0.178 s). Just like in the case of the ^{9}Be target, ^{8}B (0.77 s) can also be considered. Electrons are collected all together, regardless of the decay from which they were emitted. The

electron spectrum generated is therefore considered as sum of electron spectra resulting from all products undergoing β-decay. The ΔE-E matrix is represented by Figure 4.25. The region extending from channel 400 to 2500 [Ch. number] on the ordinate is projected on the abscissa. The resulting electron energy spectrum is corrected for the energy loss using Equation 4.10.

The continuous energy distribution of β-particles makes it difficult to identify desirable events, given that it encompasses events for all decay taking place at the same time. An approach that can be considered to remove as much undesirable events as possible is to set a time gate, such as to observe only events taking place during an interval of time corresponding to one half life of the nucleus of interest. For instance, the energy spectrum of electrons emitted from the decay of ^{8}Li can be obtained by setting a time gate of 0.84 s.

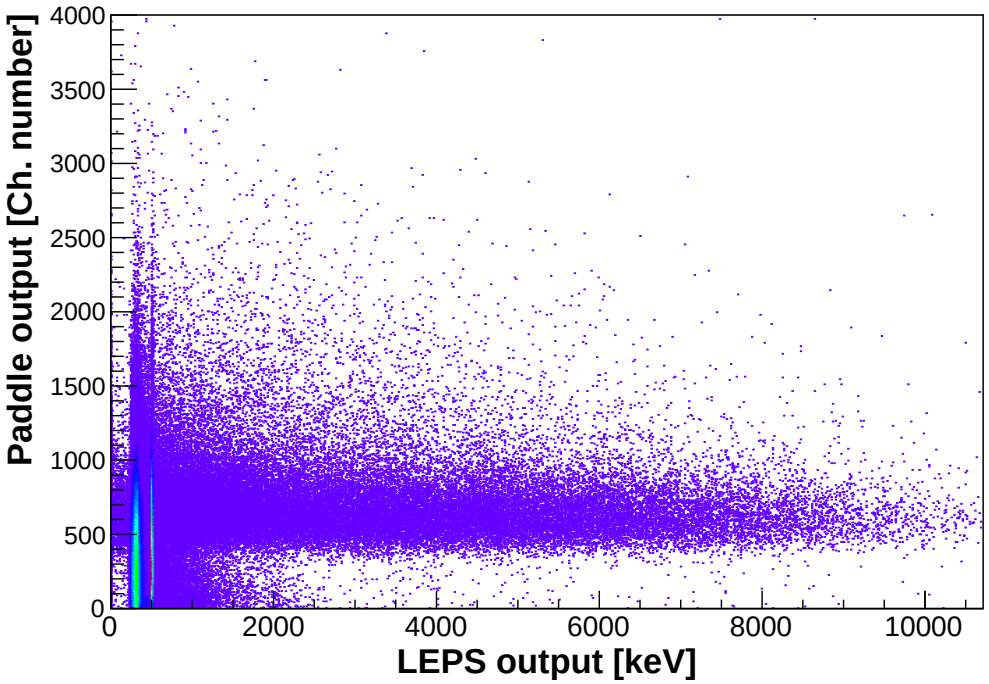

Figure 4.25: ΔE-E matrix for the p+^{nat}B reaction.

Measurements were performed during three time sets; one for t_{on}=0.8 s and t_{off}=1.2 s, another set for t_{on}=1.2 s and t_{off}=0.8 s and the last set for t_{on}=4.8 s and t_{off}=5.2 s. In the first two cases, there is a possibility of extracting all nuclei of interest, since the beam-off time is short enough for the decaying nuclei to still be present at the end of the sequence. For each of these two cases, nuclei adopt similar behaviours in the sense that, short half lived nuclei decay completely,

while longer half lived nuclei decay for more or less their half lives. In the last case, the beam-off sequence is long enough for the majority of nuclei to have completely decayed at the end of the sequence. However, since events observed are a result of β-particles, a trace of β-particles emitted during the decay of nuclei with short half lives can still be observed at the beginning of the beam-off sequence, even though they are completely non-existent toward the end of the sequence.

Similar approaches are used for t_{off}=1.2 s and t_{off}=0.8 s. At the beginning of the sequence, after 0.5 s for instance, the activity is mainly governed by a fast decay of ^{8}He and ^{9}Li and a slower decay of ^{8}Li and ^{8}B. After 0.5 s (about four times the half lives of ^{8}He and ^{9}Li), The number of β-particles from ^{8}He and ^{9}Li decreases while ^{8}Li and ^{8}B are still in their first half life at the end or the sequence. A similar situation can be observed for t_{off}=5.2 s, with the difference that ^{8}Li and ^{8}B are almost non existent at the end of the sequence.

If a time gate is set for one half life of ^{9}Li, electron spectra represented in Figure 4.26 and Figure 4.27 are obtained for t_{off}=1.2 s and t_{off}=5.2 s respectively. These spectra represent all β- particles emitted after 0.178 s. Equation 4.11 is used to fit the histogram, following the same procedure as described in Section 4.7.1 and Section 4.7.2. Since ^{8}Li and ^{8}B are undergoing a slow decay at this point, they are considered as background. Therefore, from 14 MeV upward, histograms are fitted using $N(T_e)$ and a polynomial function, setting the endpoint at 16.96 MeV. Once the best fit has been obtained, fitting parameters are substituted in the fitting function in order to extrapolate at low energies. The next endpoint is then selected to 13.6 MeV, and the process is repeated, to extract events from ^{9}Li and making sure the lower limit of the fitting interval stays bellow 10.6 MeV in order to avoid overlapping of fitting curves from different cases. The next fit is then performed with the upper limit and endpoint at 10.6 MeV to extract events from ^{8}He. Extrapolated fitting curves are presented in Figure 4.26 and Figure 4.27. The dotted red curve serves as background to the green curve (^{9}Li), which in turn serves as background to the continued red curve (^{8}He). After background subtraction, Fermi-Kurie plots are obtained for ^{8}He and ^{9}Li for t_{off}=1.2 s and t_{off}=5.2 s as shown by the graph on the upper right of Figure 4.26 and Figure 4.27 respectively.

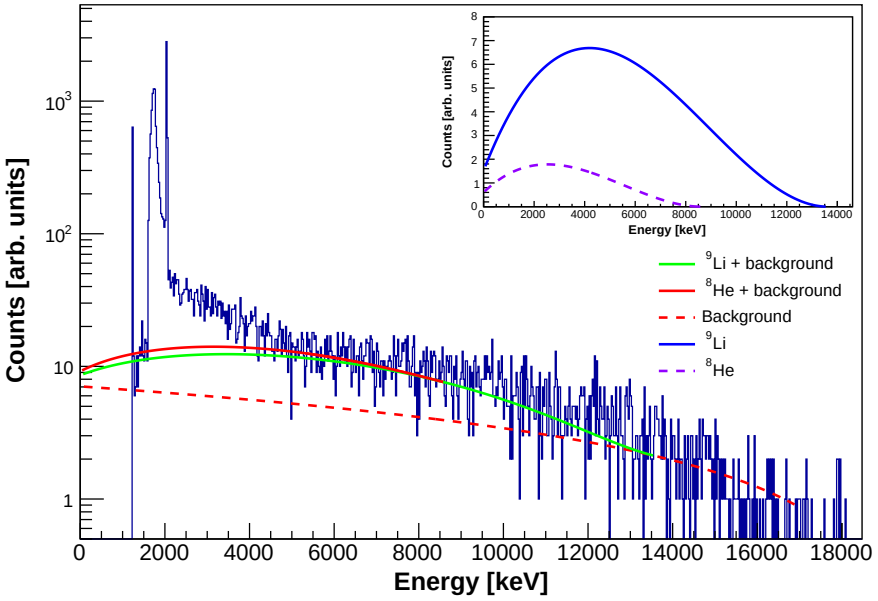

Figure 4.26: Electron energy spectrum of ^{8}He and ^{9}Li for t_{off}=1.2 s. The time gate is set for one half life of ^{9}Li (0.178 s). This is obtained for E_{lab}=50 MeV. The background is fitted using an association of the $N(T_e)$ function and a polynomial equation, with the endpoint at 16.96 MeV.

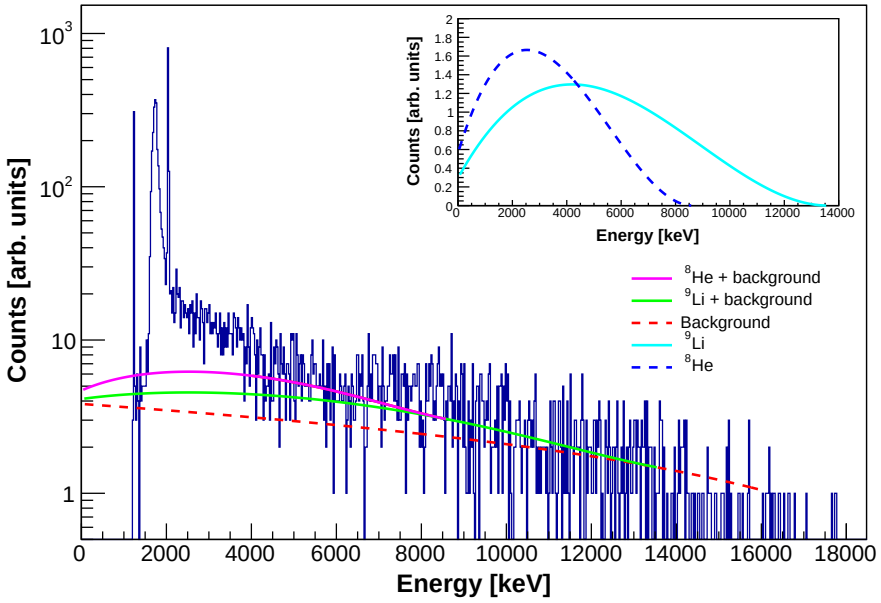

Figure 4.27: Electron energy spectrum of ^{8}He and ^{9}Li for t_{off}=5.2 s. The time gate is set for one half life of ^{9}Li (0.178 s). This is obtained for E_{lab}=66 MeV. The background is also fitted using the $N(T_e)$ function and a polynomial equation, with the endpoint at 16.96 MeV.

For nuclei with longer half lives, if the time gate is set after 0.5 s, electron energy spectra are presented in Figure 4.28 and Figure 4.29 for t_{off}=1.2 s and t_{off}=5.2 s respectively. As previously mentioned, the majority of β- particles detected during this interval of time are emitted either by ^{8}B or ^{8}Li. For short beam-off sequences events are obtained during less than one half life of the latter nuclei. For t_{off}=5.2 s, the time is long enough for any other nuclei produced in the reaction to be observed. To limit such contaminants, the time gate is set between 0.5 s and 1.4 s which is approximately one half life of ^{8}Li. Histograms are also fitted using $N(T_e)$. The background is fitted using a linear function. Since ^{8}B and ^{8}Li have neighbouring Q-values, the fit obtained by setting the endpoint to the largest Q-value, 16.96 MeV. The lower limit of the fit is set to any value greater than 14 MeV (and lower than the endpoint) until the best fit is obtained. This is to limit events with lower Q-values. The resulting function is extrapolated to lower energies. After fitting and background subtraction, the function is integrated from 0 to 16.96 MeV to extract N_t, the total number of ^{8}Li and ^{8}B to have decayed during the given amount of time, denoted $N_{^{8}Li}$ and $N_{^{8}B}$ respectively. N_t is defined by Equation 4.13.

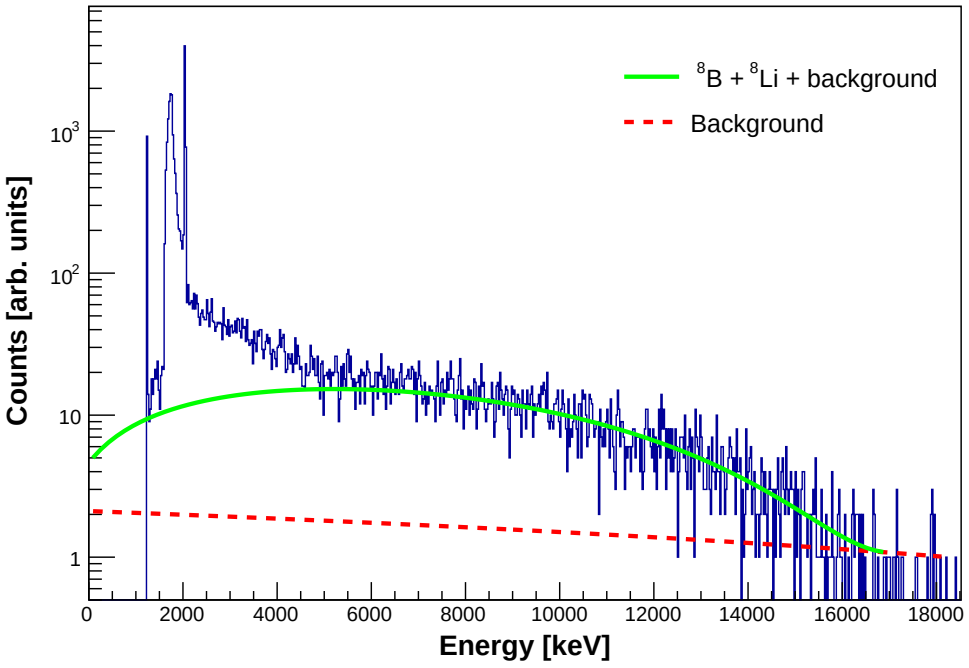

Figure 4.28: Electron energy spectrum of ^{8}B and ^{8}Li for a time gate set between 0.5 s and 1.2 s. This is obtained for E_{lab}=50 MeV.

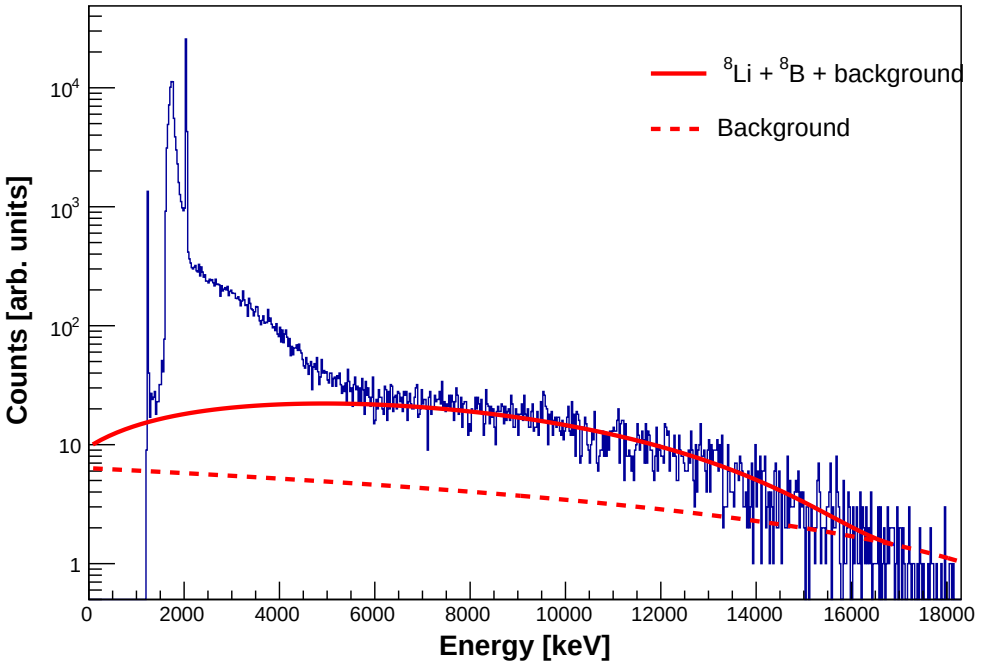

Figure 4.29: Electron energy spectrum of ^{8}B and ^{8}Li for a time gate set between 0.5 s and 1.4 s (about one half life of ^{8}Li). This is obtained for E_{lab}= 66 MeV. The bump observed below 5 MeV corresponds to other nuclei with low Q-values and half lives close to that of ^{8}Li.

Decay curves can be plotted in both cases by setting a gate on the energy. Therefore, histograms in Figure 4.30 and Figure 4.31 are obtained for energies between 14 MeV and 17 MeV (14 MeV is choosen in order to discard events from ^{8}He and ^{9}Li since the largest Q-value is 13.6 MeV). A procedure similar to what has been described in Section 4.7.2 is observed. The decay curves are fitted using Equation 4.12 (and a linear background) with fixed values of λ_1 and λ_2 corresponding to decay constants of ^{8}Li and ^{8}B respectively. The total number of ^{8}Li and ^{8}B nuclei to have decayed after the beam-off sequence for energies between 14 MeV and 17 MeV are extracted and denoted $N'_{s_{Li}}$ and N'_{s_B} respectively. Using Equation 4.13 and Equation 4.14, the total number of ^{8}Li and ^{8}B to have decay during the time taken into consideration are determined using Equation 4.15.

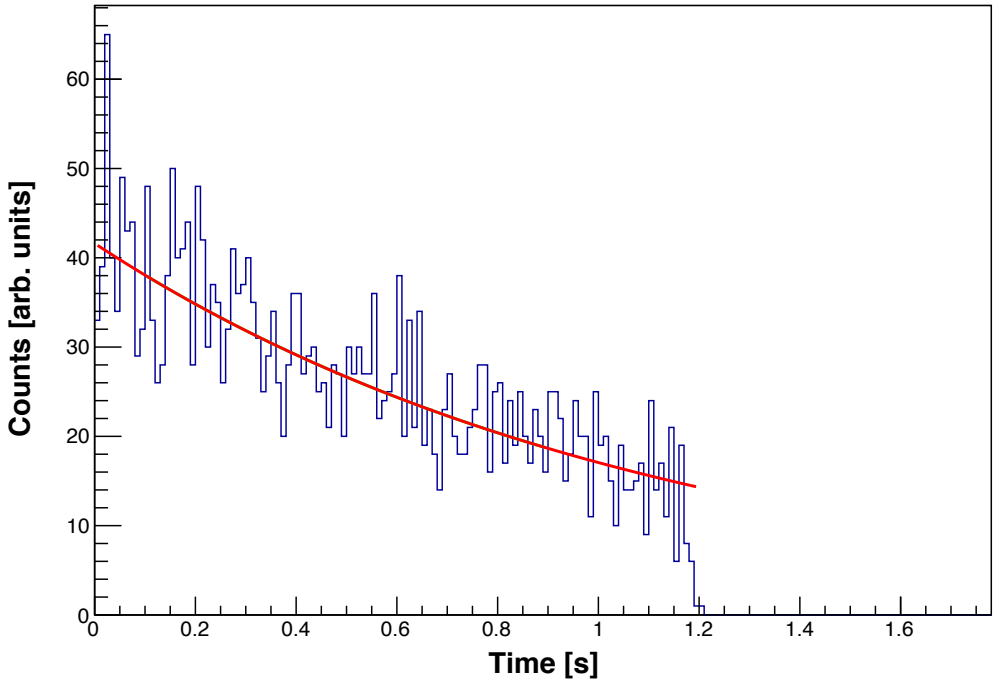

Figure 4.30: Decay curve of ^{8}B and ^{8}Li considered as a mixture, obtained for t_{off}=1.2 s at E_{lab}=50 MeV, with an energy gate from 14 MeV to 17 MeV. Here t_{off} is shorter than the half lives of ^{8}B and ^{8}Li.

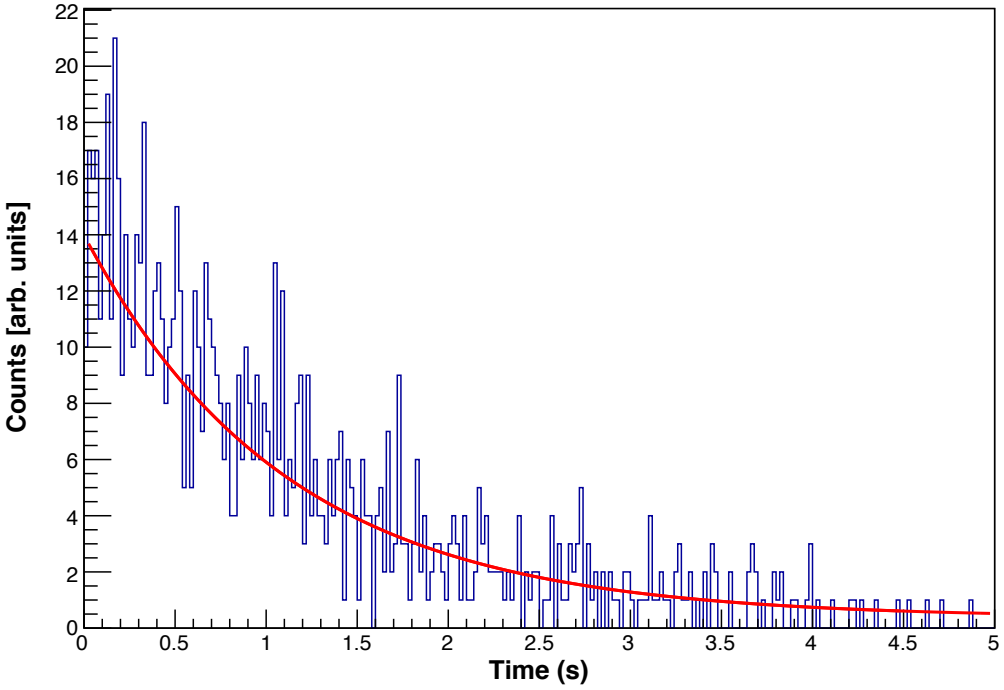

Figure 4.31: Decay curve of ^{8}B and ^{8}Li considered as a mixture, obtained for t_{off}=5.2 s at E_{lab}=66 MeV, with an energy gate from 14 MeV to 17 MeV. t_{off} corresponds to few half lives of ^{8}B and of ^{8}Li.

Fitting parameters obtained from the fit of all the Fermi-Kurie plots corresponding to the decay of products from ^{nat}B targets are presented in Table 4.6.

Table 4.6: Parameters obtained after fitting Fermi-Kurie plots for ^{8}Li and ^{8}B.

Beam energy	Product	χ^2/ndf	$C\|M_{if}\|$	κ
50 MeV	^{8}He	1.3461	$(1.7\pm0.2)\times10^{-17}$	$(2.4\pm2.1)\times10^{6}$
	^{9}Li	1.2829	$(1.3\pm0.8)\times10^{-16}$	$(1.3\pm0.24)\times10^{4}$
	^{8}Li + ^{8}B	1.3282	$(1.3\pm0.1)\times10^{-17}$	$(3.9\pm0.03)\times10^{6}$
66 MeV	^{8}He	0.9480	$(4.1\pm3.8)\times10^{-18}$	$(5.1\pm1.2)\times10^{5}$
	^{9}Li	0.6562	$(1.8\pm0.8)\times10^{-17}$	$(1.3\pm1.0)\times10^{5}$
	^{8}Li + ^{8}B	1.3952	$(9.2\pm0.2)\times10^{-18}$	$(2.3\pm0.6)\times10^{5}$

4.8 Summary

The aim in this chapter has been to present and discuss the data analysis process. The data sorting procedure was presented, as well as the energy calibration and the product identification. Furthermore, the coincidence measurement between LEPS and paddles revealed that reaction products were detected and could be identified. This led to the extraction of Fermi-Kurie plots for each exotic nuclei of interest. More aspects on the data analysis and the presentation of results will be detailed in the next chapter.

Chapter 5

Results

5.1 Overview

Production cross sections of exotic nuclei produced by proton induced reactions on ^{nat}Li, ^{9}Be and ^{nat}B targets are presented in this chapter. Experimental parameters such as beam characteristics, target dimensions and the number of products needed for the extraction of the cross section are also presented. Parameters obtained from fitting the Fermi-Kurie plots are used to determine the number of exotic nuclei produced in the reaction. The cross section is measured by observing the radiation growth of the daughter nuclei of ^{6}He, ^{8}He, ^{8}Li and ^{9}Li. The results obtained are compared to Talys calculations.

5.2 Error propagation

5.2.1 Systematic errors

Uncertainties on target measurements and detection instruments could contribute to systematic errors associated to the cross section. The uncertainty on the area density originates from the target thickness and weight, as well as the angle at which the target ladder is positioned in the scattering chamber. In addition, some uncertainties are registered in the energy loss calculation. Uncertainty in determining the stopping power using ESTAR-NIST are also evaluated. For incident electrons with energy above 100 keV the uncertainty of the collision stopping

power is estimated to 1% to 2% [45]. Also, the uncertainty associated with the radiation stopping power is 5% for energies below 50 MeV. Considering that the stopping power was calculated for electrons with incident energies up to 16 MeV, the total error on the energy loss is therefore approximated to 5%.

The efficiency of the detectors are also evaluated. Since electrons interact with every material they go through, the detection efficiency of the LEPS for electrons is considered to be 100%. Paddles are also consider to have an efficiency of 100% for electrons. Only the geometric factor (geometric efficiency) is taken into consideration. It is expressed as a function of the solid angle as follow:

$$\epsilon = \frac{\Omega}{4\pi} = \frac{1}{2}\left(1 - \frac{d}{\sqrt{d^2 + r^2}}\right), \tag{5.1}$$

with r and d representing the radius of the detector and the distance from target to detector respectively. The radius of the detector is obtained considering the active area of the LEPS. The target was placed at a distance of 8.5 cm from the detector.

5.2.2 Statistical errors

Statistical errors are associated with data manipulation. Two sets of data are fitted in this work. The first and larger set is the one containing information on the products of the reaction, that is the main experimental data. The second data set, a considerably smaller but rather important, is the signal from the current integrator used to determine the beam current. In both cases, the number of events needed is obtained by integrating the area delimited by the fitting curve (without the background). The error obtained when fitting Fermi-Kurie plots is determined using:

$$\delta N = \sqrt{\left(\frac{\partial N}{\partial p_0}\delta p_0\right)^2 + \left(\frac{\partial N}{\partial p_1}\delta p_1\right)^2}, \tag{5.2}$$

where

- $N = \int_0^Q N(T_e)dT_e$ is the integral of the function used to fit Fermi plots. In this integral, $C|M_{if}|^2$ and κ have respectively been substituted by fitting parameters p_0 and p_1.

- δN is the error associated with N. It is the error attributed to the number of products.
- δp_0 and δp_1 represent errors associated with fitting parameters p_0 and p_1 respectively.

5.3 Experimental parameters

5.3.1 Beam intensity

The beam current is measured using the Faraday cup. Particles from the beam are collected by the Faraday cup and measured using the current integrator. The current integrator is calibrated to a specific range depending on the expected beam current. The current integrator generates a pulse whenever the total charge exceeds the specified range. The histogrammed amplitude signal of the current integrator is shown in Figure 5.1, representing the total number of pulses generated by the current integrator during a run. For this measurement, the range of the current integrator was set to 2 nA. The beam intensity (or beam flux) is obtained by dividing the beam current by the charge of particles constituting the beam, that is 1.6×10^{-19} for protons (that is the charge e of an electron).

Let the range of the current integrator be denoted by k and the number of pulses generated by the current integrator N_{CI}. The beam intensity is expressed as followed [46]

$$I = \frac{N_{CI}.k}{1000.e}\,. \tag{5.3}$$

N_{CI} is obtained by calculating the area of the peak represented on the spectrum. Here, 1000 accounts for the pulse rate of the current integrator (1 kHz). It should be noted that the value of N_{CI} obtained in this manner corresponds to events detected during a run. Since the beam is turned on and off for many cycles during a run, particles are only collected during certain time intervals corresponding to beam-on sequences. Equation 5.3 is therefore corrected for the time as follow

$$I = \frac{N_{CI}\cdot t_{on}\cdot k}{1000\cdot t_{CI}\cdot e}\,, \tag{5.4}$$

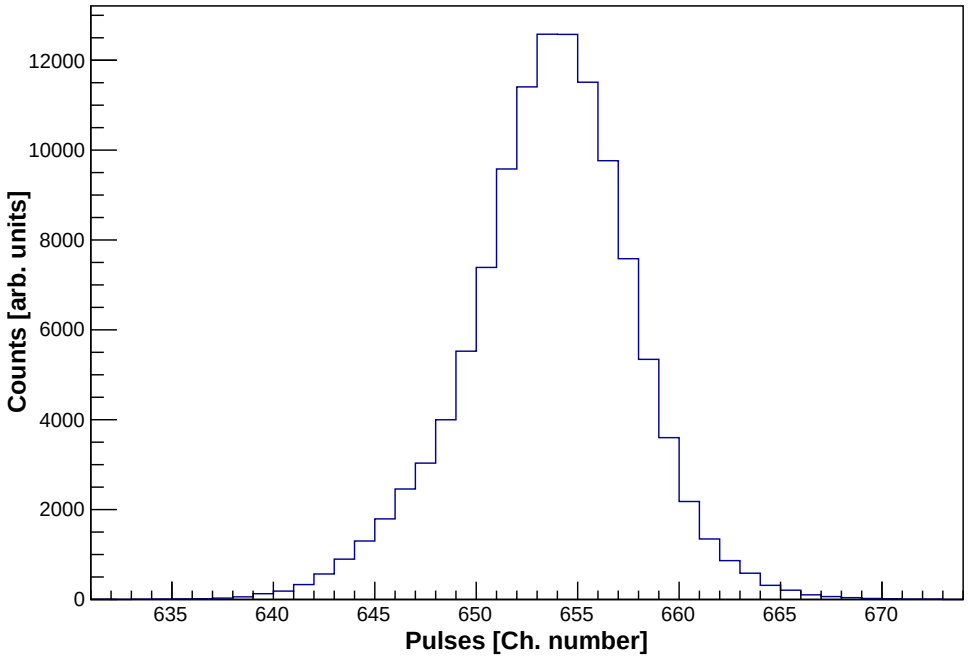

Figure 5.1: Pulses generated by the current integrator

where t_{on} is the duration of a beam-on sequence and t_{CI} is the time during which the current integrator is generating pulses, corresponding to the duration of a run.

Beam intensities measured for each target at different beam energy are listed in Table 5.1. Equation 5.4 is used to determine the beam intensity for one run. For a target with data in several runs, the expression of the beam flux becomes

$$I = \frac{t_{on} \cdot k}{1000 \cdot e} \sum_i \frac{(N_{CI})_i}{(t_{CI})_i} \,, \tag{5.5}$$

where $(N_{CI})_i$ and $(t_{CI})_i$ are respectively the generated number of pulses and the measurement time of the current integrator for the i^{th} run.

Table 5.1: Beam intensity recorded during measurements with each target.

	50 MeV		66 MeV	
Target	I [s^{-1}]	δI [s^{-1}]	I [s^{-1}]	δI [s^{-1}]
^{nat}Li	6.74×10^{9}	2.62×10^{7}	5.50×10^{9}	2.66×10^{7}
^{9}Be	6.28×10^{9}	3.95×10^{7}	5.05×10^{9}	2.45×10^{7}
^{nat}B	5.91×10^{9}	1.6×10^{7}	5.72×10^{9}	1.88×10^{7}

5.3.2 Target area density

The target area density n is the number of nuclei per unit area (cm^2). Target area densities listed in Table 5.2 are calculated using the following equation:

$$n = \frac{d \cdot N_A}{M \cdot cos\theta} \tag{5.6}$$

where

- d is the density thickness of the target (g.cm^{-2}),
- M is the molar mass (g.mol^{-1}),
- N_A is Avogadro's number (mol^{-1}),
- θ is the angle between the beam direction and the normal to the target.

Table 5.2: Target area densities

Target	n [nuclei/cm^2]	δn [nuclei/cm^2]
^{nat}Li	1.88×10^{22}	1.02×10^{21}
^{9}Be	2.70×10^{21}	9.98×10^{20}
^{nat}B	2.74×10^{21}	2.14×10^{20}

5.3.3 Decay rate

Parameters obtained from the fit of the Fermi-Kurie plot are substituted in the expression of $N(T_e)$. The resulting function is integrated to obtain the number of

electrons emitted during the decay of unstable products. This number is equal to the number of daughter nuclei present in the reaction at the end of the beam-off sequence. The production rate of the daughter nuclei is at all time dependent of the decay rate of the parent. Since ^{6,8}He, ^{8,9}Li decay, knowing the production rate of their daughter nuclei will inform on their decay rate, hence their cross section. For a stable daughter nucleus, the production rate is

$$R = \frac{\lambda \cdot N}{N_c \cdot \epsilon} \,, \tag{5.7}$$

where

- N is the number of daughter nuclei, corresponding to the number of electrons obtained from the Fermi plot,
- N_c is the number of beam on-off cycles in a run,
- λ is the decay constant of the parent nuclei, that is the exotic product and
- ϵ is the detection efficiency.

Values of decay rates for products corresponding to each target are presented in Table 5.3. These values are listed for each proton beam energy.

Table 5.3: Decay rate R obtained from the number of nuclei extracted after fitting Fermi-Kurie plots.

		R [s^{-1}]	
Target	Product	50 MeV	66 MeV
^{nat}Li	^{6}He	$(1.09 \pm 0.07)\times10^{5}$	$(1.07 \pm 0.03)\times10^{5}$
^{9}Be	^{8}Li	$(1.02 \pm 0.22)\times10^{5}$	$(5.89 \pm 0.56)\times10^{4}$
	^{8}B	$(2.86 \pm 1.65)\times10^{4}$	$(9.85 \pm 2.90)\times10^{3}$
^{nat}B	^{8}He	$(2.44 \pm 0.34)\times10^{1}$	$(1.38 \pm 0.73)\times10^{3}$
	^{8}Li	$(9.63 \pm 2.56)\times10^{3}$	$(3.39 \pm 1.95)\times10^{4}$
	^{9}Li	$(2.92 \pm 0.57)\times10^{2}$	$(1.56 \pm 0.51\ )\times10^{3}$
	^{8}B	$(5.49 \pm 3.33)\times10^{3}$	$(1.68 \pm 0.47)\times10^{4}$

5.4 Cross section

The production cross section of a radioactive nucleus is obtained by studying the radiation growth of the daughter nuclei. A relationship is established in Section 2.3.2 between the production rate of an unstable decaying nucleus and the production rate of its daughter nucleus. The production rate of the parent nuclei is $w = \sigma n I$, which is a function of the cross section, the beam intensity and the target density. During the measurement, different beam on-off cycles were set depending on targets and products. It is therefore suitable to evaluate the cross section accordingly. The number of nuclei changes with time, resulting to the total activity adopting different behaviours depending on the half life and the duration of the beam on-off sequence.

5.4.1 Lithium target

The case of ^{6}He produced from ^{nat}Li is quite straightforward in the sense that it is the only product of ^{nat}Li undergoing a β-decay. Furthermore, ^{6}He decays into only one stable nucleus, ^{6}Li. For both beam energies (50 MeV and 66 MeV), t_{on} was set to 4.8 s and t_{off} to 5.2 s. The half life of ^{6}He is 0.807 s, which is about six times smaller than t_{on}. Following what has been presented in Section 2.3.2 and substituting w by its expression, the production rate of ^{6}He at the end of a beam cycle is obtained using Equation 2.18. Since $t_{on} \gg 0.807$ s, the number of ^{6}He reaches saturation (secular equilibrium) before the end of the beam-on sequence. The decay rate, $R_{^{6}He}$, is expressed considering the maximum number of ^{6}He obtained when the beam is turned off (which is also its initial number at the beginning of the beam-off sequence) and corresponds to the initial activity of ^{6}He.

$$R_{^{6}He} = \sigma n I \tag{5.8}$$

During this sequence, the only activity is that of the decay of ^{6}He, that is

$$A_{^{6}He}(t) = \sigma n I e^{-\lambda t_{off}} \tag{5.9}$$

In Chapter 4, Figure 4.19 was obtained by considering a time limit equal to one half life. Therefore, for one half life, the production cross section of ^{6}He is expressed as follows:

$$\sigma = \frac{2 \cdot A_{^{6}He}(t_{1/2})}{n \cdot I}, \tag{5.10}$$

where $R_{^{6}He}$, n and I are the decay rate of ^{6}He, the number density of the ^{nat}Li target and the beam intensity respectively.

5.4.2 Beryllium target

A situation similar to that observed in the case of ^{6}He is reproduced here, with ^{8}Li being the only product of interest. Since the production of ^{8}B is rather significant in the p+^{9}Be reaction, it was also taken into consideration. Beam cycles are set in a similar manner as well, that is $t_{on} = 4.8$ s and $t_{off} = 5.2$ s. The half lives of ^{8}Li and ^{8}B are 0.84 s and 0.77 s respectively; which are also shorter than t_{on}. The decay rate was determined for an interval of time equal to one half life of ^{8}Li. Thus, the production cross section of ^{8}Li is expressed by

$$\sigma = \frac{2 \cdot A_{^{8}Li}(t_{1/2})}{n \cdot I} \tag{5.11}$$

with $A_{^{8}Li}(t_{1/2})$, n and I being the decay rate of ^{8}Li during one half life of ^{8}Li, the number density of the ^{9}Be target and the beam intensity respectively. The cross section of ^{8}B is determined as follow:

$$\sigma = \frac{A_{^{8}B}(t_{1/2}(^{8}Li))}{n \cdot I \cdot e^{-\lambda_{^{8}B} t_{1/2}(^{8}Li)}} \approx \frac{2 \cdot A_{^{8}B}(t_{1/2}(^{8}Li))}{n \cdot I}, \tag{5.12}$$

where $A_{^{8}B}(t_{1/2}(^{8}Li))$ is the decay rate of ^{8}B during one half life of ^{8}Li and $\lambda_{^{8}B}$ its decay constant.

5.4.3 Boron target

For ^{nat}B target, products are ^{8}He, ^{8}Li, ^{9}Li and ^{8}B with half lives 0.119 s, 0.840 s, 0.178 s and 0.770 s respectively. The various reactions are summarised in

Figure 5.2 where σ_i, i=1, 2, 3, 4, are the production cross sections of ^{8}B, ^{8}He, ^{8}Li and ^{9}Li respectively, and λ_i, i=1, 2, 3, 4, their respective decay constants. In order to adequately determine the decay rate of each product, beam cycles were set long enough to allow each nucleus to decay during at least six times their half lives. In this respect, cycles were set to t_{on} = 0.8 s and t_{off} = 1.2 s; t_{on} = 1.2 s and t_{off} = 0.8 s and later on to t_{on} = 4.8 s and t_{off} = 5.2 s.

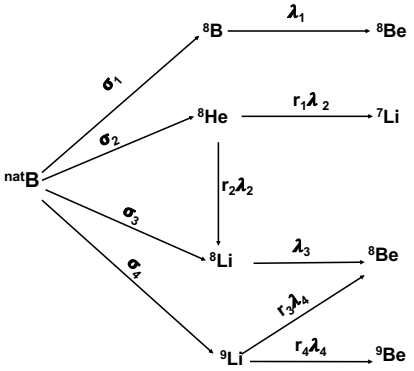

Figure 5.2: Schematic representation of the reaction channels of interest taking place for p+^{nat}B.

During the decay of ^{8}He, two main decay branches are observed. The first branch leads to the formation of ^{8}Li (83%) with a decay constant of $r_2\lambda_2$. The second branch corresponds to a decay constant of $r_1\lambda_2$ and leads to the production of ^{7}Li (16%). r_1 and r_2 are the branching ratios. A similar situation is observed during the decay of ^{9}Li with the branching ratio denoted r_3 for the decay into ^{8}Be (50.8%) and r_4 for ^{9}Be (49%). The production cross section can be determined using either decay branches. However, fits performed on electron energy spectra were used to determine the total number of electrons emitted during the decay ^{8}He and ^{9}Li, that is taking into account all decay branches. Furthermore, the decay rates of ^{8}He and ^{9}Li were obtained for a time interval equal to one half life of ^{9}Li. Given their short half lives, at the end of t_{on}, the production rate of ^{8}He and ^{9}Li is at maximum, that is ω/λ. Therefore, the production cross section of ^{9}Li is determined using

$$\sigma_4 = \frac{2 \cdot A_{^9Li}(t_{1/2}(^9Li))}{n \cdot I}. \tag{5.13}$$

On the other hand, the production cross section of ^{8}He is expressed by:

$$\sigma_2 = \frac{A_{^8He}(t_{1/2}(^9Li))}{n \cdot I \cdot e^{-\lambda_2 t_{1/2}(^9Li)}}. \tag{5.14}$$

$A_{^9Li}(t_{1/2}(^9Li))$ and $A_{^8He}(t_{1/2}(^9Li))$ are respectively the decay rates of ^{9}Li and ^{8}He for a half life of ^9Li. The parameter n represents the number density of the ^{nat}B target and I the beam intensity.

For nuclei with longer half lives, that is ^{8}B and ^{8}Li, an irradiation time of 0.8 s or 1.2 s corresponds to one or less than twice the half life. For this case, the time gate was set between 0.5 s and t_{off}. The production cross section σ_1 of ^{8}B was obtained using

$$\sigma_1 = \frac{A_{^8B}(t_{off} - 0.5)}{n{\cdot}I{\cdot}(1 - e^{-\lambda_1 t_{on}}){\cdot}e^{-\lambda_1(t_{off}-0.5)}}. \tag{5.15}$$

The production of ^{8}Li is controlled by two sources. Firstly the primary reaction p+^{nat}B and secondly the decay of ^{8}He. Given that the half life of ^{8}He is very small as compared to the half life of ^{8}Li, for t_{on}= 0.8 s, the cross section of the total production of ^{8}Li is

$$\sigma_3 = \frac{A_{^8Li}(t_{off})}{n{\cdot}I{\cdot}(1 - e^{-\lambda_3 t_{on}}){\cdot}e^{-\lambda_3 t_{off}}} - r_2\sigma_2(t_{off}). \tag{5.16}$$

$\sigma_2(t_{off})$ is the cross section of ^{8}He obtained using a decay rate corresponding to a time t_{off}.

For t_{on}= 4.8 s and t_{off} = 5.2 s, the observation time is one half life of ^{8}Li. The production cross sections of ^{8}B and ^{8}Li are expressed as follow:

$$\sigma_1 = \frac{A_{^8B}(t_{1/2}(^8Li)}{n{\cdot}I{\cdot}e^{-\lambda_2 t_{1/2}(^8Li)}} \approx \frac{2{\cdot}A_{^8B}(t_{1/2}(^8Li))}{n{\cdot}I} \tag{5.17}$$

and

$$\sigma_3 = \frac{2{\cdot}A_{^8Li}(t_{1/2}(^8Li))}{n{\cdot}I} - r_2\sigma_2(t_{1/2}(^8Li)). \tag{5.18}$$

Here, $\sigma_2(t_{1/2}(^8Li))$ is the cross section of ^{8}He obtained using a decay rate corresponding to a half life of ^{8}Li.

5.4.4 Results

The analysis of the radiation growth of exotic nuclei of interest resulted in obtaining formulae, used in each case to determine results for the production cross section, presented in Table 5.4 and Table 5.5. These results are presented for a proton beam energy of 50 MeV and 66 MeV respectively. They are compared to those calculated using Talys. Natural lithium is composed of ^{7}Li and ^{6}Li in

ratios of 90.4% and 7.6%. Natural boron is made of 80% of ^{11}B and 20% of ^{10}B respectively.

Table 5.4: Cross section at 50 MeV

		σ [mb]	
Target	Product	measured	Talys
^{nat}Li	^{6}He	1.72±0.15	2.27
^{9}Be	^{8}Li	12.10±5.14	12.73
	^{8}B	3.93±2.79	2.08
^{nat}B	^{8}He	$(2.33\pm0.7)\times10^{-3}$	2.89×10^{-3}
	^{8}Li	2.40±0.66	2.10
	^{9}Li	$(3.6\pm1.10)\times10^{-2}$	9.54×10^{-2}
	^{8}B	1.38 ±0.85	1.19

Table 5.5: Cross section at 66 MeV

		σ [mb]	
Target	Product	measured	Talys
^{nat}Li	^{6}He	2.06±0.13	1.50
^{9}Be	^{8}Li	8.64±3.30	6.93
	^{8}B	1.54± 0.73	0.83
^{nat}B	^{8}He	0.14±0.07	7.78×10^{-2}
	^{8}Li	4.22±0.72	5.10
	^{9}Li	0.20±0.07	0.18
	^{8}B	2.29±0.66	1.88

It can be observed that measured results are in agreement with Talys calculations. Same values are plotted in Figure 5.3 and Figure 5.4.

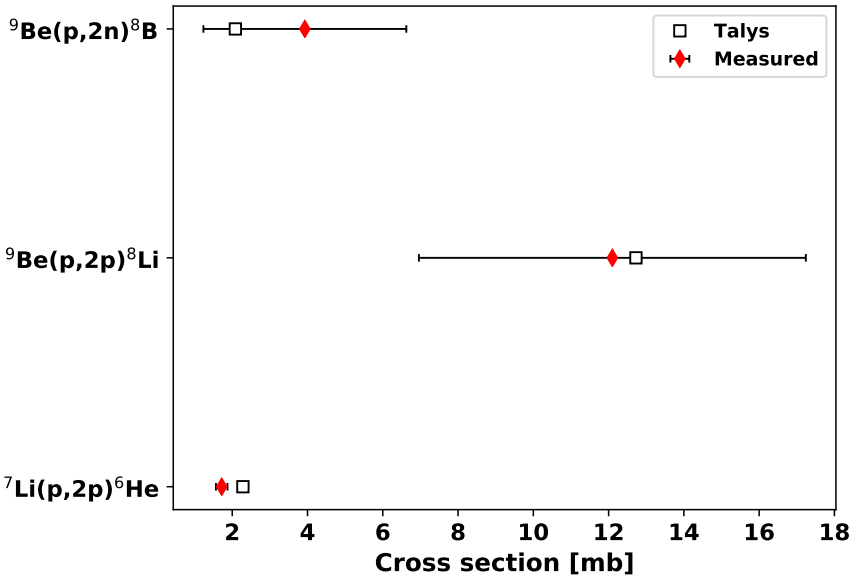

(a)

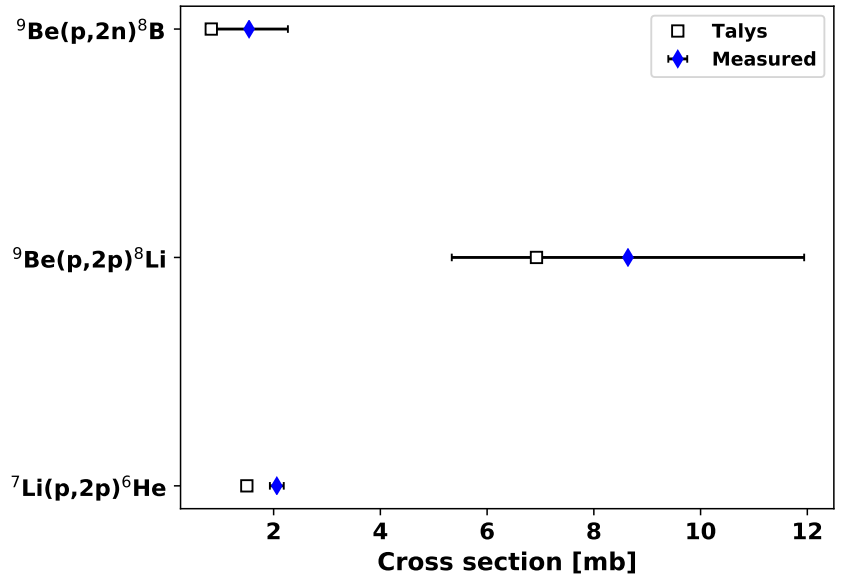

(b)

Figure 5.3: Production cross section of ^{6}He, ^{8}Li and ^{8}B, produced from p+^{nat}Li and p+^{9}Be, compared to Talys calculations. These values are presented for E_{lab}= 50 MeV (a) and for E_{lab}= 66 MeV (b).

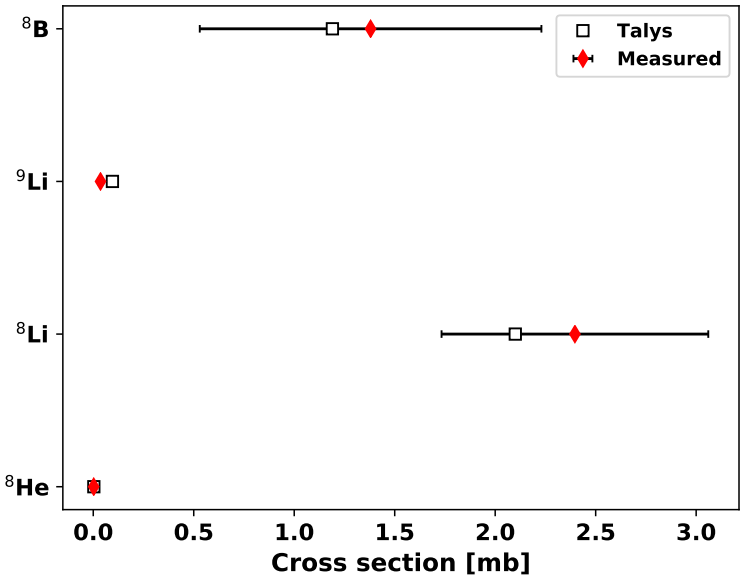

(a)

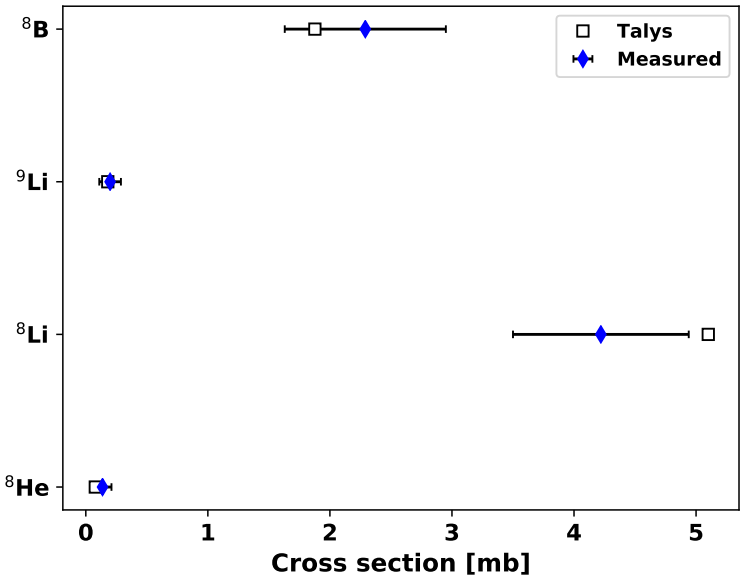

(b)

Figure 5.4: Production cross section of ^{8}He, ^{8}Li, ^{9}Li and ^{8}B, produced from p+^{nat}B, compared to Talys calculations. These values are presented for E_{lab}= 50 MeV (a) and for E_{lab}= 66 MeV (b).

5.5 Summary

Values of all experimental parameters were presented in this chapter. This included the beam intensity, the target density and the production rate (decay rate of product). The latter was determined using the number of electrons (or positrons), previously obtained from fits performed on Fermi-Kurie plots. Measured values of the production cross section were compared to values calculated using Talys. Even though ^{8}B was not initially listed among nuclei of interest, its abundance and the difficulty to dissociate the number of β-particles emitted from its decay from those emitted from the decay of ^{8}Li made it necessary to include its production cross section to the results.

Chapter 6

Summary and conclusion

The main objective in this study has been to measure the production cross section of ^{6,8}He and ^{8,9}Li using targets of ^{nat}Li, ^{9}Be and ^{nat}B, bombarded by a proton beam of energy 50 MeV and 66 MeV. This has been achieved using a ΔE-E telescope made of a 5 mm plastic scintillator detector for energy loss assessment, and a LEPS detector for residual energy measurement. Results obtained from this method after analysis revealed some agreement with calculations performed using Talys.

The idea behind the study of the production of light exotic nuclei using light stable nuclei was motivated by the development of the SAIF project to be implemented at iThemba LABS. In this regard, the study was developed in order to perform a feasibility check on the production of light radioactive beams using the ISOL method. Light stable nuclei have less products than heavier nuclei in a proton induced reaction. The use of such nuclei as targets in the ISOL method would offer easier conditions for development of radioactive beam extraction and separation.

Measurements were conducted at iThemba LABS. A brief overview of the facility has been presented, as well as a detailed display of the experimental setup. A ΔE-E telescope composed of a plastic scintillator detector (paddle) and a LEPS detector was used for particle detection. The paddle was designed, built and tested in the lab, and was used for energy loss measurement, whereas the LEPS detector was employed for residual energy measurement. The ΔE-E technique obtained with such settings ensured a particle identification, with high energy

resolution and detection efficiency. The telescope was used to detect electrons emitted from the decay of products of primary reactions.

The total energy loss was evaluated taking into account all residual energies lost by electrons in every media along their trajectory, before their interaction with the LEPS' crystal. The total energy of β-particles emitted from the decay of products was obtained by writing its expression as a function of the residual energy measured by the LEPS. Electron energy spectra obtained in this manner followed the precise distribution of the Fermi-Kurie plot describing the β-decay process. All neutron-rich nuclei of interest could therefore be identified by locating the endpoint of the Fermi-Kurie plot, corresponding to their decay Q-values.

Electron energy spectra were fitted using the expression defining the number of electrons as a function of the kinetic energy of electrons and describing the Fermi-Kurie plot. As a result, the decay rate of each product was determined for each given reaction. The cross section was then deduced by analysing the radiation growth of each product for each reaction. It was observed during the analysis that ^{8}B was significantly present in p+^{9}Be and p+^{nat}B reactions. Given its exotic nature, its production cross section was included in the results.

Given the insufficient availability of similar studies, results were compared to calculated values from Talys. As previously discussed, the comparison of results led in most cases to a satisfactory conclusion, strengthening the opinion of the reliability and precision of the technique used for the measurement and the analysis.

Facilities worldwide are focusing their interest in the production of exotic beams, among which ^{6}He is one of the least produced. The current available intensities are in the order of 10^{8} to 10^{9} atoms/s. Studies using such beams are limited, given that most interest are oriented towards more exotic nuclei. The production of a ^{6}He beam with intensity reaching a nA or more, could offer a wide range of applications in nuclear structure studies. For instance, neutron pairing can be studied by considering a (^{6}He, α) reaction, used to populate two-neutron states in a target nucleus. Furthermore, the availability of intense light exotic beams could have implications in other nuclear physics areas, such as cluster and halo formation, low density nuclear matter interactions and more.

The radioactive beam facility (SAIF project) to be implemented at iThemba LABS will require a driver beam from the SSC, at 66 MeV that can supply up

to 200 μA. With production cross sections obtained for proton beam energies of 50 MeV and 66 MeV, an extrapolation can be performed in order to estimate the production cross section for different target thicknesses. Considering for instance a boron target thick enough to degrade the proton beam energy from 66 MeV to 40 MeV, knowing the cross section distribution in the target and the beam intensity (200 μA for instance), the number of atoms of interest produced in the target can be estimated. Such reasoning can be applied using lithium and beryllium targets, to determine the total number of produced atoms. Estimated values of the number of products of interest, produced in different targets are listed in Table 6.1 .

Table 6.1: Production rate (N) of nuclei of interest in different targets. These estimations are obtained considering a target thickness necessary to slow down a 66 MeV proton beam to 40 MeV for a beam current of 200 μA.

Target	Thickness [cm]	Product	σ [mb]	N [atoms/s]
^{nat}Li	37.12	^{6}He	116.80	1.58×10^{14}
^{9}Be	1.38	^{8}Li	0.36	7.91×10^{10}
		^{8}B	0.078	1.30×10^{10}
^{nat}B	1.84	^{8}He	0.077	2.18×10^{9}
		^{8}Li	0.54	1.63×10^{11}
		^{9}Li	0.021	3.96×10^{9}
		^{8}B	0.29	6.89×10^{10}

Targets have to be made in a specific manner in order to sustain such intensities. More work is therefore needed to ascertain the possibility of producing targets to be used in this regard. In addition, extraction and transmission techniques need to be implemented.

Appendix A

TALYS input files

TALYS input files used to calculate cross sections are presented as followed for p+^{nat}Li and p+^{9}Be reactions. Calculation obtained for ^{nat}B target are performed using an input file similar to that of ^{nat}Li.

- ^{nat}Li

```
projectile p
element Li
mass 0
energy 50
filechannels y # write exclusive channel cross sections on
    separate files
filetotal y    # write total cross sections on a separate file
fileresidual y # write residual production cross sections on a
    separate file
```

- ^{9}Be

```
projectile p
element Be
mass 9
energy 50
filechannels y
filetotal y
fileresidual y
```

Appendix B

SimSort

B.1 SortPR248.C

This is the main code. It calls *SimSort.cxx* and the *.cal* files. The data file to be read is specified, as well as the root file where events of interest will be written.

```
#include "TROOT.h"
Int_t SortPR248(){
        gROOT->LoadMacro("SimSort.cxx+");
        SimSort  data;
        data.Input("PR248/Sort.g.sims");
data.SetGroup(2);
        data.SetDetector("PR248/cal/group2/detector.cal");
        data.SetLookup("PR248/cal/group2/lookup.cal");
        data.SetOffset("PR248/cal/group2/offset.cal");
        data.SetGain("PR248/cal/group2/gain.cal");
char run_name[128];
char root_name[128];
for(Int_t j=0;j<1;j++){
        sprintf(run_name,"/Data/R12",j);
        sprintf(root_name,"trees/R12.root",j);
        data.DataTreeW(run_name,root_name,0);
}
  return 1;
}
```

B.2 *.sims* files

```
analysis
format
101
timestamp
10.00    500.
//skipblock
//4000
nbblock
1000
noaxis
elab
24.0
projectile
3 2
target
59 27    1000. 0.
breakup
62 29
particles //Type of emitted particles
1      SiSi        SiCsI
0 0          no      no  //0 0 for gamma, 1 1 for charged particles, 1 0
    for neutron
//swapdet
//3
intermediate
1
1 2
exit
1
62 29
61 29
noaddback
nofixevent
//noprojections
//notrees
modulo    //Used for beam on of selection
210818286. 2762960000. //see SimSort.cxx
end
```

B.3 SimSort.cxx

```
using std::cout;
using std::endl;

void SimSort::Init()
{
    Int_t i;
    for(i=0;i<=nbpartot;i++) dejavu[i]=0;
    for(i=0;i<4;i++)   mismom[i]=0;
    for(i=1;i<=nbpartot;i++){

    }
    for(i=0;i<nbcont;i++) ETOT[i] = 0 ;
    runb= 0 ;
    eventree= 0 ;
    contig  = 0 ;
    // for simulation
    effrec = 0 ;
    thetarec = 0 ;
    effbkp = 0 ;
    thetabkp = 0 ;
    exit = 0;
    info=0;
    Exr = 0;
    Exb = 0;
}

void SimSort::DataTreeW(Char_t *dataf, Char_t *rootf, Int_t cxxblock) {
    Int_t exitnb,trigger;
    Config(); // to read everything which is needed to run this program
    Int_t i,j,k,l,ii,itemp,itemp2;
    Int_t events;
    sumacos=0;
    ADC_events=0;
    postpone=0;
    words3=0;
    history[4000]=0;
    for(i=0;i<16;i++) empful[i]=0;
    gefficiency[0]=0;
    gefficiency[1]=0;
    if(projections>0){
        for(i=0;i<256;i++) for (ii=0;ii<8192;ii++) MDirect[i][ii]=0;
    }
    char treetype[2][128];
    char datatree[128]="DataTree";
    char simutree[128]="SimuTree";
    char cmd[128],ext[8];
    char c_gz[4]=".gz";

    for(i=0;i<128;i++){
        treetype[0][i]=datatree[i];
        treetype[1][i]=simutree[i];
    }
```

```
    Int_t nbi=0;
    Int_t ityp=0;
    counter = 0.;
    if(cxxblock>0) {
        nbblock=cxxblock;
        if(nbblock>10000) stepblock=10000;
        else stepblock=nbblock/2;
        cout << "  nbblock reinitialised: " << nbblock << endl;
    }
    TString rootif = rootf;
    TString dataof = dataf;
    statfs.open("infotree.txt",ios::out);

    // generates a set of calibration file for each group if needed
    if(fInput    == 0) Input("default/sims/Simu.6Li7Li.sims");
    if(fGain     == 0) SetGain("default/cal/gain.cal");
    if(fOffset   == 0) SetOffset("default/cal/offset.cal");
    if(fPosition == 0) SetPosition("default/cal/position.cal");
    if(fLookup   == 0) SetLookup("default/cal/lookup.cal");
    if(fThickq   == 0) SetThick("default/cal/thickness.cal");

    // increment the runnb
    runnb++;
    zip[runnb]=sprintf(dataf,dataf);
    ii=0;
    for(i=0;i<4;i++) ext[i]='\0';
    for(i=zip[runnb]-3;i<zip[runnb];i++) {
        ext[ii]=dataf[i];
        ii++;
    }
    if (! strcmp(ext,c_gz)) zip[runnb]=1;
    else zip[runnb]=0;

    TFile *f1=new TFile(rootif.Data(),"RECREATE");
    if(Datar==1) ityp=0;
    if(Simur==1) ityp=1;
    TTree *t1=new TTree(treetype[ityp],"Simulated Data");

    nbpartree=nbpartot-nbpart+1;
    nbpartree=nbpartot+1;
    t1->Branch("nbpartree", &nbpartree, "nbpartree/I"    );
    t1->Branch("mismom",mismom,"mismom[4]/D");
if(reduce<4){
t1->Branch("spare",    spare,    "spare[nbpartree]/D");
if(nbpartree >1) t1->Branch("beta1",beta1,"beta1[nbpartree]/D");
if(nbpartree >1) t1->Branch("beta2",beta2,"beta2[nbpartree]/D");
if(nbpartree >1) t1->Branch("beta3",beta3,"beta3[nbpartree]/D");
if(nbpartree >1) t1->Branch("beta4",beta4,"beta4[nbpartree]/D");
if(nbpartot >1) t1->Branch("erel1",erel1,"erel1[nbpartree]/D");
if(nbpartot >2) t1->Branch("erel2",erel2,"erel2[nbpartree]/D");
if(nbpartot >3) t1->Branch("erel3",erel3,"erel3[nbpartree]/D");
if(nbpartot >4) t1->Branch("erel4",erel4,"erel4[nbpartree]/D");
if(nbpartot >5) t1->Branch("erel5",erel5,"erel5[nbpartree]/D");
if(nbpartot >6) t1->Branch("erel6",erel6,"erel6[nbpartree]/D");
if(nbpartot >7) t1->Branch("erel7",erel7,"erel7[nbpartree]/D");
```

```
if(nbpartot >8) t1->Branch("erel8",erel8,"erel8[nbpartree]/D");
if(nbpartot >9) t1->Branch("erel9",erel9,"erel9[nbpartree]/D");
if(nbpartot >10) t1->Branch("erel10",erel10,"erel10[nbpartree]/D");
if(nbpartot >11) t1->Branch("erel11",erel11,"erel11[nbpartree]/D");
if(nbpartot >12) t1->Branch("erel12",erel12,"erel12[nbpartree]/D");
if(nbpartot >13) t1->Branch("erel13",erel13,"erel13[nbpartree]/D");
if(nbpartot >14) t1->Branch("erel14",erel14,"erel14[nbpartree]/D");
if(nbpartot >15) t1->Branch("erel15",erel15,"erel15[nbpartree]/D");
if(nbpartot >16) t1->Branch("erel16",erel16,"erel16[nbpartree]/D");
if(nbpartot >17) t1->Branch("erel17",erel17,"erel17[nbpartree]/D");
if(nbpartot >18) t1->Branch("erel18",erel18,"erel18[nbpartree]/D");
if(nbpartot >19) t1->Branch("erel19",erel19,"erel19[nbpartree]/D");
if(nbpartot >1) t1->Branch("Beta1",Beta1,"Beta1[nbpartree]/D");
if(nbpartot >2) t1->Branch("Beta2",Beta2,"Beta2[nbpartree]/D");
if(nbpartot >3) t1->Branch("Beta3",Beta3,"Beta3[nbpartree]/D");
if(nbpartot >4) t1->Branch("Beta4",Beta4,"Beta4[nbpartree]/D");
if(nbpartot >5) t1->Branch("Beta5",Beta5,"Beta5[nbpartree]/D");
if(nbpartot >6) t1->Branch("Beta6",Beta6,"Beta6[nbpartree]/D");
if(nbpartot >7) t1->Branch("Beta7",Beta7,"Beta7[nbpartree]/D");
if(nbpartot >8) t1->Branch("Beta8",Beta8,"Beta8[nbpartree]/D");
if(nbpartot >9) t1->Branch("Beta9",Beta9,"Beta9[nbpartree]/D");
if(nbpartot >10) t1->Branch("Beta10",Beta10,"Beta10[nbpartree]/D");
if(nbpartot >11) t1->Branch("Beta11",Beta11,"Beta11[nbpartree]/D");
if(nbpartot >12) t1->Branch("Beta12",Beta12,"Beta12[nbpartree]/D");
if(nbpartot >13) t1->Branch("Beta13",Beta13,"Beta13[nbpartree]/D");
if(nbpartot >14) t1->Branch("Beta14",Beta14,"Beta14[nbpartree]/D");
if(nbpartot >15) t1->Branch("Beta15",Beta15,"Beta15[nbpartree]/D");
if(nbpartot >16) t1->Branch("Beta16",Beta16,"Beta16[nbpartree]/D");
if(nbpartot>20) cout <<" Not enough ereln[], declare more in SimSort.h, modify
    SimSort.cxx and lib/SimSortCom.h " << endl;
    }
    t1->Branch("exit",    &exit,    "exit/D");
    t1->Branch("eventree",    &eventree,"eventree/D");
    t1->Branch("rawevent",    &rawevent,"rawevent/D");
    t1->Branch("runb",    &runb,    "runb/D");
    t1->Branch("phi",      phi,    "phi[nbpartree]/D");
    t1->Branch("phiran",       phiran,    "phiran[nbpartree]/D");
    t1->Branch("theta",    theta,    "theta[nbpartree]/D");
    t1->Branch("thetaran",    thetaran,    "thetaran[nbpartree]/D");
    t1->Branch("thetacm",    thetacm,    "thetacm[nbpartree]/D");
    t1->Branch("etot",     etot,     "etot[nbpartree]/D");
    t1->Branch("ecm",     ecm,     "ecm[nbpartree]/D");
    t1->Branch("ETOT",    ETOT,    "ETOT[nbcont]/D");
    t1->Branch("Ex",    &Ex,"Ex/D");
    if(reduce<4){
        t1->Branch("e",        e,    "e[nbpartree]/D");
        t1->Branch("de",      de,    "de[nbpartree]/D");
        t1->Branch("er",    er,    "er[nbpartree]/D");
    }
    if(reduce<3){
        t1->Branch("Exr",    &Exr,    "Exr/D");
        t1->Branch("Exb",    &Exb,    "Exb/D");
        t1->Branch("contig",    &contig,"contig/D");
        t1->Branch("ph1ph2",    &ph1ph2,"ph1ph2/D");
        t1->Branch("ph1ph3",    &ph1ph3,"ph1ph3/D");
```

```
    t1->Branch("info",    &info,    "info/D");
    t1->Branch("cz",      cz,    "cz[nbpartree]/D");
    t1->Branch("x",       x,    "x[nbpartree]/D");
    t1->Branch("xd",    xd,    "xd[nbpartree]/D");
    t1->Branch("yd",    yd,    "yd[nbpartree]/D");
    t1->Branch("zd",    zd,    "zd[nbpartree]/D");
    t1->Branch("p",       p,    "p[nbpartree]/D");
}
if(reduce<1){
    t1->Branch("det",     det,    "det[nbpartree]/D"  );
    t1->Branch("detc",     detc,    "detc[nbpartree]/D"  );
    t1->Branch("dedet",    dedet,    "dedet[nbpartree]/D");
    t1->Branch("deddet",    deddet,    "deddet[nbpartree]/D");
    t1->Branch("ded",    ded,    "ded[nbpartree]/D");
    t1->Branch("eH",    eH,    "eH[nbpartree]/D");
    t1->Branch("eL",    eL,    "eL[nbpartree]/D");
    t1->Branch("deH",    deH,    "deH[nbpartree]/D");
    t1->Branch("deL",    deL,    "deL[nbpartree]/D");
    t1->Branch("dec",     dec,    "dec[nbpartree]/D");
    t1->Branch("erc",     erc,    "erc[nbpartree]/D");
}
t1->Branch("dop0",    dop0,    "dop0[nbpartree]/D");
t1->Branch("dop1",    dop1,    "dop1[nbpartree]/D");
if(reduce<3){
    t1->Branch("cz1",     cz1,    "cz1[nbpartree]/D");
    t1->Branch("cz2",     cz2,    "cz2[nbpartree]/D");
    t1->Branch("cz3",     cz3,    "cz3[nbpartree]/D");
    t1->Branch("cz4",     cz4,    "cz4[nbpartree]/D");
    t1->Branch("dz1",     dz1,    "dz1[nbpartree]/D");
    t1->Branch("dz2",     dz2,    "dz2[nbpartree]/D");
    t1->Branch("dz3",     dz3,    "dz3[nbpartree]/D");
    t1->Branch("dz4",     dz4,    "dz4[nbpartree]/D");
    t1->Branch("eseg1",    eseg1,    "eseg1[nbpartree]/D");
    t1->Branch("eseg2",    eseg2,    "eseg2[nbpartree]/D");
    t1->Branch("eseg3",    eseg3,    "eseg3[nbpartree]/D");
    t1->Branch("eseg4",    eseg4,    "eseg4[nbpartree]/D");
}
t1->Branch("tmstmp",    tmstmp,    "tmstmp[nbpartree]/L");
if(dump==1){
    t1->Branch("ADCid",    ADCid,    "ADCid[256]/D");
    t1->Branch("ADCch",    ADCch,    "ADCch[256]/D");
}

// Leaves for Simulation
if(Simur==1){
    t1->Branch("ran",    ran,    "ran[2]/D");
    t1->Branch("exitran",    exitran,"exitran[16]/D");
    t1->Branch("statran",    statran,"statran[16]/D");
    t1->Branch("exit",    &exit,    "exit/D");
    t1->Branch("state",    state,    "state[16]/D");
    t1->Branch("effbkp",    &effbkp,"effbkp/D");
    t1->Branch("thetabkp",    &thetabkp,"thetabkp/D");
    t1->Branch("effrec",    &effrec,"effrec/D");
    t1->Branch("thetarec",    &thetarec,"thetarec/D");
    t1->Branch("depth",    &depth,"depth/D");
```

```
        t1->Branch("CASC",    &CASC,    "CASC/D");}

    Init();
    startTime = time(NULL);
    eof=1;
    blocks=0;
    nbofevent=0;
    check=stepblock;
    check2=0;
    for(i=0;i<32;i++) probs[i]=0;

    Time[12]=9999999;
    Time[14]=time(NULL) - startTime;
    cout << endl;

    for(i=0; i<512;i++) history[i]=0;
    while(skipblock){
        ReadData(dataf);    // (1 block)
        skipblock--;
        if(! skipblock) {
            cout << blocks << " blocks skipped " << endl;}}
    while (eof != 0 && blocks<nbblock) {
        if(Datar==1)    ReadData(dataf);    // (1 block)
        if(Simur==1)    SimuData();        // Simulate an event in center of
    mass
        if(fRead != 0){
            while (words){
            filter=0;
            if(Datar==1)    UnpackData();    // (1 event of the block read
    before)
            if(fUnpack != 0){
                if(foldq[0] >= trigquad && fold[0] >= trigsi && foldc[0] >= 0 &&
     fold[1] == trign && fold[2] >= trigg){
                filter=0;

/*************Look for charged particles ********************/
                ii=0;
                itemp2=0;
                nbi = 0;
    // CHARGED PARTICLES
                if(trigsi>0){
                    groupe=0;
                    for(i=1;i<=fold[groupe];i++){
                    if(filter==0.) {
                        ii++;
                        QDSDStrip(i,ii);
                        itemp = EDE(ii,99,0);          // look for SiSI gates
                        if(itemp==0) itemp = 100*EDE(ii,0,99);// look in the
    SICsI gates
                        if(itemp>0){
                        itemp=CalCorr(itemp,ii);
                        reorder[i]=itemp;}
                            // condition to find particles that are not gated
                            if(itemp==0 && node ==0) filter++;   //if particles
    are not in the gate it kills the event
```

```
                        if(fold[groupe]==1 && node >0) {
                        }
                        if(fQstrip==0) filter++;}}
                        nbi=fold[groupe];}

    // NEUTRONS
                if(trign>0){
                    groupe=1;
                    for(i=1;i<=fold[groupe];i++){
                        if(filter==0.) {
                            ii++;
                            filter=Neutron(i,ii);
                            reorder[i+nbi]=ii; }}
                        nbi=nbi+fold[groupe];}

     // GAMMAS
                if(trigg>0){
                    groupe=2;
                    for(i=1;i<=fold[groupe];i++){
                        ii++;
                        if(filter==0.) {
                            filter=Gamma(i,ii);
                            reorder[i+nbi]=ii;}}

                    if(filter==0.) { //if filter 1
                        for(i=1;i<=fold[0];i++){
                        if(reorder[i] != i && reorder[i] != 0){
                            SwapOrder(reorder[i],i);}}
                        for(i=1;i<=fold[0];i++){
                            if(reorder[i] != patern[i]) filter++;
                            if(patern[i]==0 && minimom < 1){
                                p[i]=sqrt(2.*mass[ALCP[i]][ZLCP[i]]*etot[i])
   ;
                                p4[1][i]=p[i]*sin(theta[i])*cos(phi[i]);
                                p4[2][i]=p[i]*sin(theta[i])*sin(phi[i]);
                                p4[3][i]=p[i]*cos(theta[i]);
                                v4[1][i]=p4[1][i]/mass[ALCP[i]][ZLCP[i]];
                                v4[2][i]=p4[2][i]/mass[ALCP[i]][ZLCP[i]];
                                v4[3][i]=p4[3][i]/mass[ALCP[i]][ZLCP[i]];}}

/******* Randomize the particle order ******************************/
               for(k=1;k<fold[1];k++){
                for(i=1;i<fold[1];i++){
                if(det[i] > det[i+1] ) SwapOrder(i,i+1);}}

//-----------------------------------
//In this section, events are read and selected according to the beam sequence
    within which they were emitted. Values of "modulo" are set in the .sims file

    if(modulo>0){
        if(tmstmp[1] > startmodulo && tmstmp[1] < moduloinc + startmodulo) {
    timeres=startmodulo + moduloinc-modulo;}
        if(tmstmp[1]>=moduloinc + startmodulo) moduloinc=moduloinc+modulo;
        tmstmp[0]=tmstmp[1]-timeres;
        if(tmstmp[1]<startmodulo) filter++;
```

```
        if(tmstmp[0]>135163000) filter++;  // "<"=beam off, ">"=beam on}
//-------------------------------------

    if(filter==0) { //if filter 3
       contig=0;
       if(Simur == 1){
       for(i=0;i<=nbstep[iexit];i++) {
           statran[i] = rand()/((double)RAND_MAX +1);
           state[i]=(Double_t) istate[i];}
       exitran[iexit] = rand()/((double)RAND_MAX +1);
       exit=iexit;
       ran[1]=rand()/((double)RAND_MAX +1);
       ran[2]=rand()/((double)RAND_MAX +1);
       exitnb++;
       trigger++;
       blocks++;
       ADC_events++;
       thetarec=(Double_t ) itheta[0];
       thetarec=(thetarec+rand()/((double)RAND_MAX +1))/100.;
       thetabkp=(Double_t ) itheta[1];
       thetabkp=(thetabkp+rand()/((double)RAND_MAX +1))/100.;
       effrec=1./efficiency[0][itheta[0]];
       effbkp=1./efficiency[1][itheta[1]];
       for(i=0;i<2;i++) efficiency[i][itheta[i]]=0;
           if(escape==0) gefficiency[1]++; // gamma efficiency
             }
            if(nwords[0]<1000) history[600+nwords[0]]++;
            history[39]=history[39]+1;
            eventree=(Double_t) history[39];
            if(dump==1){
               if(nwords[0]>512) nwords[0]=512;
               for(i=1; i<nwords[0]/2;i++){
                   ADCid[i] = adcdet[0][2*i] ;
                   ADCch[i] = adcdet[0][2*i+1] ;}}
                if(matrix>0){
                    if(fold[2]==2){
                    i=(Int_t)  etot[SYMETRIZE[1]];
                    ii=(Int_t) etot[SYMETRIZE[2]];
                    if(i> 0 && i<ggsize && ii> 0 && ii<ggsize) {
                        ggmat[i][ii]++;
                        ggmat[ii][i]++;}
                            ngg=ngg+2;}}
                    if(trees>0) {
                       runb=RUNB+rand()/((double)RAND_MAX +1);
                       t1->Fill();
                       if(symetrize>0){
                          SwapOrder(SYMETRIZE[1],SYMETRIZE[2]);
                          t1->Fill();}}
                          //    Fill the spectra
                          if(projections>0)
                            {i=(Int_t) dedet[1];
                            if(i>0 && i< 256){
                            ii=(Int_t) eH[1];
                            MDirect[i][ii]++;
                            MDirect[0][ii]++;}
```

```
                        i=(Int_t) det[1];
                    if(i>0 && i< 256){
                        ii=(Int_t) etot[1];
                        MDirect[i][ii]++;
                        MDirect[0][ii]++;}}}}}}}}
        events++;}
    // put the beam axis and target in the data
    if(axis){
        nbpoints[0]=100;
        nbpoints[1]=nbpoints[0];
        for(i=0;i<=nbpoints[0];i++){
            Axis();
            t1->Fill();}}

    if(Simur==1){
        char specname[128];
        if(Exit>0) {
            TH1D *Penetrability1[8];ii=1;
            for(j=1;j<=nbstep[ii];j++){sprintf(specname,"Exit%d_Step%d",ii,j
);Penetrability1[j]=new TH1D(specname,"Penetrability1",2048,0,2048);
                for(i=0;i<2048;i++) {k=(Int_t) (1000.*pf[ii][j][i]);for(l=0;
l<=k;l++) Penetrability1[j]->Fill(i);}}}
        if(Exit>1) {
            TH1D *Penetrability2[8];ii=2;
            for(j=1;j<=nbstep[ii];j++){sprintf(specname,"Exit%d_Step%d",ii,j
);Penetrability2[j]=new TH1D(specname,"Penetrability2",2048,0,2048);
                for(i=0;i<2048;i++) {k=(Int_t) (1000.*pf[ii][j][i]);for(l=0;
l<=k;l++) Penetrability2[j]->Fill(i);}}}
        if(Exit>2) {
            TH1D *Penetrability3[8];ii=3;
            for(j=1;j<=nbstep[ii];j++){sprintf(specname,"Exit%d_Step%d",ii,j
);Penetrability3[j]=new TH1D(specname,"Penetrability3",2048,0,2048);
                for(i=0;i<2048;i++) {k=(Int_t) (1000.*pf[ii][j][i]);for(l=0;
l<=k;l++) Penetrability3[j]->Fill(i);}}}
        if(Exit>3) {
            TH1D *Penetrability4[8];ii=4;
            for(j=1;j<=nbstep[ii];j++){sprintf(specname,"Exit%d_Step%d",ii,j
);Penetrability4[j]=new TH1D(specname,"Penetrability4",2048,0,2048);
                for(i=0;i<2048;i++) {k=(Int_t) (1000.*pf[ii][j][i]);for(l=0;
l<=k;l++) Penetrability4[j]->Fill(i);}}}}

    for(k=0;k<=groupmax;k++){
        if(projections>0){
            Int_t maxADC=0;
            for(i=0;i<999;i++) if(fLookupTable[k][i][0]>0 && fLookupTable[k
][i][0]<999) maxADC=i;
            char specname[128];
            TH1D *Direct[maxADC+1];
            for(j=1;j<=maxADC;j++){
                if(fLookupTable[k][j][0]>0){
                    sprintf(specname,"Channel_%d",j);
                    Direct[j]=new TH1D(specname,specname,8192,0,8192);
                    for(ii=0;ii<8192;ii++) for(i=0;i<MDirect[j][ii];i++)
Direct[j]->Fill(ii);}}
            sprintf(specname,"Channel_All");
```

```
            Direct[0]=new TH1D(specname,specname,8192,0,8192);
            for(ii=0;ii<8192;ii++) for(i=0;i<MDirect[0][ii];i++) Direct[0]->
Fill(ii);}}
    Statistics();

    endTime = time(NULL);
    f1=t1->GetCurrentFile();
    f1->Write();
    f1->Close();
    cout << "DataTreeW: finished the job in "<< endTime - startTime << " s."
 << endl;
    cout << "DataTreeW: Created root data file \""<< rootif.Data() << "\""
<< endl;
    if(writesimu>0){
        cout << "Created raw  data file \""<< dataof.Data() << "\"" << endl
;}
    dataws[runnb].close();

    // Write informations in infotree.txt
    statfs << "Information on the last tree built" << endl;
    statfs << endl;
    statfs << "Unknown ADC's (or ADC's calibrated with coefficient 0)" <<
endl;
    for(groupe=0;groupe<=groupmax;groupe++){
        statfs << "Group " << groupe << endl;
        for(i=0;i<fNchan;i++){
            if(unknownAdc[groupe][i] != 0) statfs << i << " " << unknownAdc[
groupe][i] << endl;}}
    if(fcasc>0){
        ii=1;
        Int_t remid[16384];
        for(i=0;i<16382;i++) remid[i]=i;
        while(ii){
            ii=0;
            for(i=0;i<16382;i++){
                if(caschist[i]<caschist[i+1]){
                    itemp=caschist[i+1];        itemp2=remid[i+1];
                    caschist[i+1]=caschist[i];    remid[i+1]=remid[i];
                    caschist[i]=itemp;        remid[i]=itemp2;
                    ii++;
                }}}
        statfs << "Cascade from event file" << endl;
        itemp=0;
        for(i=0;i<16383;i++) {
            itemp=itemp+caschist[i];
            if(caschist[i] != 0)  statfs << RH[remid[i]] <<  " " << caschist
[i] << "(" << endl;
        }
        statfs << caschist[16383] << " events with more than 8 particles "
<< endl;
        statfs << "Total " << itemp << " events " << endl;}
    statfs.close();
    if (Simur ==1){
        sprintf(cmd,".! cat simsort.info infotree.txt > %s.siminfo.txt",
rootf);
```

```
        gROOT->ProcessLine(cmd); }
    return;}

// The following is to write directly the raw data in a tree
void SimSort::CaliTreeW(Char_t *dataf, Char_t *rootf, Int_t cxxblock) {
    Int_t i,ii,events;
    ADC_events=0;
    postpone=0;
    words3=0;
    for(i=0;i<16;i++) empful[i]=0;
    TString rootif = rootf;
    statfs.open("infotree.txt",ios::out);
    runnb++;
    TFile *f1=new TFile(rootif.Data(),"RECREATE");
    TTree *t1=new TTree("DataTree","Uncalibrated Data");

    if(fInput    == 0) Input("default/sims/Simu.6Li7Li.sims");
    if(fGain     == 0) SetGain("default/cal/gain.cal");
    if(fOffset   == 0) SetOffset("default/cal/offset.cal");
    if(fPosition == 0) SetPosition("default/cal/position.cal");
    if(fLookup   == 0) SetLookup("default/cal/lookup.cal");
    if(fThickq   == 0) SetThick("default/cal/thickness.cal");
    nbpartree=4;
    if(dump!=1){
        t1->Branch("nbpartree", &nbpartree,"nbpartree/I");
        t1->Branch("det",    det,    "det[nbpartree]/D");
        t1->Branch("detc",    detc,    "detc[nbpartree]/D");
        t1->Branch("dedet",    dedet,    "dedet[nbpartree]/D");
        t1->Branch("deddet",    deddet,    "deddet[nbpartree]/D");
        t1->Branch("cz",    cz,    "cz[nbpartree]/D");
        t1->Branch("de",    de,    "de[nbpartree]/D");
        t1->Branch("ded",    ded,    "ded[nbpartree]/D");
        t1->Branch("er",    er,    "er[nbpartree]/D");
        t1->Branch("eH",    eH,    "eH[nbpartree]/D");
        t1->Branch("eL",    eL,    "eL[nbpartree]/D");
    }
    if(dump==1){
        t1->Branch("ADCid",    ADCid,    "ADCid[256]/D");
        t1->Branch("ADCch",    ADCch,    "ADCch[256]/D");
    }
    Init();
    startTime = time(NULL);
    eof=1;
    blocks=0;
    check=stepblock;
    cout << endl;
    for(i=0;i<512;i++) history[i]=0;

    if(cxxblock>0) {
        nbblock=cxxblock;
        if(nbblock>10000) stepblock=10000;
        else stepblock=nbblock/2;
        cout << "  nbblock reinitialised: " << nbblock << endl;
    }
    while(skipblock){
```

```
            ReadData(dataf);    // (1 block)
            skipblock--;
            if(! skipblock) {
                cout << blocks << " blocks skipped   " << endl;}}
        while (eof != 0 && blocks<nbblock) {
            ReadData(dataf);
            if(fRead != 0){
                while (words){
                    UnpackData();
                    if(fUnpack != 0){
                        groupe=0;
                        if(fold[groupe] > 0 && fold[groupe] <5){

                            ii=0;
                            for(i=1;i<=fold[groupe];i++){
                                ii++;
                                QDSDStrip(i,ii);}

                            history[39]=history[39]+1;
                            eventree=(Double_t) history[39];}
                        if(dump==1){
                            if(nwords[groupe]>512) nwords[groupe]=512;
                            for(i=0; i<nwords[groupe]/2;i++){
                                ADCid[i] = adcdet[groupe][2*i] ;
                                ADCch[i] = adcdet[groupe][2*i+1] ;}}
                        t1->Fill();}}}
            events++;}
        endTime = time(NULL);
        f1=t1->GetCurrentFile();
        f1->Write();
        f1->Close();
        cout << "DataTreeW: finished the job in "
        << endTime - startTime << " s." << endl;
        cout << "DataTreeW: Created root data file \""
        << rootif.Data() << "\"." << endl;
        cout << "ADC Events =  \""
        << ADC_events << "\"." << endl;

        // Write informations in infotree.txt
        statfs << "Information on the last tree built" << endl;
        statfs << endl;
        statfs << "Unknown ADC's (or ADC's calibrated with coefficient 0)" <<
    endl;
        for(groupe=0;groupe<=groupmax;groupe++){
            statfs << "Group " << groupe << endl;
            for(i=0;i<fNchan;i++){
                if(unknownAdc[groupe][i] != 0) statfs << i << " " << unknownAdc[
    groupe][i] << endl;}}
        statfs.close();
        return;
    }
```

B.4 *.cal* files

- **detector.cal**

```
Type    L(mm)   W(mm)   Orientation(deg)        ADC
GE      50.0    50.0    0.0                     64 80
GE      50.0    50.0    0.0                     96 112
GE      50.0    50.0    0.0                     128 150
```

- **lookup.cal**

```
HADC    LADC    ADD-1   ADD-2   BGO-1   BGO-2   TH-GE   D-GE    PH-GE   DS
    -PSD  TH-PSD  D-PSD   PH-DSD  DSx-PSD DSy-PSD
064.080 999     064     064     999     999     135.    150.0   90.
    0.0
067.083 999     067     067     999     999     135.    150.0   90.
    0.0
068.084 999     068     068     999     999     135.    150.0   90.
    0.0
072.088 999     072     072     999     999     135.    150.0   90.
    0.0
076.092 999     076     076     999     999     135.    150.0   90.
    0.0
096.112 999     096     096     999     999     135.    150.0   90.
    0.0
099.115 999     099     099     999     999     135.    150.0   90.
    0.0
100.116 999     100     100     999     999     135.    150.0   90.
    0.0
104.120 999     104     104     999     999     135.    150.0   90.
    0.0
128.144 999     128     128     999     999     135.    150.0   90.
    0.0
132.148 999     132     132     999     999     135.    150.0   90.
    0.0
```

- **gain.cal**

```
1.
1.
0.812222
1.
1.
1.
0.6554
1.
1.
1.
0.796541
1.
1.
1.
0.695727
```

```
1.
1.
1.
1.
1.
0.661129
0.828983
1.
1.
1.
0.688911
1.
1.
1.
```

- **offset.cal**

```
0.              0.              128000.
0.              0.              128000.
0.33349                 0.              128000.
0.              0.              128000.
0.              0.              128000.
0.              0.              128000.
-2.36641                0.              128000.
0.              0.              128000.
0.              0.              128000.
0.              0.              128000.
2.19792                 0.              128000.
0.              0.              128000.
0.              0.              128000.
0.              0.              128000.
0.901054                0.              128000.
0.              0.              128000.
0.              0.              128000.
0.              0.              128000.
0.              0.              128000.
0.              0.              128000.
2.50329                 0.              128000.
1.73064                 0.              128000.
0.              0.              128000.
0.              0.              128000.
0.              0.              128000.
-0.134458               0.              128000.
0.              0.              128000.
0.              0.              128000.
0.              0.              128000.
```

Appendix C

Projections of ΔE-E plots

Projections of ΔE-E plots on the abscissa before applying energy loss correction and setting time gates are represented in Figures C.1, C.2 and C.3.

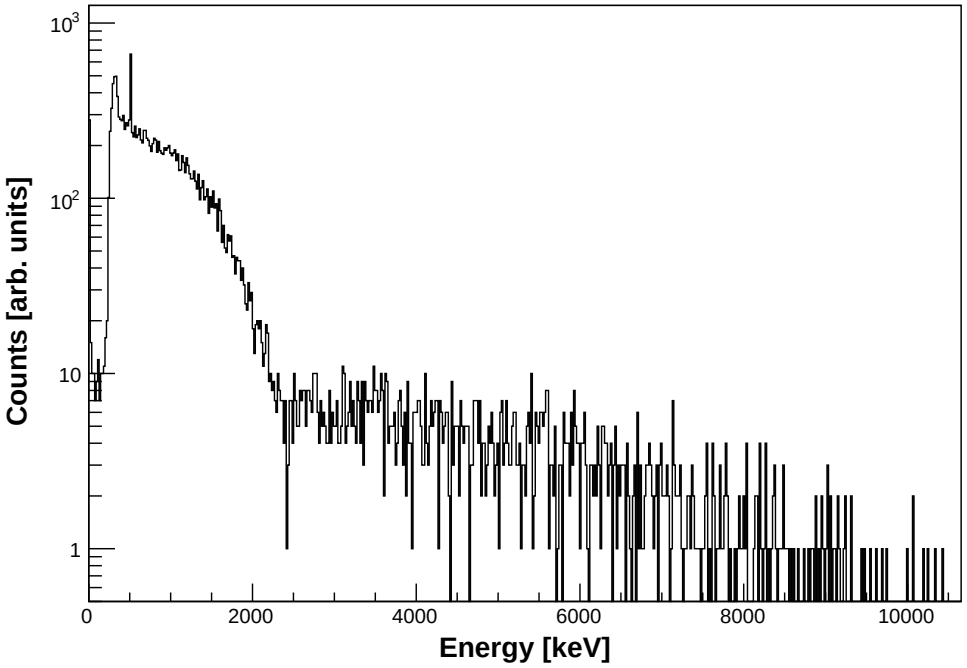

Figure C.1: p+^{nat}Li reaction

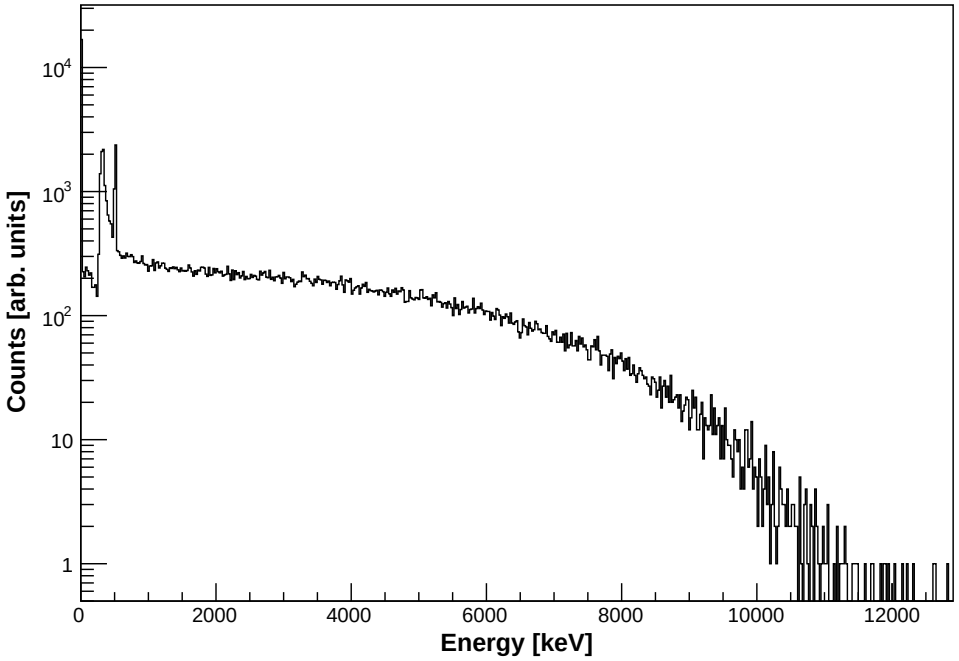

Figure C.2: p+^{9}Be reaction

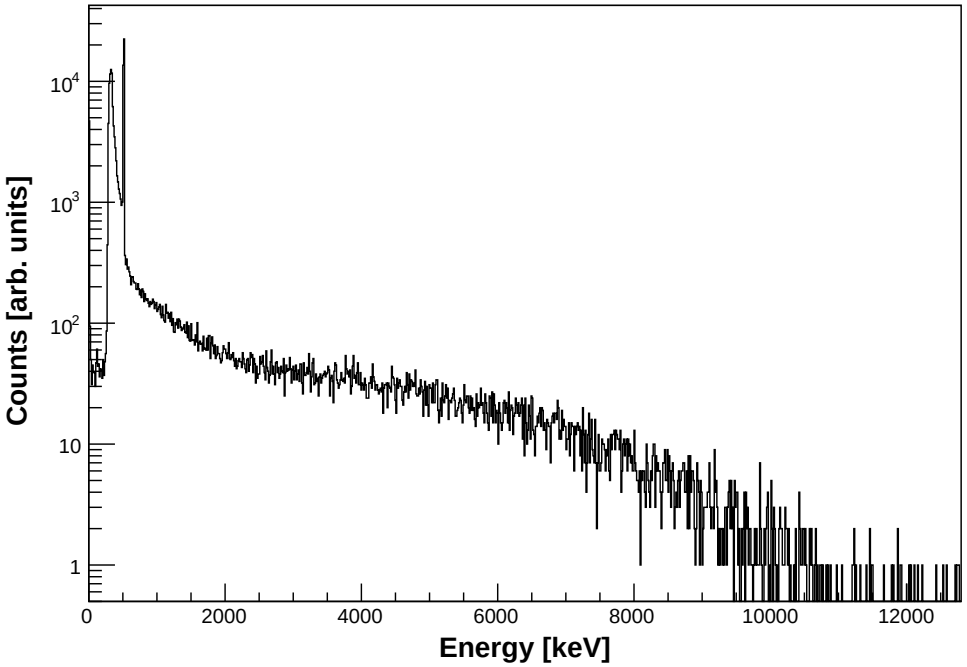

Figure C.3: p+^{nat}B reaction

Bibliography

[1] I. Tanihata, *et al.*, Phys. Rev. Lett. **55**, 2676 (1985).

[2] Y. Suzuki, *et al.*, *Structure and Reactions of Light Exotic Nuclei* (Taylor & Francis Group, London and New York, 2003).

[3] F. Uchiyama (2003), `nucl-th/0309080`.

[4] D. J. Morrissey and B. M. Sherrill, Lect. Notes Phys. **651**, 113–135 (2004).

[5] M. Lindroos, in *9th European Particle Accelerator Conference (EPAC 2004) Lucerne, Switzerland, July 5-9, 2004* (2004), URL `http://weblib.cern.ch/abstract?CERN-AB-2004-086`.

[6] B. R. Fulton, Journal of Physics: Conference Series **312**, 052001 (2011), URL `https://doi.org/10.1088%2F1742-6596%2F312%2F5%2F052001`.

[7] A. Gottberg, Nuclear Instruments and Methods in Physics Research Section B: Beam Interactions with Materials and Atoms **376**, 8 (2016), proceedings of the XVIIth International Conference on Electromagnetic Isotope Separators and Related Topics (EMIS2015), Grand Rapids, MI, U.S.A., 11-15 May 2015.

[8] T. Nilsson, in *Exotic Nuclei and Atomic Masses*, edited by J. Äystö, *et al.* (Springer Berlin Heidelberg, Berlin, Heidelberg, 2003), pp. 469–472.

[9] O. Kofoed-Hansen, in *Proceedings: International conference on nuclei far from stability 3* (1976), pp. 65–70.

[10] R. Bark, *et al.*, in *American Institute of Physics Conference Series* (2018), vol. 1962 of *American Institute of Physics Conference Series*, p. 030021.

[11] J. L. Conradie, *et al.*, in *Proc. 13th International Topical Meeting on Nuclear Applications of Accelerators (AccApp '17), Québec City, Québec, Canada July 31-August 4, 2017* (2017), pp. 127–136.

[12] J. Conradie *et al.*, in *Proc. 9th International Particle Accelerator Conference (IPAC'18), Vancouver, BC, Canada, April 29-May 4, 2018* (JACoW Publishing, Geneva, Switzerland, 2018), no. 9 in International Particle Accelerator Conference, pp. 1240–1243.

[13] A. Knecht, *et al.*, Phys. Rev. C **86**, 035506 (2012).

[14] R. Raabe, *et al.*, Phys. Rev. C **80**, 054307 (2009).

[15] A. Nesterov, *et al.*, Physics of Atomic Nuclei **64**, 1409 (2001).

[16] S. Mianowski, *et al.*, Acta Phys. Pol. B **41**, 449 (2010).

[17] *β^--Decay Evaluated Data, ^{9}Li* (2014), URL `https://tunl.duke.edu/sites/tunl.duke.edu/files/nucldata/GroundStatedecays/09Li.html`.

[18] A. J. Koning, *et al.*, *Talys-1.0* (2008).

[19] S. Hilaire, *TALYS : A tool to go from theoretical modeling of nuclear reactions to evaluations* (2015).

[20] W. R. Leo, *Techniques for nuclear and particle physics experiments* (Springer, 1992).

[21] H. Bethe and W. Heitler, Proceedings of the Royal Society of London. Series A, Containing Papers of a Mathematical and Physical Character **146**, 83 (1934).

[22] G. F. Knoll, *Radiation Detection and Measurement* (John Wiley & Sons, 2000), 3rd ed.

[23] K. S. Krane, *Introductory Nuclear Physics* (John Wiley, 1988).

[24] J. Orear and E. Fermi, *Nuclear Physics: A Course Given by Enrico Fermi at the University of Chicago*, The university of Chicago committee on publications in the physical sciences (University of Chicago Press, 1950).

[25] J. Kantele, *Handbook of nuclear spectrometry* (Academic Press, London, 1995).

[26] O. B. Tarasov and D. Bazin, Nuclear Instruments and Methods in Physics Research Section B: Beam Interactions with Materials and Atoms **266**, 4657 (2008), proceedings of the XVth International Conference on Electromagnetic Isotope Separators and Techniques Related to their Applications.

[27] G. Gamow and E. Teller, Phys. Rev. **49**, 895 (1936).

[28] S. H. Byun, in *Radioisotopes and Radiation Methodology* (Lecture Notes, McMaster University, Hamilton, Ontario, Canada, 2017).

[29] K. Wille and J. McFall, *The Physics of Particle Accelerators: An Introduction*, The Physics of Particle Accelerators: An Introduction (Oxford University Press, 2000).

[30] M. Rahman, International Journal of Instrumentation Science **1**, 63 (2013).

[31] R. Scrivens (2006), URL `https://cds.cern.ch/record/941321`.

[32] D. Faircloth, in *CERN Accelerator School on High Power Hadron Machines* (2013), `1302.3745`.

[33] G. Steyn, *et al.*, Instruments **2**, 29 (2018).

[34] F. Nemulodi, Ph.D. thesis, Stellenbosch University (2015).

[35] R. T. Newman, Balkan Phys. Lett., Special Issue, pp. 182–190 (1998).

[36] D. E. Groom, *et al.*, Atomic Data and Nuclear Data Tables **78**, 183 (2001).

[37] P. Jones, *et al.*, in *iThemba LABS Annual Report March 2013*, edited by K. Lawrie (2013), pp. 79–80, URL `https://tlabs.ac.za/wp-content/uploads/pdf/annual_reports/Annual_Report_2013_small.pdf`.

[38] XIALLC, *Pixie-16 User Manual*, XIA LLC (December 11, 2018).

[39] V. Pucknell and D. Laff, *Multi instance data acquisition system (midas)*, URL `http://npg.dl.ac.uk/MIDAS/`.

[40] XIALLC, *Pixie-4 Express User Manual*, XIA LLC (February 15, 2018).

[41] I. Pro, *Wavemetrics, inc.* (2019), URL `https://www.wavemetrics.com/`.

[42] P. Papka, *SimSort simulation and analysis code*, Unpublished Manuscript.

[43] I. Antcheva, *et al.*, Computer Physics Communications **180**, 2499 (2009).

[44] F. Crespi, *et al.*, Nuclear Instruments and Methods in Physics Research Section A: Accelerators, Spectrometers, Detectors and Associated Equipment **705**, 47 (2013).

[45] M. J. Berger, *et al.*, *ESTAR, PSTAR, and ASTAR: Computer programs for calculating stopping-power and range tables for electrons, protons, and helium ions* (2019), URL `http://physics.nist.gov/Star.publisher=NationalInstituteofStandardsandTechnology,Gaithersburg,MD`.

[46] J. J. van Zyl, Ph.D. thesis, Stellenbosch University (2012).